Tensor Network Simulation Methods for Open Quantum Lattice Models

Conor Paul Mc Keever

Department of Physics and Astronomy

University College London

This thesis is submitted for the degree of

Doctor of Philosophy

2021

I dedicate this thesis to my loving parents.

Declaration

I, Conor Paul Mc Keever confirm that the work presented in this thesis is my own. Where information has been derived from other sources, I confirm that this has been indicated in the thesis.

Conor Paul Mc Keever

2021

Publications

Parts of this thesis have been published:

C. Mc Keever and M. H. Szymańska. *Stable iPEPO Tensor-Network Algorithm for Dynamics of Two-Dimensional Open Quantum Lattice Models.* Phys. Rev. X, **11**: 021035 - Published 14 May 2021.

Acknowledgements

This work was supported by the Centre for Doctoral Training in Delivering Quantum Technologies at University College London. Engineering and Physical Sciences Research Council (Grant no. EP/L015242/1).

Abstract

A complex quantum system cannot be perfectly isolated from its surroundings and is typically subject to incoherent processes. Dissipation and/or an external drive can move the system away from thermal equilibrium to a non-equilibrium regime. Often, dissipation is an unwanted feature which is minimised as much as possible, while in others cases, it can be harnessed to stabilise interesting phases of matter. The subject of this thesis is the development of tensor network techniques to probe the dynamics and steady state properties of many-body open quantum systems.

Our theoretical understanding of many-body open quantum systems is greatly aided by numerical techniques. However, numerical methods are remarkably limited by the exponential growth of many-body Hilbert spaces. Tensor network methods are a class of numerical techniques which aim to circumvent the exponential growth of Hilbert space by representing the quantum state as a network of tensors. Doing so allows for an efficient representation and manipulation of the quantum state.

In the first part of this thesis, a tensor network method is presented in a Cluster Mean Field framework. This method integrates a one-dimensional Lindblad master equation by dividing the system into finite sized clusters, each represented by a tensor network. The effective master equation is integrated in real time using a sweeping Time Evolving Block Decimation

algorithm and the method is used to investigate the steady properties of a dissipative Jaynes-Cummings-Hubbard model with a two-photon drive where a finite size scaling of the cluster sizes allows for comparison with equilibrium models.

The simulation of two-dimensional open quantum lattice models are the subject of the second part of the thesis. The Infinite Projected Entangled Pair Operator is used as an ansatz for the density matrix of a system on an infinite square lattice. The key development is a method to optimise the truncation of enlarged tensor bonds in a way which is appropriate for mixed states. The method is tested against exactly solvable cases and literature results. In the final chapter, the algorithm is applied to a dissipative anisotropic XY-model and revealing the nature of a transition parameterised by the strength of dissipation.

Impact Statement

The principal development of this work is an accurate numerical method for simulating open quantum lattice models in spatial dimensions greater than one. The method, which is based on tensor network techniques, will open new research directions which were previously inaccessible in the study of open quantum systems. For instance, the method will allow for the numerical study of large two-dimensional arrays of atoms which interact with their environment, a class of system which has applications in quantum simulation and the modelling of materials.

Tensor networks are a highly compact way of representing a quantum state and are commonly used in the simulation of one-dimensional systems; for example, a chain of interacting atoms. They are most commonly applied to systems which are completely isolated from their environments, an idealised scenario which is difficult to achieve is a real device. The work of this thesis demonstrates that tensor networks can be used to accurately simulate open quantum lattice models in two dimensions and will give access to new out-of-equilibrium phenomena which are expected to emerge in systems of spatial dimension greater than one.

Efficient and reliable classical numerical simulation tools related to those developed in this work will push the boundaries of the classical simulation of complex open quantum systems and become a useful tool in benchmarking and verification of quantum simulation devices. It is expected further high impact research which builds upon the work presented here will emerge in the near future and that as the methods mature, they will

be routinely used and become an integral part of the theoretical study of open quantum lattice models.

Contents

Nomenclature

Roman Symbols

CMF Cluster Mean Field

CTM Corner Transfer Matrix

CTMRG Corner Transfer Matrix Renormalisation Group

DMRG Density Matrix Renomalisation Group

FET Full Environment Truncation

iPEPO infinite Projected Entangled Pair Operator

iPEPS infinite Projected Entangled Pair State

LPTN Locally Purified Tensor Network

MF Mean Field

MPDO Matrix Product Density Operator

MPO Matrix Product Operator

MPS Matrix Product State

NISQ Noisy Intermediate-Scale Quantum

TEBD Time Evolving Block Decimation

TN Tensor Network

TTN Tree Tensor Network

WTG Weighted Trace Gauge

Chapter 1

Introduction

In the twentieth century, the development of quantum mechanics caused a radical shift in our understanding of the world, so much so that we are still grappling with its implications. To this day, quantum mechanics frequently gives rise to new and unexpected physical phenomena, challenging our understanding of reality. From a technological perspective, what has been achieved as a result of our understanding of quantum mechanics in the past few decades has been astounding; the *first quantum revolution* [113] has given rise to a plethora of new technologies ranging from medical imaging to precision measurement and semiconductor devices. Catalysts of the Information Age, these technologies have undergone an unprecedented pace of development, perhaps exemplified most compellingly by Moore's law [125] which projected that the number of transistors in a dense integrated circuit would double approximately every two years; a projection which device manufacturers have been able to achieve for decades.

There are, however, signals that Moore's law is coming to an end. As the size of semiconductor components reach their lower limits, it will be necessary to rethink the routes forward beyond physical miniaturisation and increasing clock speed. Furthermore, the physical limits of other conventional technologies such as measurement devices have, in many cases, already been achieved. A much anticipated and intriguing route forward

again relies on quantum mechanics. The *second quantum revolution* [113] shifts the focus towards exploiting some of the stranger aspects of the theory. Following John Bell's famous theorem [10], the field of quantum information emerged and promised remarkable advances in information science, indeed the burgeoning field of quantum technologies is moving forward at pace, with the development of technologies such as quantum enhanced measurement, quantum clocks, quantum simulators and quantum communication. Moreover, advances towards a many-body quantum simulation devices and universal quantum computing have gained considerable pace within a short few years. In particular, a variety of experimental platforms have been developed which offer exquisite coherent control of quantum systems, these include: cold atoms [19, 71, 146, 153]; trapped ions [17, 18, 34, 124, 163]; superconducting qubits and quantum electrodynamic circuits [4, 16, 32, 179, 193] and exciton-polariton microcavities [2, 30] among others.

In dealing with these microscopic systems governed by quantum mechanics, it is typically found that interesting physical states are extremely fragile. A quantum system such as an array of coupled two-level systems will invariably interact with its environment and a process called *decoherence* [154] will cause the system to lose the quantum mechanical nature which made it useful for technological applications; for example, the measurement of a quantum system by an observer will cause a quantum system to collapse to a classical state and the coupling of a quantum system to a noisy environment tends to introduce decoherence via incoherent processes. Typical quantum systems in the lab cannot be perfectly isolated from their surroundings and the problem of decoherence is one of the central barriers to building large scale and useful quantum information processing devices [145].

Different physical platforms experience their own characteristic source of decoherence. Low temperature superconducting qubit architectures (for example [4]) ere rep-

resentative of the state-of-the-art of quantum computing and the current generation of devices falls into the category of Noisy Intermediate-Scale Quantum (NISQ) [145]. These devices undergo decoherence from a variety of sources including: thermal noise from the environment, noise due to qubit imperfections, residual stray fields between qubits and even correlated errors from background radiation, among others [4, 115, 160, 189]. Trapped ion systems can experience decoherence from non-uniform and stray electromagnetic fields [124] and optical devices such as exciton-polariton microcavities undergo an incoherent loss of photons to their environments [30]. In the context of quantum information processing, the coupling of a quantum system to sources of noise is typically regarded as a nuisance which is to be minimised as far as possible.

However, the coupling of a quantum system to its environment is not always something to be avoided, indeed there are many ways in which the system-environment coupling can be utilised for practical purposes and provide opportunities to study fundamental physics in a new non-equilibrium paradigm. Recent years have seen a surge in interest in these areas, driven in part by the prospect of using controlled dissipative channels to engineer interesting many-body quantum states with possible applications in quantum state preparation, quantum memory devices and even dissipative quantum computing [1, 50, 127, 142, 172, 185].

From the perspective of fundamental physics, the prospect of new physics beyond equilibrium has driven a large body of research, a prime example of this is non-equilibrium criticality. Criticality in classical systems is driven by a competition between energy and entropy from thermal fluctuations. For a quantum system at zero temperature, critical phenomena can still occur due to a competition between terms in the Hamiltonian which do not commute. Away from equilibrium, driven dissipative quantum systems open the possibility for even richer physics: by a careful engineering of driving and dissipation, is it possible to stabilise phases which have no counterpart at equilib-

rium [88, 108]. For example, the non-equilibrium setting opens the possibility of having long range order in two-dimensional systems (see for example the case of flocking [166]) which, in the equilibrium setting, would violate the Mermin-Wagner theorem [120].

Many examples of non-equilibrium criticality have emergent equilibrium physics where the dissipation can lead to the emergence of an effective temperature and the critical behaviour is captured by an equilibrium universality class; see for example [46, 63, 122]. Other systems define new dynamical universality classes which lie beyond the standard classification of equilibrium and are examples of non-equilibrium quantum criticality; see for example [116, 161]. While important steps have been taken towards providing a general framework in which they can be studied; for example, the development of a spectral theory of Liouvillians [121], our understanding of these phenomena is still in its infancy and there is undoubtedly a lot of physics remaining to be explored in a field which can no longer draw upon the well developed tools of equilibrium thermodynamics.

Another area of research which has recently attracted a lot interest is *time crystallinity*. In analogy to more conventional phase solid state phases associated to spatial symmetry breaking, in time crystals, a spontaneous breaking of time-translational invariance occurs. The possibility of this happening at equilibrium has been ruled out [181], however, non equilibrium many-body systems offer a platform on which time crystalline behaviour can be observed. So called *discrete time crystals* occur in systems subject to a periodic driving and are associated to discrete time translational symmetry breaking characterised by observables which have oscillations at multiples of the driving period [55, 149]. On the other hand, *dissipative time crystals* and *boundary time crystals* have been also been investigated whereby the emergent time periodicity is associated with the breaking of time translational symmetry as a result of coupling to an environment; see for example [20, 25, 84, 93, 106, 167, 196].

Given the richness of the physics in this out-of-equilibrium many-body setting, how do we study such systems theoretically? The field of *open quantum systems* [23, 28] aims to develop a framework in which out-of-equilibrium systems can be modelled and understood. Although the inclusion of the environment typically impedes a simple solution, there are a variety of analytical and numerical tools available for investigating few-body open quantum systems. Small systems can usually be treated by so called *exact numerical methods* where all degrees of freedom in the model are accounted for in the numerics. When larger systems are considered, however, one quickly encounters a central problem: the number of parameters required to represent the state of the many-body system—the size of its Hilbert space—grows exponentially with the size of the system. This phenomenon, an example of the so called *curse of dimensionality* [11], led Richard Feynman to propose quantum simulation as a means of simulating many-body quantum systems in the early 1980s [59]. Even after decades Moore's law holding fast, exact numerical methods for simulating many-body quantum systems are extremely limited in the system sizes which can be dealt with. This barrier to exact simulation has prompted a different approach in which *approximate numerical methods* have been developed to try to overcome the curse of dimensionality—see [184] for a recent review.

One such class of approximate numerical method is built upon networks of interconnected tensors. Tensor Network (TN) methods [53, 134] are based on the idea that, although the full space of states which a quantum system can explore—its Hilbert space—scales exponentially in the system size, many physically relevant states in which we might have an interest, tend to live in a very small subspace of the full Hilbert space. To make use of this, the state vector or density matrix of the system is represented as a TN and the structure of this TN ansatz restricts the set of states which a system can explore to a very small subspace of the full Hilbert space. By making use of the TN structure, the state can often be efficiently represented on a classical computer.

The long-standing success of numerical TN methods is due to the so called *entanglement area law*, whereby the entanglement entropy of a region of space scales with the size of its boundary rather than its volume [109, 141, 162, 177, 190, 191]. The area law essentially specifies the structure of quantum entanglement possessed by a large class of commonly encountered quantum many body states and, importantly, by the tensor network representation itself [53, 79, 134]. Underpinned by the strong theoretical guarantees surrounding the entanglement area law, TN method have become an indispensable tool in the numerical simulation of isolated (closed) quantum systems and the reasons why they work so well in certain situations are well understood and motivated—these will be discussed further in Chapter 2. In the context of open quantum systems the picture is much less clear and, apart from some results surrounding so called *rapidly mixing* systems [21, 92] which will be discussed in Chapter 2, we typically do not have the same strong theoretical guarantees available as we do for closed systems. For example, if one is interested in calculating time dynamics or in calculating steady states via real time evolution, then it is not clear whether the steady state or all of the transient states visited during evolution can be efficiently represented by a TN. Nevertheless, it is reasonable to expect that in many cases, if dissipative processes are sufficiently local, then the growth of entanglement will be curtailed and limit correlations generated by entangling dynamics. In the absence of theoretical guarantees, a *try it and see* approach is often taken by which some intuition can be built up.

Apart form a handful of examples [35, 40, 65, 77, 101, 118, 171, 186, 197], numerical TN methods intended for the simulation of open quantum systems are much less well developed than their closed system counterparts. This opens up many research directions wherein the powerful TN techniques developed for closed systems can be adapted and incorporated into new simulation methods for open quantum systems. The resulting algorithms will inherit efficiency and representational power of TNs and expand the toolkit

for exploring the physics of open quantum systems while also providing a new perspective of the structure of non-equilibrium quantum systems from the viewpoint of quantum entanglement. This thesis ventures along this research direction. In summary, the thesis explores the development of numerical tensor network methods for open quantum systems in one and two spatial dimensions. The central contribution of the thesis is a TN algorithm for simulating open quantum systems on a square lattice which adapts and appropriates some existing techniques intended for closed two-dimensional systems to the open system context. This reliable and efficient new algorithm offers a powerful tool to explore the physics of two-dimensional many-body non-equilibrium quantum systems, a paradigm which is relevant in both near term applications in quantum technologies and fundamental physics.

The following sections will introduce in more detail the particular research area covered in this thesis. In doing so, it will be helpful to discuss more precisely what is meant by an open quantum lattice model and to introduce the Lindblad master equation. Following this, there will be a short discussion covering the various different approaches to solving open quantum lattice models numerically. Finally, motivation for the use of tensor network techniques for this purpose will be discussed and the specific contents and contributions made by this thesis will be presented.

1.1 Open Quantum Lattice Models

In the study of condensed matter, it is natural to encounter collective systems of atoms forming crystals with highly ordered structure in space. It is therefore common to model such a system using a lattice structure, where the constituent parts of the system are located on the lattice points and interact with those on neighbouring lattice points. In this context it is common to think of the lattice as a graph $G = (V, E)$ composed of vertices V and edges E. A lattice can be constructed from any arbitrary graph,

however, regular graphs such as square, triangular and hexagonal lattices are by far the most commonly studied since they are commonly found in natural condensed matter systems. In this thesis, all of the discussion is restricted to lattices on simple cubic graphs of dimension $\mathcal{D}$, $V = L^{\mathcal{D}}$, in fact we will be concerned only with cubic lattices in $\mathcal{D} = 1$ and $\mathcal{D} = 2$ dimensions. When we speak of a *quantum lattice model* we refer to a lattice where each vertex or site hosts a quantum system; for example, a quantum spin of dimension d, an harmonic oscillator or some more general fermionic or bosonic degree of freedom. For finite-dimensional spin systems; for example, a two-level system, the individual local Hilbert spaces $\mathbb{C}^d$ associated to each lattice site compose to form a Hilbert space of the full lattice system $\mathcal{H} = (\mathbb{C}^d)^{\otimes n}$ where $n = |V|$ is the system's size, equivalent to its number of vertices. The fact that the size of the Hilbert space $\mathcal{H}$ grows exponentially with the size of the system n lies at the heart of why exact numerical simulations of these systems very quickly become infeasible as n increases.

Closed Quantum Systems

In quantum mechanics [70, 150], an isolated quantum system undergoes and evolution in time which is reversible and generated by a Hermitian operator called the Hamiltonian H. In the so called Schrödinger picture, the time evolution is described by a time dependent state $|\Psi(t)\rangle$ and a time independent Hamiltonian H. In terms of these objects the Schrödinger equation takes the form of equation 1.1 where Planck's constant $\hbar$ is set to unity ($\hbar = 1$)

$$i\frac{d}{dt}|\Psi(t)\rangle = H|\Psi(t)\rangle. \tag{1.1}$$

The pure state ($|\Psi\rangle$ or $|\psi\rangle$) representation of the system is appropriate when all that can be known about the system is accounted for, however, this is not always the case. For example, if we consider a preparation scheme which prepares the an ensemble

of pure states $|\psi_j\rangle$, each with probability p_j where $\sum_j p_j = 1$, then, if we have no knowledge of the particular state prepared by the scheme then the expectation value of some observable A is an average over all possible states weighted by their respective probabilities of preparation: $\langle A\rangle = \sum_j p_j \langle\psi_j|A|\psi\rangle$. Using the cyclic property of the trace, this can be recast this in a form where the ensemble of states is described by a *density operator* or *density matrix* $\rho = \sum_j p_i |\psi_j\rangle\langle\psi_j|$ and the expectation value simply becomes $\langle A\rangle = \mathrm{tr}[\rho A]$. The density matrix representation therefore reflects our lack of full knowledge of the state. In the case where the ensemble is composed of one pure state; for example, suppose we choose that in our ensemble preparation scheme, only one of the probabilities is non-zero $p_k = 1$, then the density matrix describes what is called a *pure state* $\rho = |\psi_k\rangle\langle\psi_k|$ which is a rank-1 projection operator such that $\rho^2 = \rho$. On the other hand, where the ensemble is composed of multiple pure states, the system density matrix is referred to as *mixed* and its *purity* defined as $P = \mathrm{tr}[\rho^2]$. The evolution of such a closed system density matrix in time can be expressed in the Schrödinger picture using the so called *Liouville-von Neumann equation* (see for example [23])

$$\frac{d}{dt}\rho(t) = -i[H, \rho(t)] \tag{1.2}$$

where the square brackets denote the commutator. The Liouville-von Neumann equation will provide a useful starting point for the derivation of the Lindblad master equation which, rather than describing the evolution of a closed system density matrix, instead describes the evolution of a density matrix which represents the state of a system which is coupled to a external reservoir; these so called *open quantum systems* [23, 28] will be discussed in the next subsection.

It is useful to specify the kind of Hamiltonians considered this thesis. Even if we are considering a system which interacts with an external reservoir, we will typically describe the system's internal dynamics using a Hamiltonian. This is no different to a

Hamiltonian describing an isolated quantum system. As discussed previously, we will typically consider Hamiltonians describing regular quantum lattice models where the lattice describes the underlying geometry of the system and the Hamiltonian describes the physics. The focus in this thesis is on systems with short ranged interactions, in particular, all of the models considered have at most two-local couplings. This means that the Hamiltonian can be written in the form

$$H = \sum_j h_j^{(0)} + \sum_{\langle j,k \rangle} h_{j,k}^{(1)} \quad j,k \in V \tag{1.3}$$

where, the angular brackets $\langle j,k \rangle$ denote that the lattice sites j and k are nearest neighbours. This is a very natural description of a typical physical system—each constituent part interacts only with those other constituent parts which are nearest to it. There are very many instances of two-local Hamiltonians in the literature and they have been studied in great depth, while their basic local geometric construction is simple, they give rise to an astonishingly complex array of phenomena.

Open Quantum Systems

Hamiltonian lattice models describe systems of particles hopping on a lattice which is isolated from any other external system or reservoir. Often one encounters the situation where the lattice system is embedded within a larger physical system with which it may interact. A typical example of such a situation arises in light-matter systems [30]. For example, a polariton lattice is a driven-dissipative system; light form a laser is resonant with an optical cavity, this light remains trapped in the cavity for a short time during which it has some probability of creating a matter excitation in the form of an electron-hole pair in a semiconductor. This excitation will decay after some short time, releasing the photon back into the cavity where this excitation-de-excitation process can continue. After some time however, the photon will escape from the cavity back into the

environment. Clearly, a full description of this systems which includes both gain from the laser and loss of photons to the reservoir requires more than just the description of the internal dynamics of the lattice.

In general, an open quantum system S is coupled to another quantum system B which represents the *reservoir*—also often called the *bath* or *environment*. The system S is therefore a subsystem of the combined system $S + B$, in most cases it can be assumed that the combined system is closed. The subsystem S will therefore evolve according to both the internal system dynamics of S and as a result of its interaction with B. The full Hilbert space of the system is described by $\mathcal{H} = \mathcal{H}_S \otimes \mathcal{H}_B$ on which the Hamiltonian $H = H_S \otimes I_B + I_S \otimes H_B + H_I$ describes the Hamiltonian H_S of the system by itself, the Hamiltonian H_B of the bath and the Hamiltonian H_I describing the interaction between the two subsystems S and B. While the combined system $S + B$ evolves according to unitary dynamics, in general, the dynamics of the subsystem S are no longer unitary.

Suppose that the state of the full system $(S+B)$ is described by the density matrix ρ, then the state of the system S can be found by tracing over the reservoir leaving a state which is described by the so called *reduced density matrix* $\rho_S = \mathrm{tr}_B \rho$, where the subscript denotes the partial trace over the subsystem B. In general, the reduced density matrix can be mixed, even if the state of the combined system is pure. The reduced density matrix $\rho_S(t)$ at a time t is obtained by tracing over the combined system's density matrix $\rho(t)$, therefore the equation of motion for the reduced system $\rho_S(t)$ can be expressed as the Liouville-von Neumann equation of the combined system

$$\frac{d}{dt}\rho_S(t) = -i\mathrm{tr}[H, \rho(t)]. \tag{1.4}$$

In principle, one could try to solve equation 1.4 for the reduced density matrix $\rho_S(t)$ by accounting for the full $S + B$ system with the tools appropriate for solving closed quantum lattice models and indeed this is often possible, however, it is common that the

full description becomes too complicated for this to be efficient; for example, the bath could represent very many degrees of freedom which may not be possible to account for exactly. Supposing that we are only interested in observations on the subsystem S, a widely adopted solution is to develop a simpler description of the subsystem S alone by discarding detailed knowledge of the reservoir and tracing over it such that the system S is described by a density matrix. A new *master equation* for the system alone can then be derived using various approximating techniques.

The Lindblad Master Equation

Throughout this thesis, the open quantum lattice models considered are described by the Lindblad master equation, for a thorough introduction the reader is referred to [23, 28]. The Lindblad master equation describes a form of the generator of the quantum dynamical semigroup that is derived under a set of approximations which we will refer to collectively as the Lindblad approximations. This set of approximations remain valid for a range of physical systems, but are perhaps most commonly appealed to in the field of quantum optics. To understand the origin and regime of applicability of the Lindblad master equation, it is instructive to discuss these approximations in turn.

To begin, we rewrite the master equation using the machinery of quantum dynamical semigroups [28]; in this setting, the evolution of the system at time $t = 0$ to a later time t can be described by a dynamical map $V(t)$ which is a map from the space of the reduced density operator into itself $V(t) : \mathcal{S}(\mathcal{H}_S) \to \mathcal{S}(\mathcal{H}_S)$, this allows for a master equation of the form $\rho_S(t) = V(t)\rho_S(0)$. Clearly, the problem is thus recast into that of finding an appropriate dynamical map $V(t)$ under some set of reasonable approximations about the character of the system and its environment.

Starting from the Hamiltonian of the full system $H = H_S + H_B + H_I$, it is first assumed that the system S is weakly coupled to the reservoir B, where the Hamiltonian

H_I describes the system-reservoir interaction; for this discussion the terms *environment*, *bath* and *reservoir* are used interchangeably and this is the so called *weak coupling limit* or *Born approximation*. The Born approximation assumes that the influence of the system on the reservoir is weak and that at any time, the state of the combined system can be represented as a tensor product $\rho(t) \approx \rho_S(t) \otimes \rho_B$.

The next assumption is the so called Markovian approximation, here it is assumed that the evolution of the state $\rho_S(t)$ at time t is only dependent on its current state such that the equation of motion is local in time. At this point, the evolution of $\rho_S(t)$ may still depend on the initial state of the reservoir, making it inconsistent with a description in the framework of dynamical semigroups. To make progress, we must assume that the timescale, τ_R over which the system's state varies appreciably, is large as compared to the timescale τ_B over which the correlations in the reservoir decay; $\tau_R \gg \tau_B$; the dynamical behaviour over times on the order of τ_B are not resolved. Finally, the so called *secular approximation* is used to render the master equation in Lindblad form.

The Lindblad master equation recurs frequently this thesis, therefore, without going into the mathematical details, we now describe its main features. As discussed in [23], the most general form of the generator of the quantum dynamical semigroup $\mathcal{L}$ is the Lindblad form and a general Lindblad master equation describing the evolution of the reduced density matrix ρ_S can be written as ($\hbar = 1$)

$$\mathcal{L}\rho_S = -i[H, \rho_S] + \sum_k \gamma_k \left(L_k \rho_S L_k^\dagger - \frac{1}{2} L_k^\dagger L_k \rho_S - \frac{1}{2} \rho_S L_k^\dagger L_k \right). \tag{1.5}$$

The first term is simply the Liouville-von Neumann equation for the evolution of the reduced density operator ρ_S with respect to a Hamiltonian H which is Hermitian and represents the unitary part of the dynamics. In general the Hamiltonian H in equation 1.5 may not be equivalent to the Hamiltonian of the subsystem S, but may instead include terms relating to the interaction of the system with the reservoir; for example

a Lamb shift is typically included in H. If the system is under the influence of a coherent drive, this is usually included as part of its unitary evolution. The second term is written as a sum over the operators L_k which are referred to as *Lindblad operators* or *jump operators*. These operators are in general non-Hermitian and can always be chosen to be traceless. The quantities γ_k are non-negative real-numbers which have the dimension of inverse time and are related to the rates of relaxation, decay or incoherent drive corresponding to the respective Lindblad operators.

In equation 1.5, it has been assumed that the terms in the Lindblad master equation are time independent and although extensions to time dependent situations are possible, they are not dealt with in this thesis and are therefore omitted from this discussion. Finally, it often convenient to collect the dissipative terms in the Lindblad master equation into a *dissipator* $\mathcal{D}(\rho_S)$ which is defined as

$$\mathcal{D}(\rho_S) \equiv \sum_k \gamma_k \left(L_k \rho_S L_k^\dagger - \frac{1}{2} L_k^\dagger L_k \rho_S - \frac{1}{2} \rho_S L_k^\dagger L_k \right). \tag{1.6}$$

1.2 Numerical Methods for Open Quantum Systems

The study of physical phenomena related to open quantum systems is greatly supported by computational physics. Often, the most interesting phenomena emerge as a result of complexity, however, this also tends to make them difficult to address either analytically or numerically. In very many cases, a semiclassical or mean field analysis is sufficient to understand the salient features of a particular model, however, in the study of large strongly correlated systems, very few models can be solved exactly and semiclassical or mean field approximations fail to capture important contributions to the physics.

The numerical investigation of large many-body quantum systems is hindered by the exponential growth of Hilbert space. Consider a many-body open quantum lattice model, as the size of the system increases, solving the Lindblad master equation using

numerically exact methods, such as diagonalisation of the Liouvillian matrix, quickly becomes infeasible. The development of tractable numerical methods is therefore crucial to make progress in this field. In this section, a few of the many approaches to numerically treating open quantum lattice models are discussed. In each case, the challenge lies in dealing with the exponential growth of the many body Hilbert space in a way which avoids discarding as much of the important information about correlations in the system as is possible, as well as in facilitating the non-equilibrium nature of the system. The reader is referred to [184] for a recent review of these methods.

Steady State vs Time Evolution When one is faced with the challenge of investigating an open quantum system, there are, broadly speaking, two different aspects of the system which can be probed; the properties of one or more of its steady states, and/or the characteristics of its dynamical evolution in time. This paradigm nurtures, again broadly speaking, two classes of numerical method or algorithm; those which calculate time dynamics and those which directly target the steady state. Time evolution algorithms typically involve the representation of the observables of a system or its state, either as a density matrix or ensemble of pure states. Following this, the state of the system or the value of its observables are integrated in time according to the master equation which generates its dynamics. To investigate steady state properties, the full, long time evolution to one or more steady states is often a good option as it also offers insight into the relaxation dynamics towards the steady state(s) as well as some loose guarantees as to the physicality of the solution. Targeting the steady state directly is also possible using techniques which are not associated with evolution in real time, for example using a variational or imaginary time evolution algorithm to optimise the state over the space of some variational manifold and with respect to some appropriate functional.

Mean Field Methods To simplify the exponential Hilbert space problem, a very common and useful approximation is the well know mean field (MF) approximation in which correlations between small individual subsystems are approximated by an average field. In its first order approximation, one lattice site is modelled exactly while the influence of its neighbours is calculated self consistently and approximated by an average external field. This simple type of MF approximation is a useful tool and often gives insight into the salient features of the model without having to resort to large scale numerics, however, it is very often an over simplification and tends to give qualitatively incorrect results in regions where inter-subsystem correlations become important—for example, near criticality. Furthermore, key aspects of quantum lattice models; entanglement, quantum information and correlations etcetera, cannot be treated at this level. Progressing beyond MF approximations in this setting is an active area of research; some works in this direction are mentioned below.

It is clear that taking steps beyond the simplest MF theory should involve the systematic inclusion of correlations between subsystems in a controlled and tractable manner. One conceptually simple way of doing so is to consider solving more than one lattice site exactly—for example in two dimensions, an $n_x \times n_y$ rectangular cluster of contiguous sites—then calculating the average field self consistently based upon the state of the cluster. This is the approach used in the Cluster Mean Field method of [88] and offers a clear systematic approach to investigating the properties of moderate sized lattices but also those of large systems via a finite size scaling. In principle, cluster based methods should work well if the typical length scale of correlations is captured by the size of the cluster, of course, this is not always guaranteed and unwanted finite size effects may prevail to large cluster sizes. The method of [103] and the similar approach of [15] make progress beyond MF theory in a more careful manner by accounting for the spatial structure of the correlation functions and feeding this back into the associated

mean-field-like equations. Another notable method is the Linked Cluster Expansion proposed in [14] which has proved useful for investigating open spin lattice models and the coherent anomaly approach of [89].

Stochastic Methods Stochastic methods are typically based on the fact that the density matrix can be represented as a statistical ensemble of pure states. By writing the initial state of an open system as $\rho(t_0) = \sum_k p_k |\psi_k(t_0)\rangle\langle\psi_k(t_0)|$, the state at future times can be found by propagation of the set pure states $|\psi_k\rangle$ rather than the full density matrix. Each of these pure state *trajectories* are less computationally costly than evolving the full density matrix but this come at the cost of having to average over many trajectories in order to reconstruct the ensemble average. In a typical situation, the system is initialised in a pure state $|\psi\rangle$ and M independent simulations are performed, giving a statistical error which scales as $\sim 1/\sqrt{M}$. For a Hilbert space of total dimension d, the computational cost of each trajectory is on the order of $O(Md)$ which is a considerable improvement over $O(d^2)$ required to evolve the full density matrix, furthermore, since each trajectory of the master equation unravelling is statistically independent the method is trivial to parallelise.

The stochastic nature of these methods comes from the inclusion of incoherent processes experienced by each trajectory; a simple routine might proceed as follows. Consider the case of a many-body spin system in a dissipative environment which is described by a Lindblad master equation, in this setting each of the trajectories will evolve according to a non-Hermitian Hamiltonian which does not preserve the norm of the pure state. Once the norm of the state drops below a previously drawn random number, a randomly chosen incoherent spin flip—a quantum jump—occurs which models the incoherent spin relaxation or dephasing [44, 45, 143]. Each trajectory typically has many discontinuous quantum jumps while the ensemble average will recover the smooth damped evolution.

Alternatively, a quantum state diffusion approach [67, 139] can be used. Here the

evolution of the trajectory is be governed by a stochastic Schrödinger equation in which the norm of the state remains at unity but the evolution is accompanied by a noise term which models random fluctuations associated to continuous measurement or some other environmental noise.

Stochastic and trajectory methods can offer advantages in situations where the density matrix ensemble average masks some of the underlying physics; for example, in so called *bistable* regimes [28], the probability distribution is bimodal and the mean field result typically has two stable solutions. While the ensemble averaged density matrix solution would have significant weight near these two mean field solutions, the individual trajectories can offer insight into switching or tunnelling dynamics between the two bistable states caused by quantum and/or thermal noise or induced by external noise. Furthermore, quantum trajectory methods benefit from well established methods restricting the state in a low entanglement region of the associated Hilbert space, for example using a Matrix Product State ansatz (see Chapter 2). Using such a representation allows access to larger system sizes, furthermore this method can benefit from the presence of incoherent dissipation which often limits the growth of entanglement in time, this is of course a key requirement for restricting the state to the low entanglement region of the system's Hilbert space; see [44] for an extensive review.

Phase Space Methods In phase space methods, the state of the system is represented represented on a phase space, for example, using a Wigner [188], Positive-P [51] or Q [26] quasi-probability representation, from there, the goal is to attempt to find classical stochastic processes for which the hierarchy of couple moments is a good approximation to that of the quantum problem. The Truncated Wigner Approximation (TWA) is a commonly used phase space method. TWA has been used very successfully in the context of driven-dissipative microcavity polariton systems in [29] and later in the context of a two dimensional BKT transition in a planar polariton microcavity [43]

and offers a remarkably good description of exciton-polariton experiments. The large rates of dissipation and relatively weak interaction strength of state of the art polariton microcavities make them an ideal candidate for treatment using phase space methods, however, for highly non-linear problems arising from strong interactions, phase space techniques often fail dramatically [66, 152]. The Positive-P representation is another phase space representation which finds utility in exploring large driven-dissipative systems, it has the useful feature that when the associated numerics remains stable, the resulting values can be considered exact, the regions of applicability of the Positive-P method in the context of the drive-dissipative Bose-Hubbard model have recently been explored in [49].

Variational Approaches Variational approaches have been very successful in closed systems, methods such as density functional theory and ground state TN algorithms are routinely used. For open quantum systems, variational techniques can also be used, here it is most natural to construct a variational principle which finds the steady state of a given model. Towards this end, a typical strategy involves parameterising the state of the system in terms of a set of variational parameters, for example $\rho = \rho(\{\alpha_i\})$, then optimising those parameters with respect to a suitable functional. Returning to the example of finding the steady state, defined by $\dot{\rho} = 0$, one possible approach is to minimise $||\mathcal{L}\rho||$ for an appropriate norm. Clearly choosing the appropriate functional is of central importance to these methods as discussed in [182, 183]. For example, if the trace norm is chosen, the evaluation of the variational functional itself is still exponential in the system size, it is however possible to construct upper bounds on the variational functional related to the degree of additional correlations that can arise due to the application of the Liouvillian to states inside the variational manifold, see [183]. Variational methods also find a utility in time evolution algorithms; for example the Time Dependent Variational Principle employs a variational integration of the master

equation [99, 137].

Machine Learning Inspired Methods Recently, the success of machine learning algorithms has made its way into the simulation of quantum lattice models. In the context of open systems a few methods inspired by machine learning have already been developed. For example, methods based on neural networks and the variational minimisation of an appropriate cost function have provided an exciting proof of concept, see for example [76, 128, 174, 192]. By representing the state as a neural network, the hidden layers introduce variational parameters which are associated to the quantum correlations of the many body state. In principle, long range connectivity possible with the neural network can allow for the inclusion of long range correlations which may give advantages over other methods where only short range correlations are retained.

Corner Space Renormalisation The Corner Space Renormalisation Method of [60] approaches the problem by restricting the Hilbert space of the open system to a corner of the full Hilbert space. To do so, the method solves the master equation using an iterative procedure which begins by finding the steady state for a small system, for example by exact diagonalisation, then, two copies of the small systems are merged and only the most probable states in the product space of the merged states are retained. Following this, the steady state of the merged system is found and the process of merging and discarding least probable state repeated. This iterative procedure can be used to simulate lattices of increasing size. As highlighted in [184], the structure of the resulting density matrix is analogous to that of a Tree Tensor Network (TTN) [158] and is therefore tailored to finite system sizes.

1.3 This Thesis

As discussed in the introductory paragraphs, recent advances in a variety of quantum computing and quantum simulation platforms have opened up new opportunities for the experimental realisation of quantum lattice models. However, for the foreseeable future, it is likely that these experimental platforms will have to contend with noise. While this noise is often an unwanted nuisance, there remain opportunities whereby the coupling of a quantum lattice model to its environment can be harnessed and engineered, leading to new technological applications and providing a new setting in which to explore fundamental physical phenomena. In these endeavours, the ability to solve open quantum lattice models on classical computers remains an indispensable tool. To circumvent the exponential growth of the system Hilbert space and move beyond the limits of exact numerical techniques, a broad array of creative approximate numerical methods have been developed, the goal of this thesis is to contribute to this array of techniques by developing efficient algorithms based on TNs, with a particular emphasis on the relatively unexplored area of two-dimensional lattice models.

Underpinned by entanglement area laws, TNs have emerged as a standard tool in the numerical simulation of closed quantum systems. Their development of the past decades has offered a new lens into the entanglement structure of many-body quantum states and provided a new framework in which the structure of these states can be understood and characterised. In the pursuit of quantum computational advantage [144], TNs have emerged as one of the most compact and powerful classical ansatze for quantum systems, so much so that the leading classical algorithms pushing at the boundaries of quantum advantage are based on large tensor network contractions; see for example [69, 82].

For one dimensional systems, the computational efficiency of TNs has already been carried over to the context of open quantum lattice models, where the handful of algorithms mentioned previously have demonstrated impressive results. In one spatial

dimension, TN methods benefit from the simple network geometry; efficient contraction of the network and convenient gauge transformations make for simple and efficient algorithms. Indeed, like in the case of closed quantum systems, the majority of TN methods for open quantum systems are intended for to study of one-dimensional systems.

In the context of two-dimensional systems, tensor network methods incur a large overhead in both computational and operational complexity such that there are very few works which are intended for the simulation of two-dimensional open quantum lattice models. In two dimensions, treatment of open quantum systems using TNs becomes a lot more challenging. Firstly, the presence of closed loops in the network mean that those simplifying methodologies associated to one-dimensional systems are no longer available, secondly, there is very often a much greater computational cost associated to contracting the two-dimensional TN. Both of these combined add significant additional complexity which means that TN methods for two-dimensional systems require a more careful treatment and additional numerical machinery. The central aim of the work in this this thesis makes progress in this direction.

In Chapter 2 TN methods are introduced from the perspective of one-dimensional closed quantum systems, in this setting, strong statements can be made in terms of entanglement and correlations about why TNs allow for an efficient representations of many-body quantum states. This is followed by a discussion of one-dimensional TNs as they are applied to open quantum systems, including an overview of the key differences to closed systems and review of some of the methods in the literature. Chapter 2 concludes with a detailed discussion of a one-dimensional TN algorithm based on the Matrix Product Operator (MPO) ansatz [171, 197] which integrates the Lindblad master equation in real time to calculate steady states and which is implemented in the framework of a Cluster Mean Field (CMF) theory[13, 88]. Chapter 3 presents the results of a brief

study on the Dissipative Jaynes-Cummings-Hubbard model [72, 155] with a two-photon drive and on a one-dimensional lattice. These results serve as both a demonstration of the TN method discussed in Chapter 2 and a study of the of the critical properties of the model.

In Chapter 4, two-dimensional TN methods are discussed and an algorithm to calculate time dynamics and steady states of a Lindblad master equation on a two-dimensional lattice is presented. In doing so, the Projected Entangled Pair Operator (PEPO) TN ansatz is discussed along with its *infinite* system counterpart the Infinite Projected Entangled Pair Operator (iPEPO) [101]; by *infinite* we are referring to a translationally invariant system in the thermodynamic limit. Details of the iPEPO algorithm form the bulk of Chapter 4 and includes a discussion of environment calculation, optimisation and gauge fixing. The chapter concludes with testing of the iPEPO algorithm for integrating a dissipative Ising model in an efficiently solvable regime and against other algorithms in the literature. In particular, we take as a starting point the work of [101] which presented a TN algorithm for calculating steady states of square lattice systems and introduced the iPEPO as an operator ansatz for the system density matrix. Importantly, the work of [101] used the so called *simple update* algorithm to integrate the master equation in real time and while this procedure is fast and efficient, the simplicity of the method means that it is not expected to properly account for the influence on spatial correlations on local dynamics, furthermore, there are concerns over the stability of the simple update algorithm in this context as outlined in [94]. This thesis introduces a new integration method which goes beyond the simple update; in particular, the key contribution of the work is a new method to truncate enlarged tensor bonds while taking into account the effect of spatial correlations. The new truncation scheme adapts existing techniques from closed quantum system tensor network literature. A so called *corner transfer matrix* (CTM) [8, 9, 130, 131] technique is used to calculate the environment of the lattice

unit cell and the particular CTM variant used here is adapted from [62]. Techniques for finding optimal tensor bond truncation known as Full Environment Truncation (FET) is adapted from [56] and a method for fixing the gauge freedom across internal bonds to the so called Weighted Trace Gauge (WTG) is also adapted from [56]. In practice, it is found that this new truncation scheme is essential for achieving accurate simulations, this is particularly true in the context of real time evolution towards a steady state where the influence of even very small spatial correlations on local dynamics accumulates in time and can have a considerable impact on the eventual character of the steady state.

Chapter 5 uses the two-dimensional TN algorithm developed in Chapter 4 to probe the properties of a dissipative and anisotropic XY-model on a square lattice. This interesting model hosts a transition parameterised by the ratio of the strength of hopping between nearest neighbour lattice sites and the strength of dissipation which takes the system from a pure product state in the limit of strong dissipation to a highly mixed state when the hopping dominates. Furthermore the model serves as an example of how mean field theories applied to open quantum systems can give qualitatively different results compared to the case where quantum correlations are accounted for.

Chapter 2

Tensor Network Methods for One Dimensional Systems

It is natural to begin an introduction to numerical TN methods by discussing their application to one-dimensional closed quantum systems. In this setting, the representation of quantum states as TNs has become an invaluable tool. As well as being a tremendously successful framework for numerical simulation, the representation of states as TNs has also proven to be a powerful tool in understanding the structure of many body quantum states. One can therefore approach an introduction from two directions. A top down approach would first consider the success of numerical methods such as the Density Matrix Renormalisation Group (DMRG) and the plethora of related algorithms which have emerged over the years, from there, one can delve into the reasons why it has worked so well. Alternatively, a bottom up approach would first identify the typical structure of quantum states associated to the so called *physical corner of Hilbert space* [78, 190] and show how representation as a TN exploits this structure and can serve as an efficient ansatz for these states.

Here we choose the latter approach. Firstly, a brief introduction to graphical TN notation is given, followed by a short discussion of correlations and entanglement which

culminates in the identification of the entanglement area law as a key feature linking TNs to quantum states. Based on these concepts, a short discussion about the prospects of simulating open quantum systems with TNs is given. The widely used TNs, the Matrix Product State and Matrix Product Operator are introduced and various types of algorithm intended for simulating open quantum systems are reviewed. Finally a simple algorithm for calculating steady states of one-dimensional systems is developed in more detail. Elements of the discussion are adapted from the various review articles [33, 53, 134, 156].

2.1 Graphical Notation

The representation of tensors using index notation quickly becomes cumbersome when more complicated TNs are being dealt with. Graphical notation greatly simplifies the representation of TNs. Illustrated in Figure 2.1, tensors are represented graphically by shapes with connected lines or legs, where the rank of a tensor is exposed by its number of connected legs. Common operations on tensors: tracing of matrices, linear maps and arbitrary contractions involving many tensors are straightforward to represent by tensors diagrams. For example, the contracted indices of a pair of tensors share a common leg and outer products of tensors have an intuitive graphical representation.

The conventions used for the graphical representation of tensor conjugation, Kronecker deltas δ, isometries and the reshaping of a tensor are illustrated in Figure 2.2. Consider the example of a singular value decomposition of a third rank tensor T, decomposed with respect to one of its legs. In Figure 2.2 (a-c) T is first reshaped such that two of its legs become one, giving it the form of a matrix. Next, the matrix T is decomposed giving the unitary matrices U and V and the diagonal matrix S, where $U^\dagger U = I$ and $V^\dagger V = I$ where we note that the second rank Kronecker delta—equivalent to the identity matrix—is represented by a line. Conjugation is represented graphically

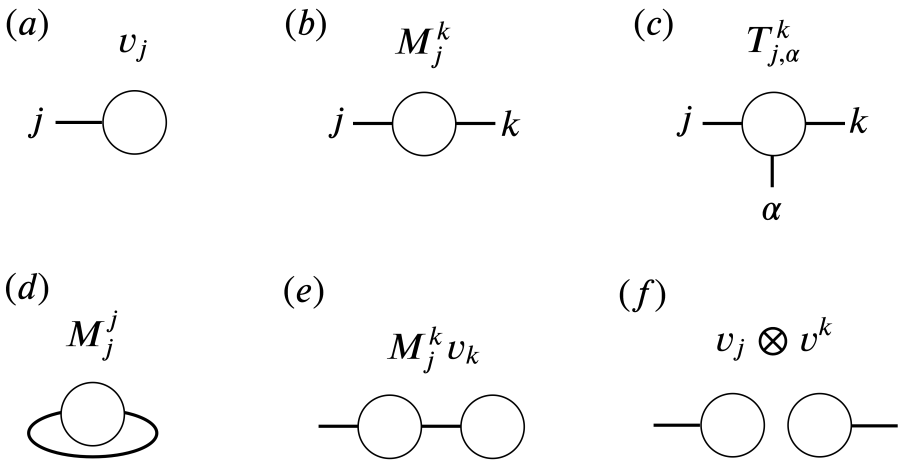

Figure 2.1: Graphical notation of TNs. (a) A vector v has one index and is represented by a shape with one leg, (b) a matrix M has two legs and (c) a third rank tensor T has three. (d) Tracing over indices results in a scalar with no legs while (e) the matrix M maps a vector v to another vector. (f) The outer product of a vector v with its transpose.

by a mirror image, where, by convention, the pointed shape assigned to isometries or unitaries makes this graphical conjugation clear.

2.2 Entanglement and Correlations

To approach the subject of TNs as they relate to quantum lattice models, it is insightful to first discuss them in the context of Hamiltonian systems. This is because certain classes of Hamiltonians are known to have ground states for which a TN ansatz is an efficient and accurate representation. For example; for the case of one-dimensional, gapped, local Hamiltonians, the ground state is known to have a particular entanglement structure, it turns out that this entanglement structure means that the state can be efficiently represented by a particular type of TN called a Matrix Product State (MPS). This section explores the connection between the entanglement structure of quantum states and their representation using TNs.

To make the discussion more concrete it is useful to recount some basic ideas from

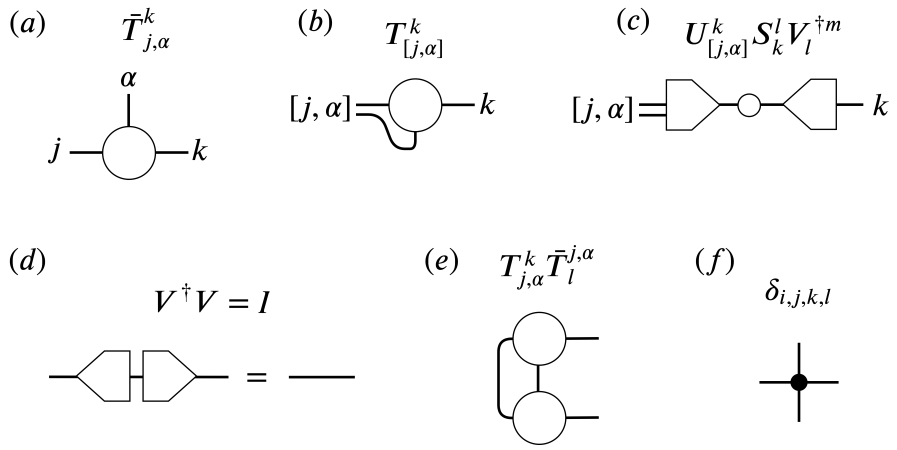

Figure 2.2: Graphical notation, reshaping, decomposition and isometries. (a) T is conjugated with respect to the index α and is represented by its horizontal mirror image $\bar{T}$. (b) Reshaping of indices. (c) Singular value decomposition of the matrix T gives the unitary matrices U and V and the diagonal matrix S. (d) Contraction of isometries give the identity matrix which is represented by a line. (e) Contraction of T and $\bar{T}$ is greatly simplified in graphical notation. (f) Representation of a fourth rank Kronecker delta.

quantum theory. For a Hamiltonian H, the ground state $|\psi\rangle$ is that which minimises the energy $E_0 = \langle\psi|H|\psi\rangle$ and lives on a ground state manifold $\mathcal{G}$ which is a subset of the full Hilbert space $\mathcal{H}$ of the Hamiltonian. The ground state can be either unique or degenerate and in the thermodynamic limit of an infinitely large system, it can either be separated by a finite energy gap ΔE to the first excited state, in which case it is said to be *gapped*, or, if there is no energy gap separating the ground state and first excited state, the system is said to be *gapless*.

The form of spatial correlation functions between different sites on the lattice tells us a lot about the structure of a state—in both classical and quantum systems. If one is dealing with a two-local Hamiltonian, then one might intuitively expect correlations to decay quickly in space; only nearest neighbour lattice sites are directly coupled to one another such that correlations between sites at a greater distance will become increasingly weak. This does indeed turn out to be the case if the local Hamiltonian is gapped. In fact, an exponential decay of correlations in gapped Hamiltonians can be

proven rigorously [111]. This statement is, however, no longer true for gapless systems where correlations instead decay algebraically. The functional form of spatial correlation functions points to some structural differences between gapped and gapless states. These differences have far reaching consequences and underpin much of our understanding of phase transitions, critical behaviour and universality. Nevertheless, for quantum many-body systems, the correlation functions tell only part of the story, to understand the structure of these states at a deeper level it is necessary to incorporate ideas from the theory of quantum information.

Quantum information theory gave rise to the notion of quantum entanglement. From Bell's inequalities to many body physics and more recently in novel quantum technologies, this uniquely quantum mechanical phenomenon has become an important concept throughout quantum physics. The application of the theory of entanglement to many-body quantum lattice models has resulted in a much more intricate understanding of the structure of complex quantum systems which are typically observed in nature. The entanglement structure is of fundamental importance in the classification of many-body quantum states and allows for the characterisation of states with no classical counterpart. As we will see, TNs have played a significant role in the development of this understanding; viewed through the lens of entanglement theory, the suitability of TNs for describing many body quantum states becomes apparent.

Consider a lattice Hamiltonian which is gapped and prepared in its pure and unique ground state ρ, a subset of lattice sites A which is separated from the rest of the lattice, which we will call B, can be described by the reduced density matrix $\rho_A = \mathrm{tr}_B(\rho)$. The Von Neumann Entropy $S(\rho_A) = -\mathrm{tr}(\rho_A \ln \rho_A)$ of the reduced system is a measure which indicates the *degree of entanglement* [12] between the subsystem A and the remainder of the lattice B; note that the Von Neumann entropy of the whole system is zero since it is a pure state. If the two subsets A and B can be decomposed as a product state,

then no quantum entanglement exists between the subsystems. A finite Von Neumann entropy on the other hand, indicates the presence of bi-partite entanglement; for this reason it is often dubbed the *entanglement entropy.*

How then does the entanglement entropy scale as the size of the lattice model increases? If ρ_A represents a subspace consisting of N_A spin-1/2 particles ($d = 2$) then $S(\rho_A)$ is maximised if ρ_A is maximally mixed

$$S(\rho_A) = -\sum_j (\eta_j \ln \eta_j) = N_A \ln d.$$

In general the von-Neumann entropy is upper bounded by $S(\rho_A) \leq |A| \ln d$ where $|A|$ denotes the size or *volume* of the subsystem ρ_A and d the size of the Hilbert space of each local system—we assume systems with finite dimensional Hilbert spaces for simplicity. It is natural to ask whether or not this bound which is extensive in the subsystem volume $|A|$ is actually reached for a typical system in the lab. Whereas a *generic* state chosen randomly from the full Hilbert space state does indeed tend to saturate the upper bound, more typical physical states, for example ground states of gapped one-dimensional local Hamiltonians, instead scale with the size of the *boundary* $|\partial A|$ between subsystems rather than its volume, this is dubbed the *entanglement area law.* While the nomenclature comes from the three-dimensional case where the area refers to that which bounds a volume, in a one-dimensional system the *area* corresponds to the boundary between the sites separating the subsystem A from the rest of the state and for a two-dimensional system, the *area* corresponds to the perimeter of the connected subsystem A

$$S(\rho_A) \propto |\partial A| \quad \text{(area law)}.$$

Some instances of area laws are well known; for example, the statement that the entanglement entropy obeys an area law can be made rigorously for the case of unique

ground states of gapped one-dimensional local Hamiltonians [79]. Other instances of area laws are also known; for instance, free fermionic and bosonic models in which the Hamiltonian can be written as a quadratic polynomial in the creation and annihilation operators [37, 141], graph states [81] and free bosonic models in dimensions greater than one [38]. The reader is referred to the review article [54] for a more complete set of examples.

On the other hand, there are known instances of states which violate entanglement area laws; for example, in one-dimensional Hamiltonians, ground state spatial correlations decay algebraically rather than exponentially when the system is gapless. In this situation, the strict area law is violated and the entanglement scaling acquires a logarithmic correction. The corrected entanglement scaling remains a sub-volume law, but is logarithmically divergent in the volume of the subsystem $|A|$. A strong relationship between the presence of an exponential decay of spatial correlations and an entanglement area law has been established [22]; the former implies the latter.

In dimensions greater than one, much less is known rigorously about the entanglement scaling of Hamiltonian ground states. Clearly, the boundary of a higher dimensional subsystem A soon becomes non trivial. Through a range of approaches, an intuition has been developed about area laws in higher dimensional systems: when one has a local gapped model with a length scale provided by the correlation function, then it is broadly expected that area laws should hold [54]. Although it is more difficult to prove strict area laws in this higher dimensional setting, there has been some progress in this direction; for example, it is possible to show that the entanglement scaling of higher dimensional models are upper bounded by an area law with at most logarithmic corrections given a sufficiently fast decay of correlations [117]. To give a more concrete example: it is known that critical, quasi-free fermionic models on a lattice violate higher dimensional area laws with logarithmic corrections, but that their bosonic counterparts do not [38].

The connection between quantum states and their representation as TNs becomes clear when we note that TN states themselves also obey an area law by construction. As will be shown in section 2.3, the well known Matrix Product State clearly obeys an entanglement area law by virtue of it's TN structure. In light of the above discussion concerning area laws, the fact that TNs provide an efficient representation of states obeying an entanglement area law is at the heart of the success of TN algorithms for numerically simulating low energy quantum states; if one reasonably expects that a particular state obeys an area law—many physically reasonable ones do—then it should be possible to find a TN ansatz which can represent that state in an efficient way. This key point is worth reiterating: although a very small subset of states in the full Hilbert space satisfy an area law, it is found that very often, states typically encountered in reasonable physical systems tend to live in and around this low entanglement subspace of the full exponentially large Hilbert space and this is precisely the subspace spanned by efficiently representable TN states.

For a long time, it was widely believed that in physically reasonable systems, area laws could be violated by at most logarithmic corrections, however, more recent studies [126] have highlighted a class of models which are deemed to be physically reasonable but violate the area law by a square root factor meaning that they are exponentially more entangled than a system obeying an area law. This class of supercritically entangled states could allow for physical system which have a much richer structure than previously thought possible and their classical simulation is likely far beyond the capabilities of state-of-the-art techniques.

Correlations and Entanglement in Open Quantum Systems

The previous discussion leading the identification of a relationship between clustering of correlations, entanglement area laws and TNs drew upon notions related to the closed

system Hamiltonian. When attempting to numerically simulate a many-body open quantum system, a natural question is to ask whether tools like TNs can be adapted to this new context. As compared to closed systems, much less is known about the nature of many-body open quantum systems and under which conditions they can be simulated efficiently on a classical computer. Drawing inspiration from closed systems in addressing these questions it is natural to consider the structure of correlations and entanglement of typical states encountered in open systems. In [190] it was shown that thermal states of local Hamiltonians obey an area law and while this result extends the notion of area laws to mixed states, thermal states do not fully cover steady states and a more tailored analysis is required. In this section, some relevant results pertaining to so called *rapidly mixing* many-body open quantum systems are briefly discussed. For a review on the issue of entanglement in open-systems, the interested reader is referred to [3].

Much like the discussion in terms of ground states of local Hamiltonians, here, the discussion is restricted to steady states of local Lindbladians—systems weakly coupled to a Markovian environment. Of course there are some basic differences between steady states and ground states to contend with, most notably is the fact that ground states are pure while steady states can be mixed. This calls for a different measure of entanglement which is appropriate for mixed states and one typically finds that the *mutual information* which measures correlations between two parts of a quantum state is used. The mutual information is advantageous in that it coincides with the entanglement entropy in the case of pure states and it upper bounds mixed state operational entanglement measures such as the distillable entanglement [12, 21].

The stability of the theoretical model defined by a Hamiltonian or Lindbladian with respect to small perturbations is crucial to its justification as a good model of the associated physical system; if the Hamiltonian or Lindbladian model depends very sensitively

on small perturbations, then it is difficult to conclude anything about the actual physical system. In [39], the authors consider local Lindbladians which correspond to the generator of the time evolution in the Lindblad approximation and which decompose into sums of local terms where the interactions decrease in strength with distance. The motivation for considering this class of system is that they model many of the types of environmental noise found in nature and therefore provide a realistic model of physical systems. For local Lindbladians it is shown that local observables and correlation functions *are* stable to perturbations, as long as the unperturbed Lindbladian has a unique fixed point and obeys what is a so called rapid mixing condition. Whereas in the case of the Hamiltonian, the nature of the gap plays a central role, in dissipative systems, a similar role is associated to the speed of convergence towards the fixed point—the mixing time. Systems for which the mixing time scales logarithmically with the systems size are denoted *rapid mixing*. The stability of such Lindbladians is good news for those seeking to numerically simulate many-body open quantum systems, however this does not yet address the structure of correlations or entanglement.

In [92], the authors provide an analysis of the correlation properties of lattice systems which have dynamics generated by sufficiently local Liouvillians with a unique steady state; local Lindbladians are a typical example of this. In particular, they show that if the Lindbladian has a spectral gap which is independent of the size of the system, then the correlation functions decay exponentially and are therefore strongly clustered and localised. It is also shown in [92] that in the case of rapidly mixing systems, the mutual information correlations decay strongly, hinting at the possibility of an entanglement area law in the presence of rapid mixing. Taking this a step further, the authors of [21] prove that for rapidly mixing dissipative quantum systems, the associated fixed point satisfies an area law with logarithmic corrections in the mutual information. If on the other hand the fixed point is pure, then the state satisfies entanglement area law in

terms of the entanglement entropy. In either case rapid mixing is the required condition for an area law and this broadly ties in with the intuition for closed quantum systems where a gapped Hamiltonian typically admits an area law.

These results seem to suggest that in many cases, fixed points of open quantum systems with local dissipators should be efficient to simulate classically using TNs. In particular, this should be the case for steady states of rapidly mixing systems which fulfil the conditions described in [21, 92]. Given a local Lindbladian for which we might expect there to be fixed point which satisfies an area law, we could conjecture that a TN such as a Matrix Product Operator or some higher dimensional network such as the Projected Entangled Pair Operator with a finite bond dimension will be sufficient to represent its stationary state to a good approximation. However, even in the case of local Lindbladians there are regions of the phase diagram where entanglement may be strong and where the TN ansatze could be pushed to their limits; for example, near critical points of dissipative phase transitions. Over recent years a variety of numerical algorithms have been proposed and successfully used to simulate many-body open quantum systems using TNs. Before reviewing them, it will be useful to introduce two commonly used TN ansatze for one-dimensional systems, the Matrix Product State and the Matrix Product Operator.

2.3 The Matrix Product State

The Matrix Product State (MPS) is the most widely used type of TN. It gets its name from its structure, a one-dimensional array of tensors which, without considering the local Hilbert space dimensions d, consist of a product of matrices as illustrated in Figure 2.3. Consider a one dimensional quantum system with N sites which is completely isolated from its environment. A general many-body wavefunction $|\Psi\rangle = c_{j_1 j_2 \cdots j_N} |j_1\rangle |j_2\rangle \cdots |j_N\rangle$ of this system can be expressed in terms a set of local

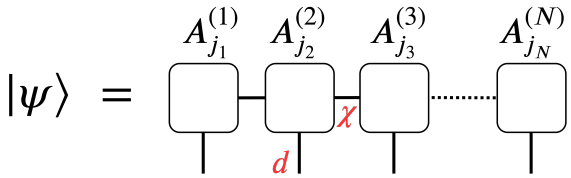

Figure 2.3: The Matrix Product State (MPS) is composed of a set of interconnected tensors with a local Hilbert space dimension d and bond dimensions χ. The left- and rightmost tensors are row and column vectors respectively.

bases at each site on the chain and an Nth-rank tensor $c_{j_1 j_2 \cdots j_N}$. The idea of the MPS representation is to break c up into a set of smaller rank tensors which are contracted as illustrated in Figure 2.3. For the case of a one-dimensional system with open boundary conditions, the left and rightmost matrices are $A^{(1)} \in \mathbb{C}^{1\times D}$ and $A^{(N)} \in \mathbb{C}^{D\times 1}$ while the remaining tensors are $A^{(n)} \in \mathbb{C}^{D\times D}$. The uncontracted dimensions shown in Figure 2.3 are associated to the local basis states.

$$c_{j_1 j_2 \cdots j_N} = \sum_{\alpha,\beta,\ldots,\omega}^{D} A^{(1)}_{\alpha;j_1} A^{(1)}_{\alpha,\beta;j_2} \ldots A^{(N)}_{\omega;j_N} = A^{(1)}_{j_1} A^{(1)}_{j_2} \ldots A^{(N)}_{j_N} \tag{2.1}$$

Each of the individual tensors in the MPS has one physical Hilbert space dimension d and one or two bond dimensions χ. The physical dimension d has a clear physical meaning: it represents the space of states of the local subsystem associated to the local tensors, for example it could represent the space of states of a spin-1/2 particle in which case $d = 2$. The bond dimension can be thought of as a variational or refinement parameters and has no direct physical significance but is instead associated to the expressibility of the ansatz; it controls how much of the full Hilbert space the MPS can represent. For an N-body spin system, the number of parameters needed to represent the state—in the tensor c—is $\mathcal{O}(d^N)$, the corresponding MPS with bond dimension D can instead be represented using $\mathcal{O}(NdD^2)$ parameters, a scaling which is linear rather than exponential in N.

The MPS is *dense* in the sense that if the bond dimension is taken large enough then the space of states it can represent will be equivalent to the full $\mathcal{O}(d^N)$ Hilbert space. In practice, the bond dimension is used as a variational parameter which controls the accuracy of the ansatz, the larger D, the greater the space of state which can be represented and the smaller the error of the approximation. In the limit of $D = 1$, the matrices become complex numbers and this is equivalent to the MF approximation. Importantly, as discussed previously, the MPS obeys an area law by construction. This can be seen by considering a subset A of contiguous sites, then, the entanglement entropy scales as $S(\rho_A) = \mathcal{O}(\log(D))$ and is therefore bounded from above by a constant in N.

In the context of numerical methods for the simulation of open quantum systems, the MPS finds utility in stochastic methods. These methods are based on the stochastic unravelling of the master equation into an ensemble of pure state trajectories. During the algorithm, each individual pure state trajectory evolves according to a non-Hermitian Hamiltonian and undergoes a stochastic jump when the norm of the state falls below a previously drawn random number. Stochastic methods based on the MPS incorporate the TN ansatz and its associated efficient time evolution techniques into the quantum trajectories algorithm. The efficiency of the MPS representation thereby extends the system sizes achievable using stochastic methods. The interested reader is referred to [44] for a review.

2.4 The Matrix Product Operator

A *matrix product operator* (MPO) introduced in [171, 197] is a TN representation of a quantum mechanical operator. The MPO can in principle represent any operator on the Hilbert space it supports, this includes a representation of the mixed state density operator ρ, in which case it is often referred to as a *matrix product density operator* (MPDO). When considered as a mixed state ansatz, the MPDO can be thought of as

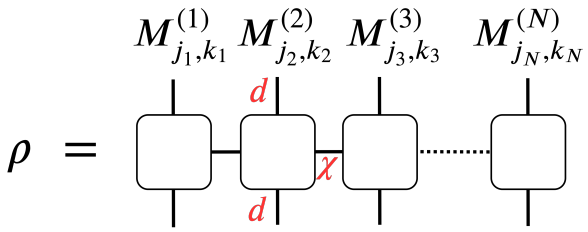

Figure 2.4: The Matrix Product Operator (MPO) is composed of a set of interconnected tensors, each with two local Hilbert space dimensions d and one or two bond dimensions χ.

a natural generalisation of the MPS to mixed sates. The general MPO O is written in terms of the tensors $M^{(n)}_{j_n k_n} \in \mathbb{C}^{D_n \times D_{n+1}}$ apart from those at the first and last site which are of size $M^{(1)}_{j_1 k_1} \in \mathbb{C}^{1 \times D_2}$ and $M^{(N)}_{j_N k_N} \in \mathbb{C}^{D_N \times 1}$ respectively. The labels j_n and k_n are associate to the local Hilbert space of the reduced density matrix at site n. An MPO with open boundary conditions is represented graphically in Figure 2.4 where the pair of local Hilbert space dimensions d are associated to each local Hilbert space and the bond dimension χ plays the same role as it does for the MPS; a variational or refinement parameter.

$$O = \sum_{j_1,\ldots,j_N}^{d} \sum_{k_1,\ldots,k_N}^{d} M^{(1)}_{j_1 k_1} M^{(2)}_{j_2 k_2} \ldots M^{(N)}_{j_N k_N} |j_1, \ldots, j_N\rangle\langle k_1, \ldots, k_N| \tag{2.2}$$

A straightforward way to construct a MPDO for which the positivity of the resulting density matrix is ensured is to use a *purification form* as explained in [171]. To do so, the individual MPO matrices $M^{(n)}_{j_n k_n}$ which are of size $D_n^2 \times D_{n+1}^2$ are constructed as sums over the tensor products

$$M^{(n)}_{j_n,k_n} = \sum_{a=1}^{d_n} A^{(n)}_{j_n s} \otimes (A^{(n)}_{k_n s})^* \tag{2.3}$$

where d_n is at most dD_nD_{n+1} and the matrices $A^{(n)}_{j_n s_n}$ are of size $D_n \times D_{n+1}$. The condition of equation 2.3 is a semidefinite condition—sufficient but not necessary—

which guarantees that the associated map is completely positive and therefore represents a physical state.

A major drawback of using the more general MPO as a representation for a mixed quantum state is that the problem instance of detecting locally whether the state of the global quantum system is positive semidefinite is NP-hard—it is undecidable in the thermodynamic limit [96]. Nevertheless, the MPO representation has been used in a number of numerical algorithms to great effect; while the positivity of the global state is not possible to guarantee efficiently, the eigenvalues of sufficiently small reduced density matrices can be checked efficiently and while the truncation of enlarged bonds can in principle cause the state to become unphysical these algorithms often work well enough.

Although the purified MPDO form appears to be a neat solution to this positivity problem, the authors of [104, 105] show that there are fundamental limitations on the representational power of the purification form; note that the A tensors in equation 2.3 are "the purification" of the M tensors. In particular, they show that there exist translationally invariant MPOs which do not possess purification MPDO forms which are valid for all system sizes [104]. Moreover, authors of [105] consider the problem of representing a MPO (represented by a set of M operators) with bond dimension D with a MPDO in purification form (represented by a set of A operators) with dimension D' and ask whether D' can be upper bounded by a function of D. They find that D' may need to be arbitrarily larger than D to represent the same state. In other words, to gain positivity guarantees via the purification form it may be necessary to pay for an arbitrarily larger bond dimension [33], nevertheless, while the purification form can be problematic for infinite systems, it is always possible to at least formally find a purification for finite size systems by diagonalising the density matrix [171].

In terms of the expressivity as an ansatz for mixed quantum states MPOs satisfy an area law by construction and it is conjectured [31] that a generic MPDO in purific-

ation form can be written as the Gibbs state of a quasi-local parent Hamiltonian and therefore will have exponentially decaying mutual information in space. In terms of representations of Hamiltonian operators, it is possible to represent Hamiltonians with up to exponentially decaying interactions using an MPO and that Hamiltonians with interactions decaying as a power law can be represented by sums of MPOs [140]. The question of the expressivity of both classical and quantum correlations of the different tensor network operator ansatze has been explored with respect to the so called *operator Schmidt rank*—the minimum bond dimension of the MPO—and its associated purification's Schmidt rank [48]. In particular, one of the issues with MPO is that the amount of classical correlations—measured by the entanglement of purification[165]—is not upper bounded by the operator Schmidt rank but by the rank of its purification [48, 105]. This throws up some issues around the interpretation of the operator Schmidt rank; for example, it can be shown [47] that any bipartite mixed state represented my a MPO with operator Schmidt rank two is separable such that it cannot describe quantum correlations. Moreover, in the case of multipartite systems it can also be shown [47] that MPOs of operator Schmidt rank two can also contain only classical correlations but that MPOs of bond dimension three can contain an unbounded amount of classical correlations; as measured by the Schmidt rank of their purification. The expressive power of various tensor network factorisations has recently been explored in [68].

The authors of [197] demonstrate a numerical algorithm based on the MPO ansatz to simulate thermal systems or integrate a generic master equation in time using a superoperator renormalisation algorithm for nearest neighbour Liouvillians. A central feature of the algorithm of [197] is the representation of the mixed state using the useful Choi isomorphism which defines a correspondence between superoperators and operators on a tensor product. In this framework, the density matrix is reshaped into a vectorised *superket* $\rho \to |\rho\rangle$ while the superoperators acting on the superket become matrix-vector

products $\mathcal{L}(\rho) \rightarrow \mathcal{L}|\rho\rangle$. The representation in this vectorised form is convenient from an operational perspective as it fits easily into time evolution algorithms such as Time Evolving Block Decimation (TEBD), for example the master equation can be integrated in real time using TEBD.

Some algorithms based on the MPO ansatz directly target the steady state. The authors of [40] make use of the fact that the steady state $|\rho_s\rangle$ of a Lindbladian defined by the superoperator $\mathcal{L}$ which satisfies the equation $\mathcal{L}|\rho_s\rangle = 0$ will also be the ground state of the Hermitian operator $\mathcal{L}^\dagger\mathcal{L}$, therefore a variational ground state search method can be used to directly find $|\rho_s\rangle$ where it will be the lowest energy eigenstate of $\mathcal{L}^\dagger\mathcal{L}$. An advantage of ground state search methods over a real time evolution methods is that the ground state search algorithm need not pass through the sequence of transient states visited by the real time evolution, some of which could be highly entangled and would therefore require a MPO with very large bond dimension to represent. This can happen even if the eventual steady state is well represented by an MPO with a small bond dimension, see for example [27]. One drawback of using the $\mathcal{L}^\dagger\mathcal{L}$ ground state search method is that this operator is in general highly non-local even if the Liouvillian $\mathcal{L}$ itself is not. A related approach was taken in [118] where the authors used an MPO based algorithm to directly search for the null vector of the Liouvillian $\mathcal{L}|\rho\rangle = 0$ using DMRG-like sweeps along the system. More recently, the authors [65] used a hybrid approach for targeting steady states of infinite one-dimensional systems based on an iMPO ansatz which represents one-dimensional systems directly in the thermodynamic limit. Their hybrid approach first uses a ground state search procedure to converge towards an approximate steady state which is the ground state of some auxiliary Hamiltonian which approximates $\mathcal{L}^\dagger\mathcal{L}$, then, starting with the resulting ground state, it uses real time evolution according to the local Liouvillian to fine tune the steady state. This two-stage approach bypasses highly entangled states associated to

the transient entangling dynamics and in some cases results in much faster convergence to the steady state.

An alternative approach to simulating thermal systems is to unitarily evolve a pure state containing an ancilla directly and then trace over that ancilla to compute the mixed state. This is achieved by attaching a local environment at each MPO site such that its purification is written as a MPS $|\Psi\rangle$. Consider for example a one-dimensional system with open boundary conditions, the purified state $|\Psi\rangle$ can be written as

$$|\Psi\rangle = \sum_{j_1,\ldots,j_N} \sum_{k_1,\ldots,k_N} A^{(1)}_{[j_1 e_1]} A^{(2)}_{[j_2 e_2]} \cdots A^{(N)}_{[j_L e_L]} |j_1 e_1 j_2 e_2 \cdots j_N e_N\rangle.$$

where the contraction over internal bonds is implicit. The MPS can be evolved using standard MPS techniques and mixed state can then be recovered by tracing over the environmental degrees of freedom of the purification, giving a density matrix ρ which is positive semidefinite by construction $\rho = \mathrm{tr}_{e_1 e_2 \cdots e_L} |\Psi\rangle\langle\Psi|$.

In [5, 58] the authors use this method to calculate spectral functions of finite temperature systems. In [80] the authors prescribe a method to find a minimally entangled representation as an MPS by iterative minimisation of the second Rényi entropy, for a given mixed state, the purification is not unique and it is therefore important to remove unnecessary entanglement.

In a slightly different but related direction, the authors of [186] present an algorithm for open quantum systems based on what they call a *locally purified tensor network* (LPTN). In this case, the state is decomposed as $\rho = X^\dagger X$ and the so called purification operator X is represented using a TN. The integration method is similar to TEBD and acts only on the purification operator, meaning that the state remains positive throughout and the mixed state ρ can be recovered at any point by contraction X with its conjugate $X^\dagger$. This method allows for the efficient simulation of open quantum lattice models of a finite size.

2.5 A Cluster Mean Field Algorithm

The important features of a typical TN algorithm are best explained by giving a detailed example of an algorithm. In this section, a simple algorithm for calculating the steady state of a one-dimensional system is discussed in detail. The method makes use of the cluster MF approach inspired by [88] and the underlying DRMG-like sweeping TEBD real time evolution algorithm incorporates a methodology similar to [197]. The method is well suited to calculating steady state properties and is used in Chapter 3 to calculate the steady state properties of a dissipative Jaynes-Cummings-Hubbard model with a two-photon drive.

The Ansatz

We represent the mixed state of the system as a MPO in vectorised form. Consider a one-dimensional chain of N sites. The local Hilbert space at each site is spanned by the set of operators $\{\sigma^{(n)}_{j_n,k_n}\}$; for example, for a chain of two level systems, these operators are the Pauli spin operators $\sigma^0 = I$, $\sigma^1 = \sigma^x$, $\sigma^2 = \sigma^y$ and $\sigma^3 = \sigma^z$. The unvectorised MPO can be written in terms of the matrices $M^{(n)}_{j_n,k_n}$ and the operators $\sigma^{(n)}_{j_n,k_n}$ as

$$\rho = \sum_{j_1,\ldots,j_N}^{d} \sum_{k_1,\ldots,k_N}^{d} M^{(1)}_{j_1k_1} M^{(2)}_{j_2k_2} \ldots M^{(N)}_{j_Nk_N} \sigma^{(1)}_{j_1,k_1} \sigma^{(2)}_{j_2,k_2} \ldots \sigma^{(N)}_{j_N,k_N}, \tag{2.4}$$

where the sum over operator basis states is suppressed, this is illustrated in Figure 2.5. The MPO is written in its vectorised form by vectorisation of the basis matrices $\sigma^{(n)}_{j_n,k_n} \to \sigma^{(n)}_{[j_n,k_n]}$ where it useful to further compress the notation such that $[j_n, k_n] \to \mu_n$ giving

$$\rho = \sum_{\mu_1,\ldots,\mu_N} M^{(1)}_{\mu_1} M^{(2)}_{\mu_2} \ldots M^{(N)}_{\mu_N} \sigma^{(1)}_{\mu_1} \sigma^{(2)}_{\mu_2} \ldots \sigma^{(N)}_{\mu_N}, \tag{2.5}$$

Figure 2.5: The mixed state is represented with a Matrix Product Operator (MPO) of bond dimension χ and a $d \times d$ local Hilbert space. In the vectorised form, the local Hilbert spaces are vectorised giving the superket $|\rho\rangle$ which is represented by a vectorised MPO with bond dimension χ and a local Hilbert space d^2.

which is illustrated in Figure 2.5. The vectorised form is very useful from an operational perspective since it has the same form as an MPS.

Mixed Canonical Form

On every internal bond of a TN, for example the TN representing $|\rho\rangle$ there exists a gauge freedom. This can easily be seen by resolving the identity matrix across each internal bond—represented graphically by a line—into a pair of isometries $\mathbb{I} = x^{-1}x$, the gauge freedom arises from the freedom to choose x. This gauge freedom allows the network to be cast in various canonical forms which often simplify algorithms considerably.

A useful canonical form which is widely used in algorithms such is the *mixed canonical form* or *multi-canonical form*. The idea is to choose an orthogonality centre which lies between two sites on the chain. All tensors to the left of the orthogonality centre are transformed to their so called *left-canonical form* while those to its right are set to their *right-canonical form*. As we will see, the mixed canonical form corresponds to performing a Schmidt decomposition across the two sites which flank the orthogonality centre, for this reason it is also often referred to as the *Schmidt form*. The mixed canonical form is widely used in numerical methods since it allows for efficient and numerically stable algorithms, furthermore it provides a clear prescription for the truncation of the Hilbert space in terms of the Schmidt components across a bipartition of the chain.

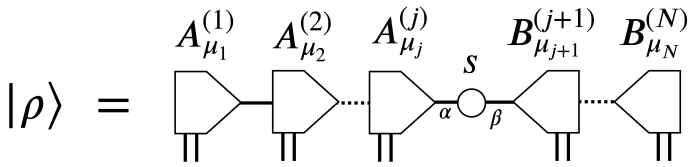

Figure 2.6: The matrix product operator can be expressed in mixed canonical form with the orthogonality centre at the location of the bond matrix s. Note that the vectorised form is used such that the pairs of vertical legs at each tensor correspond to the vectorised operators σ_{μ_n} which span the local Hilbert space at each site.

The MPO describing the full density matrix of the chain ρ is written in mixed canonical form with orthogonality centre located between sites j and $j+1$

$$\rho = \sum_{\alpha,\beta=0}^{\chi-1} \underbrace{[A^{(1)}_{\mu_1} \dots A^{(j)}_{\mu_j}]_\alpha}_{x_{L\alpha}} s_{\alpha\beta} \underbrace{[B^{(j+1)}_{\mu_{j+1}} \dots B^{(N)}_{\mu_N}]_\beta}_{x_{R\beta}} \sigma^{(1)}_{\mu_1} \dots \sigma^{(N)}_{\mu_N}, \tag{2.6}$$

where $A^{(j)}_{\mu_j}$ and $B^{(j)}_{\mu_j}$ are $\chi \times \chi$ matrices apart from those at the left and right ends of the chain, $A^{(1)}_{\mu_1}$ and $B^{(L)}_{\mu_j}$, which are $1 \times \chi$ and $\chi \times 1$ matrices respectively. The $\chi \times \chi$ matrix s is a diagonal matrix containing Schmidt components. Note that the sum over the basis operators at each site labelled by μ_j has been suppressed in equation 2.6. In Figure 2.6, the MPO expressed in mixed canonical form is shown in graphical notation—note that the vectorised form of the MPO is used and the dots imply an arbitrary number of intermediate sites.

In the following discussion it will be useful to express the tensors which are located to the left of the orthogonality centre as $\hat{x}^{[j]}_{L\alpha}$ and those to its right as $\hat{x}^{[j+1]}_{R\alpha}$ as shown in equation 2.8, note that by writing $\hat{x}_L$ and $\hat{x}_R$ with hats, contraction with the basis operators is implied. Importantly, the Hilbert-Schmidt (or equivalently Frobenius) inner product of both $\hat{x}^{[j]}_L$ and $\hat{x}^{[j]}_R$ gives the identity as shown in Figure 2.7 (a-c). Writing the **L**eft ad **R**ight tensors in this way results in a concise expression of the density matrix

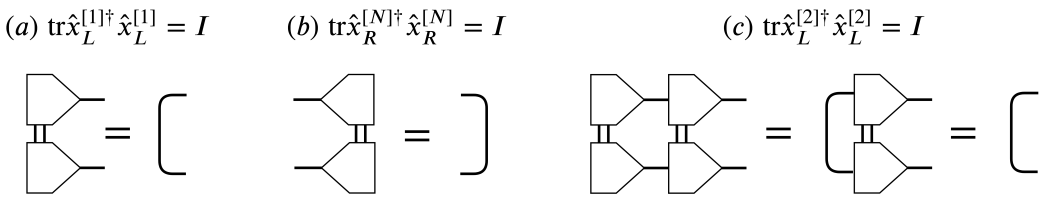

Figure 2.7: The Frobenius (or Hilbert-Schmidt) inner product of the left and right tensors $\hat{x}_L^{[j]}$ and $\hat{x}_R^{[j]}$ give the identity $\forall j$. This can be shown by considering that the tensors on the left (a) and right (b) of the chain fulfil the same condition and therefore it must be fulfilled for any site along the chain (c).

in equation

$$\rho = \sum_{\alpha=0}^{\chi-1} \hat{x}_{L\alpha}^{[j]} s_{\alpha,\beta} \hat{x}_{R,\beta}^{[j+1]}, \tag{2.7}$$

where

$$\hat{x}_{L\alpha}^{[j]} = [A_{\mu_1}^{(1)} \cdots A_{\mu_j}^{(j)}]_\alpha \sigma_{\mu_1}^{(1)} \cdots \sigma_{\mu_j}^{(j)}, \qquad \hat{x}_{R\alpha}^{[j+1]} = [B_{\mu_{j+1}}^{(j+1)} \cdots B_{\mu_L}^{(L)}]_\alpha \sigma_{\mu_{j+1}}^{(j+1)} \cdots \sigma_{\mu_L}^{(L)}. \tag{2.8}$$

Often one is required to move the orthogonality centre, for example when manipulation the TN according to some real or imaginary time evolution algorithm or to efficiently measure some local observable. A method of moving the orthogonality centre while maintaining the mixed canonical form is therefore necessary. To do this, the strategy is to define a method for moving the orthogonality centre one site to the left or one site to the right, repeated application of these left or right moves allows for the orthogonality centre to be shifted to any location along the chain. An example of method to perform a right move is given graphically in Figure 2.8.

In this work the mixed canonical form is used, however, alternative canonical forms can be used, for example, one can bring the MPS of MPO to the canonical form as prescribed by Vidal [175]. In that case, the state is decomposed by successive SVDs

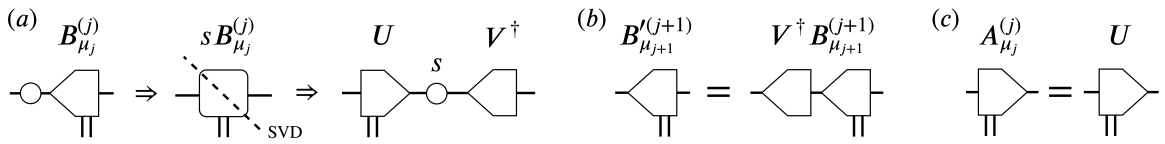

Figure 2.8: Right move of the orthogonality centre. (a) For an MPS in mixed canonical form with orthogonality centre left of site j, contract s with $B^{(j)}_{\mu_j}$, reshape the resulting tensor and perform an SVD as shown. (b) The orthogonality centre is now located left of site $j+1$, to its right is the new tensor $B'^{(j+1)}_{\mu_{j+1}}$ and (c) to its left is $A^{(j)}_{\mu_j}$.

starting at one end of the chain and progressing to the end site-by-site until the state is in a form which is represented by N tensors $\{\Gamma^{[1]}, \ldots, \Gamma^{[L]}\}$ and $n-1$ diagonal bond matrices $\{\lambda^{[1]}, \ldots, \lambda^{[L-1]}\}$. The $\Gamma^{[j]}$ at each site correspond to changes of basis between the Schmidt basis and the basis of the local Hilbert space while the entries of the diagonal bond matrices $\lambda^{[j]}$ are the Schmidt coefficients.

The canonical form of Vidal is useful from the perspective of time evolution algorithms, in particular the TEBD algorithm of [175, 176]. More precisely, the update of the state represented in canonical form by the set of Γ and λ according to a map which acts on sites l and $l+1$ only involves the update of the tensors $\Gamma^{[l]}$, $\lambda^{[l]}$ and $\Gamma^{[l+1]}$ meaning that maps can be applied in parallel rather than in left to right sweep.

A closely related canonical form for infinite one-dimensional systems can be represented by a single tensor Γ and a single diagonal bond matrix λ forming a unit cell which repeats and are referred to as infinite Matrix Product States (iMPS) or infinite Matrix Product Operators (iMPO). The various canonical forms are of central importance to any numerical TN algorithm and have been widely reviewed, see for example [134, 156].

Time Evolution and the Cluster Mean Field

The state is evolved in real time with respect to a Lindblad master equation defined by the Hamiltonian H and the set of Lindblad jump operators L using a simple sweeping Time Evolving Block Decimation (TEBD) algorithm. Starting from some initial state

ρ_0 the state at a time t is obtained by direct integration of the master equation which is equivalent to the application of the dynamical map $\rho_t = e^{t\mathcal{L}}\rho_0$. Lindbladians $\mathcal{L}$ with up to two-local interactions are considered; they decompose as a sum of terms with at most nearest neighbour interactions $\mathcal{L} = \sum_{j=1}^{L-1} \mathcal{L}_{\langle j,j+1\rangle}$. Since we are using the vectorised form of the MPO, we used the vectorised form of the Lindbladian superoperator where each of the two-site operators decompose into the coherent part of the evolution defined by the vectorised Hamiltonian $\mathcal{H}_{j,j+1}$ and the dissipative part $\mathcal{D}_{j,j+1}$ such that

$$\mathcal{L} = \sum_{j=1}^{L-1} \mathcal{L}_{j,j+1} = \sum_{j=1}^{L-1} \mathcal{H}_{j,j+1} + \mathcal{D}_{j,j+1} \tag{2.9}$$

where we note that when the vectorisation of the matrix is performed column-by-column, the resulting vectorised terms are

$$\mathcal{H}_{j,j+1} = -i\left(\mathbb{I}_{j,j+1} \otimes H_{j,j+1} - H_{j,j+1}^T \otimes \mathbb{I}_{j,j+1}\right), \tag{2.10}$$

and

$$\mathcal{D}_{j,j+1} = \frac{1}{2}\left(2L_{j,j+1}^* \otimes L_{j,j+1} - \mathbb{I}_{j,j+1} \otimes L_{j,j+1}^\dagger L_{j,j+1} - L_{j,j+1}^T L_{j,j+1}^* \otimes \mathbb{I}_{j,j+1}\right). \tag{2.11}$$

The full dynamical map $e^{\mathcal{L}t}$ is first discretised into small time steps δt as $e^{\mathcal{L}t} = [e^{\mathcal{L}\delta t}]^{t/\delta t}$ and then a second-order Trotter decomposition of the incremental gates is made giving

$$e^{i\mathcal{L}\delta t} \approx \prod_{j=1}^{L-1}\left[e^{\mathcal{L}_{j,j+1}\delta t/2}\right] \prod_{j=L-1}^{1}\left[e^{\mathcal{L}_{j,j+1}\delta t/2}\right]. \tag{2.12}$$

The terms in the first product form the rightward sweep while those in the second product contains terms in the leftward sweep. After each pair of left-right sweeps the state

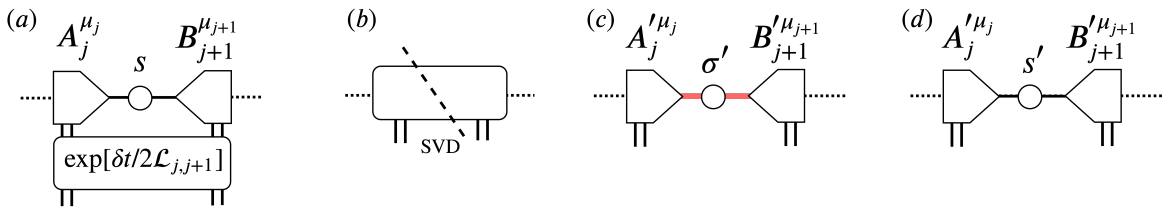

Figure 2.9: (a) Contraction of the Trotter gate with the pair of nearest neighbour tensors $A_j^{\mu_j}$ and $B_{j+1}^{\mu_{j+1}}$ with the orthogonality centre located between them, as indicated by the bond matrix s. (b) The contracted tensor is initially decomposed using a SVD giving, after reshaping, (c) the updated tensors $A_j'^{\mu_j}$, $B_{j+1}'^{\mu_{j+1}}$ and a new bond matrix $\sigma'$where in general the bond dimensions will be enlarged. (d) The enlarged bond dimension is truncated, for example by discarding singular values below some tolerance.

evolves by an amount δt with an error of order $L||h_{j,j+1}||^3\delta t^3$ where $||h_{j,j+1}||$ estimates the typical magnitude of the terms of $\mathcal{L}$. Each of the dynamical maps is calculated by direct exponentiation of the vectorised matrices $\delta t/2\mathcal{L}_{j,j+1}$ using a standard linear algebra matrix exponentiation routine.

Having constructed the sequence of dynamical maps, we now discuss how each of the two-site maps is applied to the state. Consider the update of the sties j and $j+1$ according to the map or "gate" $e^{(\delta t/2)\mathcal{L}_{j,j+1}}$. To begin the orthogonality centre is moved to site between sites j and $j+1$, then the dynamical map is contracted with the pair of tensors $A_j^{\mu_j}$ and $B_{j+1}^{\mu_{j+1}}$ as well as the bond matrix s as illustrated in Figure 2.9 (a-b). Following the contraction, the resulting tensor is decomposed using a SVD, this can be achieved by reshaping the tensor into a matrix and applying a standard routine from a numerical linear algebra library then reshaping the decomposed matrices back to their original shape. The resulting tensors are the updated $A_j'^{\mu_j}$ and $B_{j+1}'^{\mu_{j+1}}$ as well as the diagonal bond matrix σ' as illustrated in Figure 2.9 (c). In general, the bond dimension across the newly decomposed bond will be enlarged and needs to be truncated in order for the algorithm to remain efficient. Given that the update method described above leaves the network in the mixed canonical form, the diagonal entries of σ' are equivalent to the Schmidt coefficients across the associated bipartition. A straightforward truncation

scheme is therefore to retain only the χ largest terms of σ' or alternatively to discard those below some preselected tolerance. After the truncation we are left with the updated pair of tensors and the new bond matrix s' as shown in Figure 2.9 (d). In the language of equation 2.7 the truncation step is expressed as

$$\rho' = \sum_{\alpha=0}^{\chi'-1} \hat{x}'^{[j]}_{L,\alpha} s' \hat{x}'^{[j+1]}_{R,\beta} \rightarrow \rho = \sum_{\alpha=0}^{\chi-1} \hat{x}^{[j]}_{L\alpha} s_{\alpha,\beta} \hat{x}^{[j+1]}_{R,\beta} \quad \chi < \chi' \tag{2.13}$$

and minimises the Frobenius norm distance between the untruncated and truncated states. Other norms can also be used as discussed in [187], there the truncation scheme is more involved but choosing an alternative norm can ameliorate some of the issues associated with the MPO ansatz such as the loss of positivity and can allow for preservation of local conserved quantities. Here we use the simple Frobenius truncation since it is efficient and gives satisfactory results for our purposes.

A single left-right sweep is illustrated graphically in Figure 2.10. Ignoring the CMF effective fields for the moment, the left-right sweep is applied to a one-dimensional chain of L sites. Initialised in the mixed canonical form with orthogonality centre between sites $j = 1$ and $j = 2$, the first dynamical map is applied and any enlarged bonds truncated. Next the orthogonality centre is moved one step the right and the next dynamical map in the sequence given in equation 2.12 is applied. This rightward sweep of dynamical maps continues until the end of the chain is reached where the leftward sweep begins implementing the series of dynamical maps in the second product of equation 2.12. The process is repeated until the end of the end of the predefined time t is reached. One left-right sweep constitutes the evolution of the state by a time δt. For modelling finite sized systems this is all that is required, however, if we wish to perform a finite size scaling and make predictions about the behaviour in the thermodynamic limit, it can be useful to supplement dynamical evolution using a cluster MF approach.

The central idea of the Cluster Mean Field (CMF) is to expand upon the usual

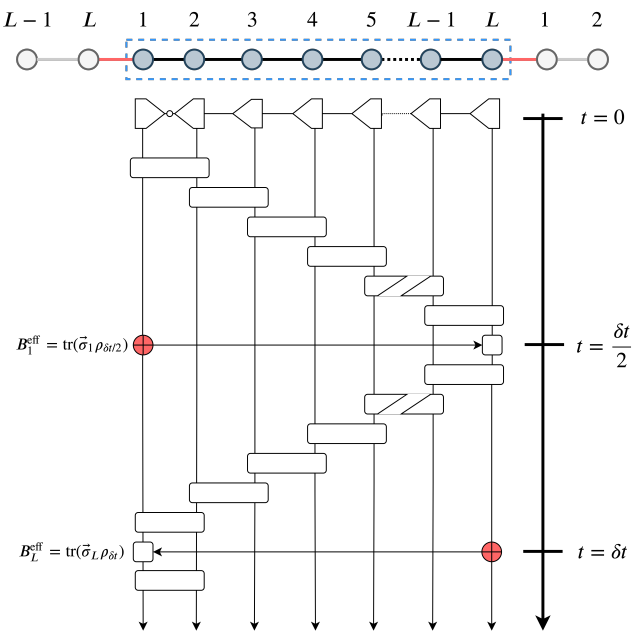

Figure 2.10: Diagram of the cluster MF approach combined with time evolving block decimation. The cluster is represented as an MPO and time evolution performed using TEBD, at the end of each left-to-right and right-to-left sweep of the time evolution, the action of the appropriate average field B_1^{eff} or B_L^{eff} is accounted for by the contraction of a single site gate at the boundaries of the cluster.

MF theory by exactly solving a cluster of sites and self consistently applying a field to the edges of the cluster. More precisely—borrowing much of the notation of [88]—considering an infinite lattice in one dimension, a subset of contiguous spins $\mathcal{C}$ (the "cluster") is isolated from the rest of the lattice, this is demonstrated in Figure 2.10, with the cluster of sites $1 \dots L$ inside the dashed bounding box. Next, the decoupled Hamiltonian of the CMF H_{CMF} is written as the sum of the Hamiltonian of the isolated cluster $H_{\mathcal{C}}$ and the Hamiltonian $H_{\mathcal{B}(\mathcal{C})}$ which describes the action of a field on the sites at the boundary of the cluster $\mathcal{B}(\mathcal{C})$. Consider for example a chain of spin-1/2 particles, then, $H_{\mathcal{B}(\mathcal{C})}$ consists of an effective field $\boldsymbol{B}_j^{\text{eff}}$ acting on the boundary spins

$$H_{\mathcal{B}(\mathcal{C})} = \sum_{j=\mathcal{B}(\mathcal{C})} \boldsymbol{B}_j^{\text{eff}} \cdot \boldsymbol{\sigma}_j. \tag{2.14}$$

The effective field $\boldsymbol{B}_j^{\text{eff}}(t) = \text{tr}[\boldsymbol{\sigma}_{j'}\rho(t)]$ is identified as the magnetisation of the spin j' which is adjacent to j and is part of the neighbouring cluster $\mathcal{C}'$. Of course, this adjacent spin is being modelled by the spin at the opposite boundary of the cluster $\mathcal{C}$. The density matrix of each cluster $\rho_{\mathcal{C}}$ is a factorisation of the global density matrix in much the same way as the usual single-site MF approach, with the only difference that each cluster may contain more than one site.

$$\rho = \bigotimes_{\mathcal{C}} \rho_{\mathcal{C}} \tag{2.15}$$

The effective master equation describing the evolution of ρ_C can then be expressed in terms of H_{CMF} as ($\hbar = 1$)

$$\dot{\rho}_{\mathcal{C}} = -i[H_{CMF}, \rho_{\mathcal{C}}] + \sum_{j\in\mathcal{C}} \mathcal{D}_j[\rho_{\mathcal{C}}] \tag{2.16}$$

In a similar way to the approach used in [88], we combine the cluster MF approach with a TN. In particular, we represent the state of the cluster $\rho_{\mathcal{C}}$ as a MPO and evolve

the state in time using the TEBD algorithm with Frobenius truncation described above. The method is neatly summarised in Figure 2.10. We initialise the state in mixed canonical form with the orthogonality centre located between the first an second sites. A discretisation and Trotter decomposition of $\exp(t\mathcal{L}_{\mathcal{C}}) = \exp(t\mathcal{L}_{CMF})$ is performed and the first Trotter gates in the left-to-right sweep is applied. Before subsequent trotter gates are applied, the effective field B_1^{eff} is measured. After the rightmost Trotter gate of the rightward sweep has been applied, the single site map describing the action of $H_{\mathcal{B}(\mathcal{C})}$ on the L^{th} lattice site—dependent on B_1^{eff}—is applied. The right-to-left TEBD sweep then commences, with the effective field B_L^{eff} measured after application of the first Trotter gate of the leftward sweep. Once the right-to-left sweep is complete the action of $H_{\mathcal{B}(\mathcal{C})}$ on the 1^{st} site of $\mathcal{C}$—dependent on B_L^{eff}—is applied. This completes one time-step δt of the sweeping TEBD algorithm combined with CMF. This approach ensures that the effective fields reflect the current state of the adjacent spins from which they are measured and avoids unnecessary movement of the orthogonality centre when measuring the effective fields.

Measurement

With the MPO representation of the density matrix at hand, the measurement of expectation values of observables is straightforward. For local observables, it is convenient to calculate the reduced density matrix as illustrated in Figure 2.11. An efficient method to calculate the reduced density matrix at site j is to first trace over the local Hilbert space dimensions of the tensors $M^{(n)}_{j_n,k_n}$ of all other sites—j's complement. Doing so results in the vectors $m^{(1)}$ and $m^{(N)}$ at each end of the chain and the matrices $m^{(j)}$ in the middle which can be efficiently contracted from the left and right leaving ρ_j. Correlations such as $\langle\sigma_j\sigma_{j+2}\rangle$ demonstrated in Figure 2.11 can also be calculated efficiently. In this case, the tensors $m^{(j)}$ are again calculated by tracing over the local Hilbert spaces

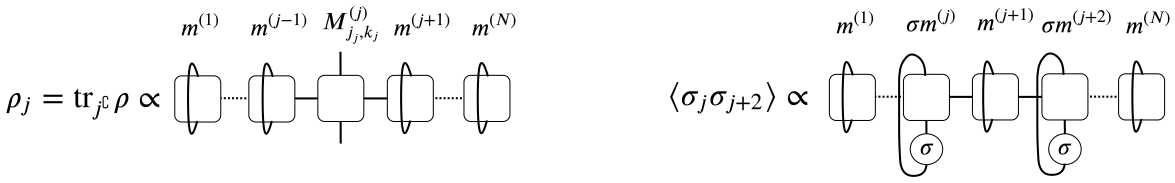

Figure 2.11: Construction of the local density matrix at the site j is done by tracing over all other sites $j^{\complement}$. The train of traced matrices $m^{(j)}$ and the vectors $m^{(1)}$ and $m^{(N)}$ at each end allow for efficient contraction of the network to calculate ρ_j. Correlations are efficiently found by calculating the $\sigma m^{(j)} = \mathrm{tr}(\sigma M^{(j)})$ and contracting with the rest of the traces tensors $m^{(j)}$ as shown for the example $\langle \sigma_j, \sigma_{j+2} \rangle$.

where at sites j and $j+2$ the operator σ is inserted in the trace giving the matrix $\sigma m^{(j)} = \mathrm{tr}(\sigma M^{(j)})$ and allows for a very efficient contraction resulting in the scalar observable. In each case it may be necessary to normalise the result by dividing by the trace of the full density matrix.

2.6 Discussion

In this chapter TNs have been introduced from the perspective correlations and entanglement in closed quantum systems. The MPS was identified as an efficient parameterisation of low energy states of one-dimensional gapped Hamiltonians. Clustering of correlations and the entanglement area law were introduced as key structural components of the MPS and central to its success as an ansatz for closed quantum lattice models. Moving to open quantum systems, the prospects for simulation of open systems was discussed in terms of rapid mixing and entanglement. A variety of methods to represent a mixed state as a TN were discussed, these included purification ansatze, the LPTN, MPDO and MPO and a selection of the associated algorithms in the literature were then reviewed. The remainder of the chapter was devoted to a more detailed account of a one-dimensional TN algorithm in the framework of a cluster mean field theory. The presentation of the algorithm served to demonstrate many of the key features of a typical

TN algorithm: canonical forms, optimisation (in this case using a DMRG-like TEBD method) and measurement.

Not discussed in detail in this chapter were the various translationally invariant formulations of one-dimensional TN algorithms, for example those based on the iMPS or the iMPO where the prefix "i" denotes "infinite". In this setting the system is thought of as the infinite repetition of a unit cell along the single dimension, while the unit cell itself is represented using one or more MPSs or MPOs, the "rest" of the system outside the unit cell to the left and right is dubbed its *environments* which can be thought of as the solutions to fixed point tensor equations representing the left and right environments. In mean field based methods the role of the environment is played by a *classical* field whereas in infinite TN methods the fixed point tensors representing the environment can encode more complex correlations in their virtual indices. Infinite TN algorithms allow for direct access to the thermodynamic limit and particularly efficient in one dimension.

As mentioned in the details of the integration scheme, the truncation of enlarged bonds in the network is a key step in any TN algorithm. Here the simplest case of Frobenius truncation was used, however there are alternative methods for finding truncations. Two notable examples are the Time Dependent Variational Principle (TDVP) of [74, 75] and the truncation with respect to alternative norms as discussed in the Density Matrix Truncation (DMT) routine of [187]. Both of these methods have the additional benefit of preserving conservation laws, at least locally and it would be interesting to consider alternative truncation schemes in the context of open quantum systems.

Chapter 3

Jaynes-Cummings-Hubbard Model with a Two-Photon Drive

3.1 Introduction

Coupled resonator arrays (CRA) are systems composed of a set of resonators which are connected to each other allowing excitations to travel between resonators. In optical CRAs photons are trapped in arrays of cavities which are naturally dissipative, without being driven by an external source any photons inside the resonator will eventually escape into the environment, the equilibrium state is therefore that of an empty resonator. There are a broad range of physical phenomena associated to optical CRAs, they tend to be inherently non-equilibrium in nature and range from fermionisation of photons to out-of-equilibrium quantum-Hall physics, see [132] or for a review.

Two closely related models of CRAs are the driven-dissipative Bose-Hubbard and Jaynes-Cummings-Hubbard models. In the context of photonic systems, the former describes an optical CRA with nearest neighbour hopping between cavities and an on-site photon-photon interaction mediated by an artificial atom or a Kerr non-linearity. In the case where the non-linearity is provided by a two level system, the model is known

as the Jaynes-Cummings-Hubbard model [72, 159]. Typically, the spontaneous emission of photons from the coupled resonator arrays of both types are replenished by a coherent or incoherent external drive. The cases of incoherent and single-photon coherent drive have been well studied and they give rise to a variety of interesting phenomena, see [132] and references therein. More recently, the case of a two-photon coherent drive, often referred to as a quadratic drive, has been considered.

Before discussing the Jaynes-Cummings-Hubbard model with a two-photon drive it is useful to briefly discuss some of the literature related to the dissipative Bose-Hubbard model with a two-photon drive. The single site version of the Bose-Hubbard model—often referred to as a Kerr resonator—has been studied in the context of a two-photon drive in [6, 7, 121]. In extended lattice systems, the quadratically driven dissipative Bose-Hubbard model, was studied in from a MF perspective [151] and later beyond MF in [147, 170]. In the usual case of a single-photon coherent drive, the $U(1)$ symmetry associated to the Bose Hubbard Hamiltonian is lifted by the drive, which rules out any spontaneous symmetry breaking in the driven-dissipative setting. The two-photon drive however, does not completely lift the symmetry, instead, the drive sets the phase of the square of resonator field leaving a discrete $\mathbb{Z}_2$ symmetry. This $\mathbb{Z}_2$ symmetry is the origin of a steady state which is characterised by a statistical mixture of Schrödinger cat-like states (see [6]) and opens the possibility for spontaneous symmetry breaking, indeed this is observed in theoretical studies of the single site Kerr resonator in for example [121] and in the MF treatment of the associated lattice system in [151].

Going beyond the MF theory of [151] the nature of the phase diagram of the dissipative Bose-Hubbard model with a two-photon drive was studied in [147]. There the authors found that the system displays critical behaviour akin to that of the finite temperature quantum Ising model suggesting that the dissipative Bose-Hubbard model with a two-photon drive can act as a quantum simulator of the quantum Ising model. In par-

ticular the authors of [147] numerically calculate steady state properties of finite size systems in one and two dimensions using the Corner Space Renormalisation method first introduced by [60]. There, a direct comparison is made with the quantum Ising model at finite temperature, a model which hosts critical phenomena. Using a finite size scaling analysis based on the critical exponents of the quantum Ising model, it is found that in the Bose-Hubbard model with two-photon drive a quantum critical point emerges in the regime of small single-photon dissipation, as long as the model is on a two-dimensional lattice. For larger rates of single-photon dissipation and for one-dimensional systems, the accompanying classical fluctuations compete with long ranged quantum correlation and the simulated system sizes are large enough to allow for sufficient classical fluctuations such that the scaling properties deviate from the universal Ising behaviour. The system therefore mimics a quantum Ising model at a finite temperature where the effective temperature is associated to the single-photon dissipation.

While it should be expected that the similarity of the two models will give rise to similar physics, the Jaynes-Cummings-Hubbard model remains qualitatively different to the Bose-Hubbard and by virtue of the extra "handle" provided by the details of the two-level system it tends to have richer physics [132]. By explicitly modelling the spin degree of freedom, the nature of the system can be explored in greater detail. For example the behaviour of defects, photonic and atomic, could be explored in the context of a quench across the transition point or in transport phenomena.

In this short chapter, a similar analysis to that of [147] is undertaken for the dissipative Jaynes-Cummings-Hubbard model with two-photon drive and on a one-dimensional lattice. Instead of using the Corner Space Renormalisation method, the CMF+MPO method described in Chapter 2 is used to calculate steady states and the work serves as a demonstration of the viability of this method for this task.

The Model

They Jaynes-Cummings-Hubbard models describes an array of optical resonators which allow photonic resonator excitations to hop to nearest neighbours. A two-level system is located in each resonator and is coherently coupled to bosonic mode of the resonator. Considering a homogeneous system where all cavities and two-level systems are the same, in the laboratory reference frame, the Jaynes-Cummings-Hubbard Hamiltonian with a two-photon drive reads

$$\begin{aligned} H_{\text{lab}} =& \sum_j \omega_c a_j^\dagger a_j + \omega_q \sigma_j^+ \sigma_j^- + g(a_j^\dagger \sigma_j^- + a_j \sigma_j^+) + \frac{G}{2}(a_j a_j e^{2it\omega_p} + a_j^\dagger a_j^\dagger e^{-2it\omega_p}) \\ & -\frac{J}{z} \sum_{\langle i,j \rangle} a_i^\dagger a_j \end{aligned} \tag{3.1}$$

where ω_c is the bare resonator frequency at each site, ω_q is the frequency of the two-level system (qubit), g is the coupling between the resonator and the qubit and G is the strength of the coherent two-photon drive of frequency ω_p. Finally the photons hop between cavities at a rate J which is homogeneous on the lattice of coordination number z. In a reference frame rotating at the frequency of the drive ω_p the Hamiltonian takes the time independent form

$$\begin{aligned} H_{\text{JCH}} =& \sum_j -\Delta_c a_j^\dagger a_j - \Delta_q \sigma_j^+ \sigma_j^- + g(a_j^\dagger \sigma_j^- + a_j \sigma_j^+) + \frac{G}{2}(a_j a_j + a_j^\dagger a_j^\dagger) \\ & -\frac{J}{z} \sum_{\langle i,j \rangle} a_i^\dagger a_j \end{aligned} \tag{3.2}$$

where the $\Delta_c = \omega_p - \omega_c$ and $\Delta_q = \omega_p - \omega_q$ are the detuning between the frequencies of the drive and resonator and that between the drive and qubit respectively. In the model both one- and two-photon incoherent losses to the environment are modelled by

a Lindblad master equation with local dissipators $\mathcal{D}[a_j]$ and $\mathcal{D}[a_j a_j]$ on each resonator

$$\dot{\rho} = -i[H_{JCH}, \rho] + \gamma \sum_j \mathcal{D}[a_j](\rho) + \eta \sum_j \mathcal{D}[a_j a_j](\rho) \tag{3.3}$$

where the rates γ and η and the one- and two-photons dissipation rates respectively.

The Hamiltonian is invariant with respect to the action of the excitation number parity operator $\Pi = \exp(i\pi \sum_j a_j^\dagger a_j + \sigma_j^+ \sigma_j^-)$ such that the Lindblad master equation 3.3 is invariant under a global change of the sign of the field operators $a_j \to -a_j \ \forall j$ accompanied by a global change of the sign of the spin raising and lowering operators $\sigma_j^+ \to -\sigma_j^+ \ \forall j$ and $\sigma_j^- \to -\sigma_j^- \ \forall j$. This is the discrete $\mathbb{Z}_2$ symmetry of the system. As will be discussed in subsection 3.1, under a MF approximation the model is expected to undergo a dissipative phase transition which is associated with a spontaneous breaking of this $\mathbb{Z}_2$ symmetry.

Single Site Picture

To form a picture of the nature of the steady state it is useful to first to solve the quadratically driven dissipative Jaynes-Cummings model achieved by setting $J = 0$ in equation 3.3. For the case of zero detuning between the resonator and the two level system, $\Delta_c = \Delta_q$ in equation 3.2, above the zero energy $\mathcal{E} = 0$ ground state $|g, 0\rangle$ the eigenstates of H_{JCH} are dressed atoms or polaritons $|n, \pm\rangle = 1/\sqrt{2}(|G, n\rangle \pm |E, n-1\rangle)$ where n labels the number of photons in the resonator and G and E are the ground and excited states of the two level system. The associated eigenenergies are characterised by the $\sqrt{n}$ splitting of the model which, in the lab frame, take values $\mathcal{E}_{n,\pm} = \omega_c n \pm g\sqrt{n}$ for $n = 1, 2, 3 \ldots$ [72].

The character of the steady state is investigated by numerically solving for the single site steady state which we label ρ_{ss}. To do this, a cutoff for the number of photons in the resonator $N_c = 20$ is introduced and the steady state of the system ρ_{ss} is calculated

using the standard numerical techniques of quantum optics, for example using the QuantumOptics.jl package of [98]. The detuning is chosen such that the two-photon driving is resonant with lowest energy excited state $\Delta_c = \Delta_q = -g$ and the coupling between the resonator and two-level system is set to $g/\gamma = 4.0$. This choice of detuning means that as the system is driven and the nonlinearity causes a blueshift of energy levels, the drive will remain at or below resonance for all drive strengths and therefore avoid any bistable behaviour which would complicate matters [102].

With ρ_{ss} in hand, the Wigner function $W(z)$ (see [6]) associated the resonator mode of the steady state $\rho^c_{ss} = \mathrm{tr}_q \rho_{ss}$ is calculated where

$$W(z) = \frac{2}{\pi}\mathrm{tr}(D_z e^{i\pi a^\dagger a} D_z^\dagger \rho^c_{ss}) \tag{3.4}$$

and $D_z = e^{za^\dagger - z^* a}$ is the displacement operator. The Wigner function plotted in Figure 3.1 (a) is bimodal in character and symmetric around $z = 0$. To get a better understanding of the nature of the state we perform a spectral decomposition of the steady state resonator mode $\rho^c_{ss} = \sum p_i |\psi_i\rangle\langle\psi_i|$ and plot the Wigner functions of the $|\psi_i\rangle$ associated to the four largest eigenvalues p_i in Figure 3.1 (b-e). The state is dominated by two cat-like states [159] which are identified by their characteristic interference pattern and are associated to the two largest eigenvalues p_1 and p_2 while the lower probability states associated to p_3 and p_4 etcetera, contribute much less to the overall resonator mode.

Mean Field Picture

Next, the MF solution to 3.3 with a non-zero hopping $J > 0$ is addressed. To do this, a cluster MF (CMF) method with a cluster size of $n_x \times n_y = 1 \times 1$ is used, where a single site of the system is solved using exact numerics again by introducing a photon number cutoff N_c and the effect of the hopping term J is calculated self consistently by introducing an effective field B_{eff} into the Hamiltonian in the same manner as described

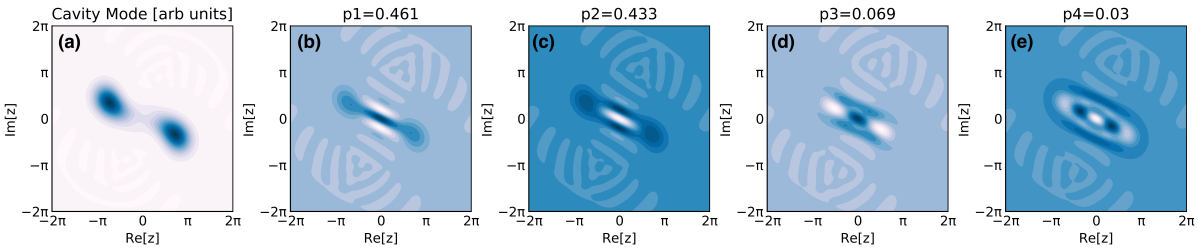

Figure 3.1: (a) Wigner function $W(z)$ of the steady state resonator mode $\rho_{ss}^c = \mathrm{tr}(\rho_{ss})$ of the dissipative Jaynes-Cummings model with two-photon drive for parameters $G/\gamma = 20$, $g/\gamma = 4.0$, $\Delta_c = \Delta_q = -g$ and equal rates of one- and two-photon loss $\eta/\gamma = 1$. (b-e) The Wigner functions $W(z)$ associated to the four largest eigenvalues of the spectral decomposition of $\rho_{ss}^c = \sum_i p_i |\psi_i\rangle\langle\psi_i|$, the state is dominated by the two cat-like states identified by their typical interference pattern in (b) and (c).

in Chapter 2.

The introduction of the hopping terms causes a shift of the energy of the resonator $\omega_c \to \omega_c - J$, therefore in order to match the resonator and qubit resonances, the detunings are set to $\Delta_c = -g - J$ and $\Delta_q = -g$. The CMF Lindblad master equation is integrated in time until good convergence of the expectation values of the field operators $\langle a \rangle$ is achieved. The photon number cutoff N_c is chosen large enough such that the operators $\langle a^\dagger a^\dagger a a \rangle$ are well converged, in practice we find that choosing $N_c = 12$ is sufficient for the parameter range of the phase diagram plotted.

The phase diagram for $g/\gamma = 4.0$, $J/\gamma \in [0, 3]$ and $G/\gamma \in [0, 5]$ is plotted in Figure 3.2. The results show a breaking of the $\mathbb{Z}_2$ symmetry in a region of the phase space indicated by a non-zero value of the local fields $|\langle a_j \rangle|$ or equivalently, a non-zero value of local spins $\langle \sigma_j^x \rangle$ and $\langle \sigma_j^y \rangle$. In the Wigner function picture, the symmetry breaking chooses one of the two lobes symmetric about $z = 0$. A linear stability analysis (not discussed) around the symmetric solution shows that it is indeed unstable in the symmetry broken regions indicated in Figure 3.2, this is also checked numerically by briefly introducing a very small one-photon drive on top of the symmetric solution and checking whether it remains stable or not.

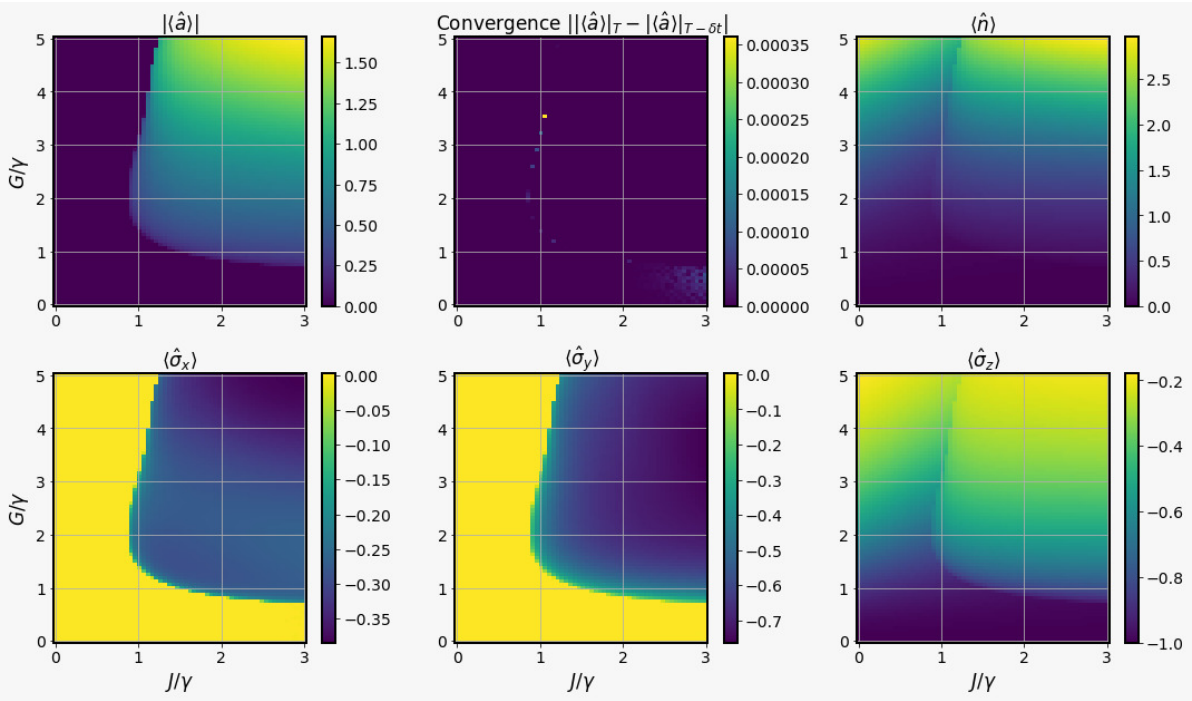

Figure 3.2: Phase diagram of the quadratically driven dissipative Jaynes Cummings Hubbard model calculated using a 1×1 CMF method. (a) The symmetry broken region is indicated by a non-zero value of the expectation value of the local field operator $|\langle a \rangle|$. The convergence in time of the results are shown in the plot of $||\langle a \rangle|_T - |\langle a \rangle|_{T-\delta t}|$ which tends to zero in the steady state. The transition to the symmetry broken phase is accompanied by a sharp increase in the resonator photon number $\langle n \rangle = \langle a^\dagger a \rangle$ as a function of G/γ. The spin expectation values show that in the symmetry broken phase $\langle \sigma^x \rangle$ and $\langle \sigma^y \rangle$ are non-zero while $\langle \sigma^z \rangle$ displays similar behaviour to $\langle n \rangle$. The data plotted are for model parameters: $g/\gamma = 4.0$, $\Delta_c = -g - J$, $\Delta_q = -g$ and $\eta/\gamma = 1$.

3.2 Research Questions

Given the close relationship between the Jaynes-Cummings-Hubbard and Bose-Hubbard models one might expect that similar behaviour to that observed for the dissipative Bose-Hubbard Model with a two-photon drive beyond MF theory in [147] should carry over to the case of the dissipative Jaynes-Cummings-Hubbard model with a two-photon drive. However, in [72], the authors compare these models under *single photon* coherent drive and find that even when the respective non-linearities are of similar strength and find that the behaviour of the models differs in most parameter regimes. This chapter investigates whether the quadratically driven dissipative Jaynes-Cummings-Hubbard and Bose-Hubbard models share the features of the former inasmuch as it can, in principle, act as a quantum simulator of the quantum Ising model. In addressing this question, the feasibility of the CMF+MPO tensor network technique for simulating such systems is also tested.

3.3 Methods

To investigate the one-dimensional phase diagram beyond MF theory we utilise the CMF+MPO method. Inspiration is taken from the work of [147] on the driven-dissipative Bose-Hubbard model with two-photon drive and we perform a finite size scaling analysis of steady state parity expectation value based on the critical exponents of the Ising model.

In particular we calculate the steady state ρ_{ss}^{L} for clusters of sizes $L \in [16, 20, 24, 28, 32]$ and examine the finite size scaling curves as outlined in the following subsection. The model parameters are chosen as $J/\gamma = 2.0$, $g/\gamma = 4.0$ $\Delta_c = -g - J$, $\Delta_q = -g$ and $\eta/\gamma = 1$ with a two-photon drive strength in the range $G/\gamma \in [0, 1]$ which coincide with a region of the MF phase diagram of Figure 3.2. For each value of G/γ, the MPO is

initialised in the product state where each resonator is in its vacuum state $|0\rangle$ and the qubits are in their $|\downarrow^z\rangle$ configuration $\rho_0 = \bigotimes_j |0_j, \downarrow_j^z\rangle\langle 0_j, \downarrow_j^z|$. The local dimension d of the field operators a, related to the maximum number of photons by $N_c = d - 1$, is set to either $d \in [3, 4]$ for the simulations. The master equation 3.3 is integrated in time using the CMF+MPO method described in Chapter 2 until the system has converged in time and with respect to the MPO's bond dimension labelled D. For each value of the two-photon drive strength G/γ, each lattice size L and each value of d, an independent simulation starting from ρ_0 is run and the bond dimension increased until convergence, in particular it is demanded that the norm of the discarded Schmidt coefficients falls below a threshold value $\epsilon_D = 10^{-6}$. A time step of $\tau\gamma = 0.01$ is chosen for all numerical results shown.

Finite Size Scaling

The scaling analysis follows the principle of Fisher and Barber [61] and the methodology of [147] and is based on a standard finite size scaling analysis in terms of the parity operator Π and the size of the MPO cluster L. The rescaled parity $\Pi L^{\beta/\nu}$ where $\Pi = \mathrm{tr}(e^{i\pi(\sum_j a_j^\dagger a_j + \sigma_j^+ \sigma_j^-)}\rho_{ss})$ is plotted as a function of the two-photon drive strength G/γ and the emergence of a critical point is indicated by the crossing of rescaled curves at a common critical point G_c. The parity expectation value decomposes as a product of local terms making its evaluation very efficient using the MPO ansatz. In the present case, the chosen critical exponents $\beta = 1/8$ and $\nu = 1$ are related to the magnetisation and correlation length of the one-dimensional quantum Ising model. Furthermore, any universal scaling of the system is investigated by observing the rescaled curves of $\Pi L^{\beta/\nu}$ plotted as a function of $(G - G_c)/\gamma L^{1/\nu}$, where universal behaviour is indicated by the collapse of the data on to a single curve.

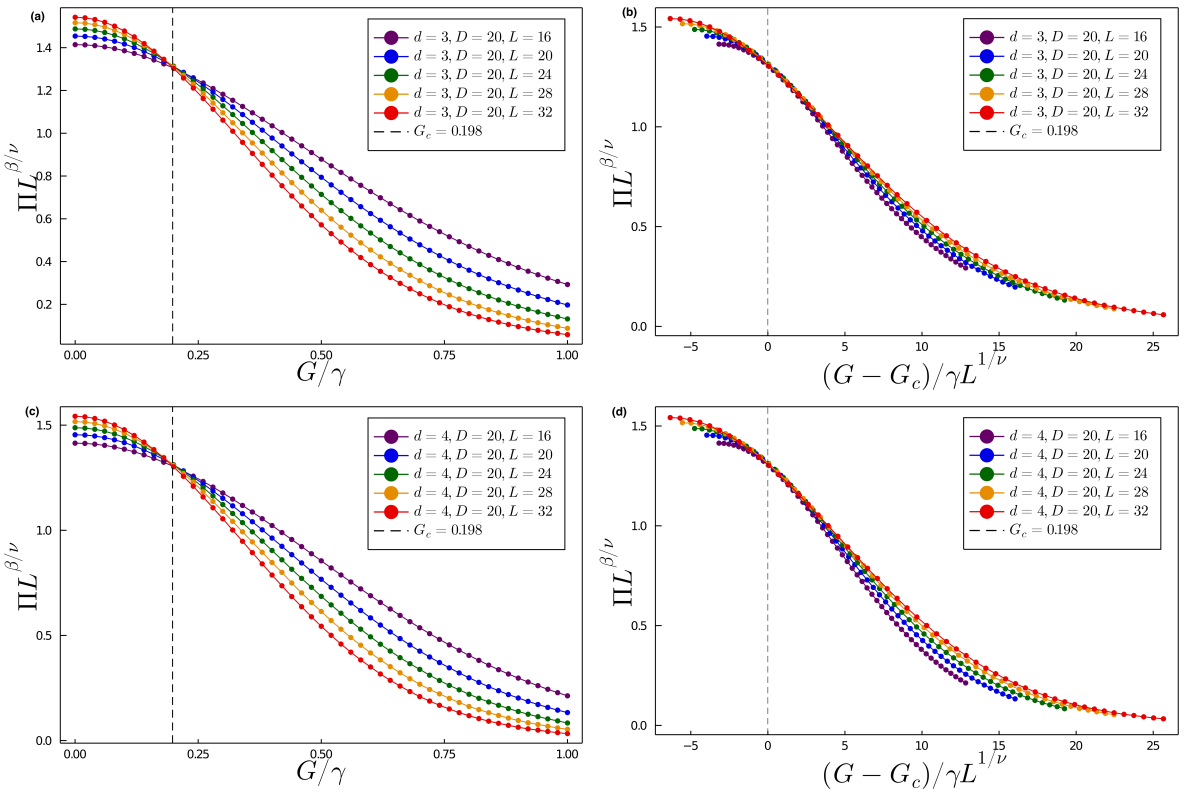

Figure 3.3: For a range of lattice sizes $L \in [16, 20, 24, 28, 32]$ the expectation value of the parity operator $\Pi = \exp(i\pi \sum_j a_j^\dagger a_j + \sigma_j^+ \sigma_j^-)$ is plotted as a function of the strength of the two-photon drive G. The values are rescaled using the critical exponent of the one-dimensional quantum Ising model: $\beta = 0.125$ and $\nu = 1$. (a) & (c) The critical drive strength is identified as the crossover point of the rescaled value $\Pi L^{\beta/\nu}$ as a function of G/γ and is estimated as $G_c \approxeq 0.198$. (b) & (d) A rescaling of the drive strength shows a partial collapse of the data in a region surrounding G_c. In (a) & (b) the local Hilbert space dimension is $d = 3$ while in (c) & (d) it has a value of $d = 4$.

3.4 Results

In Figure 3.3 the results of the CMF+MPO numerics are shown. In the left subfigure, the rescaled parity operators for the steady state density matrices of varying length L are plotted as a function of G/γ. The rescaled parity $\Pi L^{\beta/\nu}$ show a common crossing point at a critical drive strength $G_c \approx 0.198$. In the right subfigure, the rescaled parity is plotted as a function of $(G - G_c)/\gamma L^{1/\nu}$, this data shows only a partial collapse of the curves in a small region of the drive strength surrounding G_c.

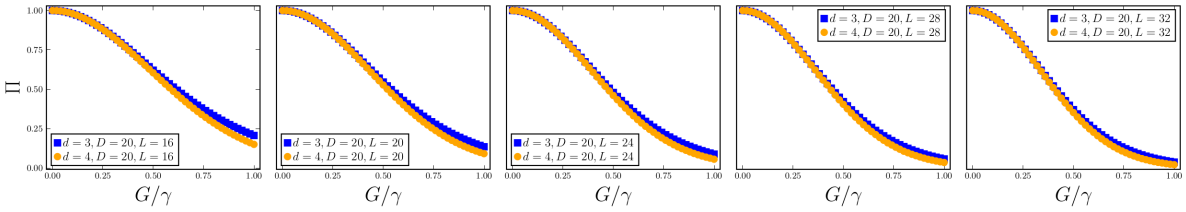

Figure 3.4: Convergence of the numerics with respect to the local Hilbert space dimension $d = N_c - 1$ for lattice sizes $L \in [16, 20, 24, 28, 32]$ and a bond dimension $D = 20$. For a boson cutoff of $N_c = 2$ ($d = 3$) the data appear well converged for drive strengths below $G/\gamma \lessapprox 0.3$.

In Figures 3.4 and 3.5 the convergence properties of the numerical results are shown. In particular, in Figure 3.4 the values of the parity expectation value as a function of the local Hilbert space dimension d is plotted for $d \in [3, 4]$ and for system sizes $L \in [16, 20, 24, 28, 32]$. These data appear well converged for drive strengths $G/\gamma \lessapprox 0.3$, for larger drive strengths the greater number of photons in each resonator demands a larger Hilbert space cutoff, nevertheless the difference between $d = 3$ and $d = 4$ is not too large for the drive strengths shown. In Figure 3.5 the convergence with respect to the bond dimension D is shown for a local Hilbert space size of $d = 3$, lattices of size $L \in [16, 20, 24, 28, 32]$ and for a range of bond dimensions $D \in [1, 10, 20, 30]$. While the correction to the MF $D = 1$ solution is significant, the data for the parity operator Π appear well converged for a very moderate bond dimensions. It is important to note that the parity operator factors into a product of local observables which tend to converge more quickly than non-local observables, nevertheless the data appear to be well enough converged for the present purpose.

3.5 Discussion

In this Chapter the CMF+MPO numerical simulation technique explained in Chapter 2 was demonstrated by solving the dissipative Jaynes-Cummings-Hubbard model with a two-photon drive on a one-dimensional lattice. It was shown that, in a similar way to

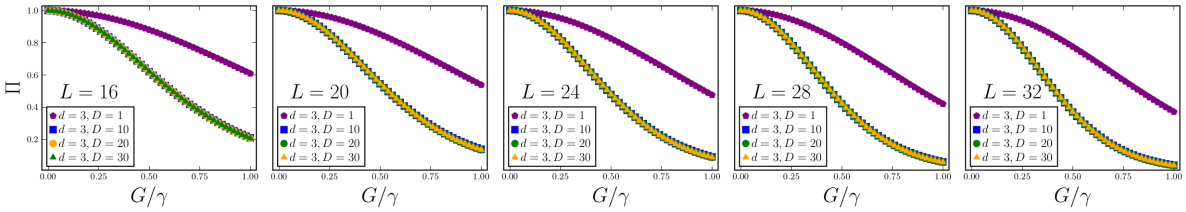

Figure 3.5: Convergence of the numerics for a lattices of size L with respect to the bond dimension D. The data for the observable Π appear well converged for the modest bond dimension of $D \gtrapprox 20$ and for drive strengths below $G/\gamma \lessapprox 0.3$.

the Bose-Hubbard model, the dissipative Jaynes-Cummings-Hubbard model with a two-photon drive on a one-dimensional lattice can in principle act as a quantum simulator of the Ising model's quantum critical point at a finite temperature. It is important to note here that these results—and also those of [147]—have assumed prior knowledge of the critical exponents and used them to fit the finite size scaling data, thereby *verifying* the nature of the critical behaviour. A more typical situation is where the critical exponents are not know a priori and this would require a much more careful analysis protocol for the results produced by the quantum simulation device. In practice, the results and conclusions drawn from quantum simulation experiments which lie beyond the reach of classical computation typically benefit from techniques such as cross platform verification which test the conclusions of quantum simulations across multiple platforms and serve to increase (or decrease) confidence in those results.

A critical drive strength is estimated at $G_c/\gamma = 0.198$ which is indicated by a common crossover point of the rescaled parity expectation value. In a small region of drive strengths surrounding G_c/γ the rescaled parity curves partially collapse, however more generally, the scaling properties of the system depart from the universal behaviour reflecting the influence of the one-photon losses on the system, an incoherent process which mimics the effect of temperature in an equilibrium system.

Given the MPO steady state representation, it would be straightforward to calculate non-local observables such correlation functions and spin structure factors which would

give more insight into the nature of the system. Interesting future directions for this work would be to examine the behaviour of the system as the rates of single photon dissipation are reduced, akin to reducing the temperature of the analogous thermal system. It would be interesting to study the system in the atomic limit of the Jaynes-Cummings-Hubbard model where the qubit component of the polariton dressed states are dominant; having this control over the qubit-resonator detuning may make the Jaynes-Cummings-Hubbard a more versatile platform for such quantum simulations. Extensions to higher photon driving fields would introduce higher order symmetries and open the possibilities of quantum simulation of spin models with larger spins $S > 1/2$. The introduction of disorder or spatial inhomogeneity of the drive could allow for studies of localisation and spin transport. Finally it would be of interest to study the properties of quenches across the transition point where defects associated to spins and bosons could be investigated.

Chapter 4

Tensor Network Methods for Two Dimensional Systems

4.1 Introduction

In Chapter 2 TNs as ansätze for one-dimensional systems were discussed. However, the idea can be generalised to higher dimensions and more complex geometries. Conceptually, the idea is simple, rather than tensors located on the vertices of a simple one-dimensional graph, arbitrary TNs can be constructed by considering tensors located on the vertices of arbitrary graphs and connected by an arbitrary set of edges. In this chapter we are concerned with TNs representing two-dimensional quantum systems and in particular TNs on cubic lattices $V = L^{\mathcal{D}}$ where $\mathcal{D} = 2$. Some of the discussion draws on the review articles of [53, 134].

The Projected Entangled Pair State (PEPS) can be though of as the natural generalisation of the MPS to two dimensions. Numerical algorithms using the PEPS as an ansatz are typically less commonly used than those based on the one-dimensional MPS ansatz, this can be attributed to two main factors, the first is that the computational cost associated with representing and manipulating the PEPS ansatz is, in general, larger

than for the MPS. This is most noticeable if we compare the computational complexity of contracting a PEPS network to contracting an MPS, whereas contraction of a MPS is efficient, contraction of a PEPS is a very computationally costly problem in the general case. The second reason is that the PEPS ansatz contains closed internal loops which mean that many of the very convenient features of the MPS, for example, the ability to define a simple canonical form, need to be revised. In the context of TN methods, the increase in spatial dimension form one to two or more is accompanied by significant additional operational complexity and tends to require more elaborate numerical machinery. Nevertheless, the PEPS ansatz has been used widely for calculating properties of two-dimensional closed quantum systems and the pace of improvements in the associated algorithms mean that the PEPS ansatz has become a valuable tool in many body physics, see for example the review article of [134].

In the context of open quantum systems, two-dimensional TN methods are much less well developed than those in one spatial dimension. This can perhaps be attributed to the same reasons that PEPS are a less commonly used ansatz: the increased complexity of contraction and more elaborate machinery required. However, these are also compounded by the extra considerations required to simulate mixed states. To our knowledge, prior to the work undertaken in this thesis, there was only one TN algorithm in the literature which dealt with two-dimensional open quantum systems. In particular the work of [101] introduced an algorithm which we will call Simple Update (SU) based on the Infinite Projected Entangled Pair Operator (iPEPO) TN ansatz for simulating steady states of two-dimensional open quantum systems. While that pioneering work provided an excellent proof of principle, issues surrounding the convergence and stability properties of the Simple Update algorithm emerged and were discussed recently in [94]. It is important to note that algorithms addressing two-dimensional thermal states also have been developed—see for example [41, 42, 100]—however, for the purposes of this

discussion we distinguish these from algorithms intended for open quantum systems of a driven-dissipative nature.

The goal of this chapter is to introduce and demonstrate a TN algorithm for two-dimensional systems based on the iPEPO ansatz which overcomes some of the limitations of the Simple Update algorithm. The chapter begins with a discussion of the Projected Entangled Pair State and its operator equivalent, the Projected Entangled Pair Operator. Following this, details of how the translationally invariant nature of the iPEPO ansatz is dealt with, in particular, the effective environments which account for the extended system are discussed. Optimisation of the iPEPO is then discussed by elaborating on a real time evolution algorithm which integrates the Lindblad master equation, this section includes many of the key developments of this work including the details of how to optimise truncation of enlarged network bonds by taking into account the influence of the effective environment. The details of how measurements are performed are given before the final section which tests the accuracy of the algorithm for calculating dynamics of a dissipative quantum Ising model and steady states of a drive-dissipative Bose-Hubbard model as well as comparing its performance to the Simple Update approach.

4.2 The Projected Entangled Pair State

The PEPS is a TN representation of a two-dimensional quantum state and can be represented graphically as in Figure 4.1. Each of the individual PEPS tensors are fifth-rank $A^{(j)}_{\alpha,\beta,\gamma,\delta;j}$ (Figure 4.1 (a)) with four bond dimensions D and one local Hilbert space dimension d. In the finite lattice of Figure 4.1 (b) all of the $A^{(j)}$ can be chosen to be different, or in the case of a translationally invariant system, the unit cell can be represented by one or more PEPS with the full system—the *infinite* PEPS (iPEPS)—formed by the repetition of the unit cell to span the plane. The PEPS gets its name from a common way of constructing the tensor: each square lattice vertex shares an

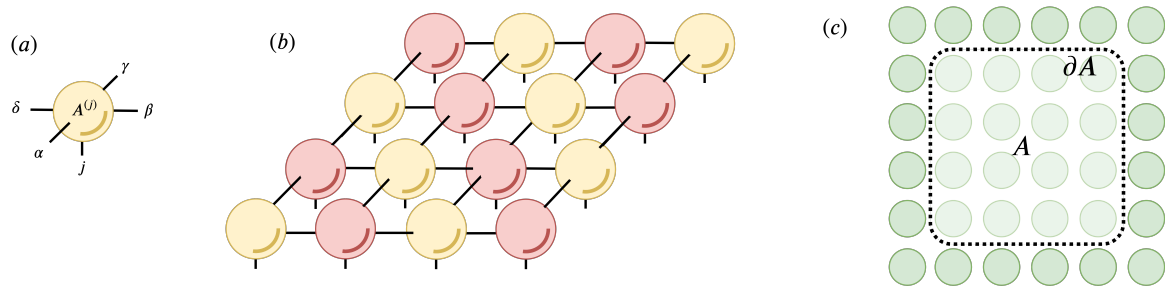

Figure 4.1: (a) Graphical representation of a PEPS tensor. (b) Finite size lattice represented as a PEPS. (c) The entanglement area law on a two-dimensional lattice, the region A is bounded by ∂A.

entangled pair with each of its neighbours. The map $P^{(k)}$ where

$$P^{(k)} = \sum_{\alpha,\beta,\gamma,\delta=1}^{D} \sum_{j=1}^{d} A^{(k)}_{\alpha,\beta,\gamma,\delta;j} |j\rangle\langle\alpha,\beta,\gamma,\delta| \tag{4.1}$$

can be said to "project the entangled pairs" shared by each site k. Many of the properties of the MPS carry over into the PEPS, for example it satisfies an entanglement area law where the boundary ∂A of a subset of sites A is proportional to the number of bonds connecting A to to its complement as demonstrated in Figure 4.1 (c). Like the MPS, the PEPS is also dense such that for a finite system, if the bond dimension D is taken large enough then the PEPS can represent any state on the full Hilbert space. One notable difference between PEPS and MPS is that a PEPS can be constructed with algebraically decaying correlations rather than just exponential [173].

Different also to the case of MPS is a lack of a strong statement about the ability of a PEPS to represent a typical physically reasonable states; for example, while we do have a strong statement about the ability of a MPS to represent ground states of gapped Hamiltonians, to our knowledge, no rigorous statement exists in two dimensions, although it is widely expected that PEPS will provide an efficient representation for ground states of gapped Hamiltonians [173]. Furthermore, the success of numerical algorithms based on the PEPS ansatz suggests that it is indeed capable of representing

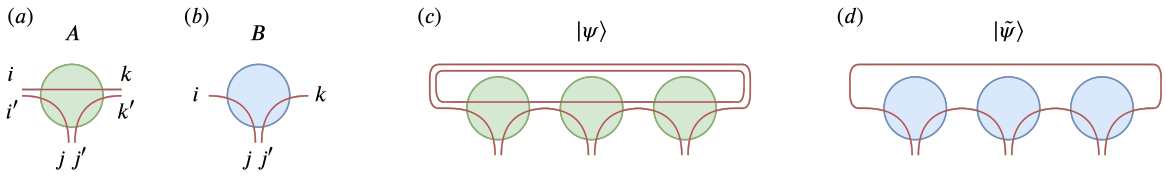

Figure 4.2: Internal correlations in a TN with closed loops. (a) The three-index tensor A forms the "sites" of a state $|\psi\rangle$ (c) for which there are internal correlations. (c) The three-index tensor B forms the state $|\tilde{\psi}\rangle$ (d) which has no internal correlations. Figure is adapted from [56].

a broad class of strongly correlated many body pure states.

One major complication generated by the two-dimensional topology of the network is that, in general, the problem instance of contracting a PEPS is contained in the computational complexity class $\sharp P$ [157]. This means that the calculation of a local observable of a state represented by a PEPS is in general very inefficient. Nevertheless, approximate contraction schemes have been developed which circumvent this problem to a large extent. Of course this is particularly relevant for infinite systems represented by the infinite Projected Entangled Pair State (iPEPS) where exact contraction is impossible. In this setting various approximate contraction techniques exist, for example tensor coarse-graining methods [73, 87], boundary MPS methods [90] and Corner Transfer Matrix (CTM) methods which will be introduced later in Section 4.3.

Internal Correlations and the Cycle Entropy

For a one-dimensional systems with open boundary conditions, described for example by a MPS or MPO, the TN ansatz has no closed loops, this is referred to as an acyclic TN. On the other hand, in higher dimensions, for example in the case of the PEPS, the TN has many closed loops; each plaquette of the square lattice forms a loop. TNs with closed loops are referred to as cyclic TNs.

Cyclic TNs host so called *internal correlations*. These are correlations which exist

in the internal structure of cyclic TN but which do not contribute to any property of the quantum state. To neatly illustrate this, the discussion from [56] is recounted as follows: Consider the three-index tensor $A_{[i,i'],[j,j'],[k,k']}$ of bond dimension $\chi = 4$ where each of the indices is a product of two smaller indices; the primed and unprimed. A can be constructed as an outer product of delta functions $A_{[i,i'],[j,j'],[k,k']} = \delta_{i,i'}\delta_{j,j'}\delta_{k,k'}$ as illustrated in Figure 4.2 (a). In a similar way, the tensor B can be constructed as an outer product of two Kronecker deltas $B_{i,[j,j'],k} = \delta_{i,j}\delta_{j',k}$ giving a bond dimension $\chi = 2$ as illustrated in Figure 4.2 (b). To elucidate the role of internal correlations it is useful to arrange the tensors A and B such that they represent the states $|\psi\rangle$ and $|\tilde{\psi}\rangle$ which are described by the TNs $\mathcal{T}$ and $\tilde{\mathcal{T}}$ respectively as illustrated graphically in Figure 4.2. Clearly, the state described by these networks is the same, however, the networks themselves are fundamentally different. The string of internal correlations demonstrated in Figure 4.2 (b) does not contribute to any property of the state $|\psi\rangle$ yet remains present in the internal structure of the network. Cutting the network $\mathcal{T}$ along one of its bonds would reveal a set of coefficients in the bond matrix which are not physically relevant since they contain information about the physically irrelevant internal correlations as well as the physical correlations associated to the quantum state. The fact that cyclic TNs host internal correlations marks a clear distinction between cyclic and acyclic TNs and is one of the sources of complexity encountered when moving from one- to two-dimensional TN algorithms.

A further complication is that the gauge of a cyclic TN cannot be fixed uniquely since it cannot be brought to a Schmidt form across a bipartition where each side of which represents an orthogonal basis, in fact a cyclic TN simply cannot be bi-partitioned across a single bond due to its topology. While a unique gauge does not exist, the author of [56] demonstrated a method of fixing the gauge of an internal bond of an arbitrary cyclic TN. The so called Weighted Trace Gauge (WTG) reduces to the Schmidt gauge

in the case of a cyclic TNs and is discussed in section 4.4.

When developing numerical algorithms based on cyclic TNs it is important to keep in mind the possible accumulation of internal correlations, while these will occupy some of the representational capacity of the TN ansatz, they do not contribute to any property of the state and should therefore be removed or reduced as fas as possible. A build up of internal correlations can lead to problems in computation and even the breakdown of algorithms, see for example [110]. The removal or minimisation of internal correlations can be done using so called disentanglers, see for example [57], however, the approach used in this work is based on the work of [56] where a method of both quantifying and removing internal correlations is prescribed. This method will be discussed more thoroughly later in this chapter.

The iPEPO Ansatz

Similar to the generalisation of the MPS the MPO, the natural generalisation of the PEPS to representing operators is the Projected Entangled Pair Operator (PEPO)[78, 94, 95, 100, 101, 123] and its translationally invariant infinite system counterpart, the iPEPO. Like the PEPS, the PEPO is in principle capable of representing algebraically decaying correlations, at least for classical models. This can be shown by observing that an *exact* representation of the classical thermal Ising model on a square lattice can be represented by a PEPO with bond dimension $D = 2$ [100] where, at criticality, the correlations decay algebraically [173]. Due to its geometry, the PEPO inherits the area law properties and complexity of contraction associated to the PEPS and is know also that PEPOs prove an efficient representation of Gibbs states of local quantum Hamiltonians [123].

The density matrix ρ of an infinite two-dimensional system can be represented by an iPEPO. The iPEPO is composed of a set of of tensors $\{A_j\}$, where we associate a

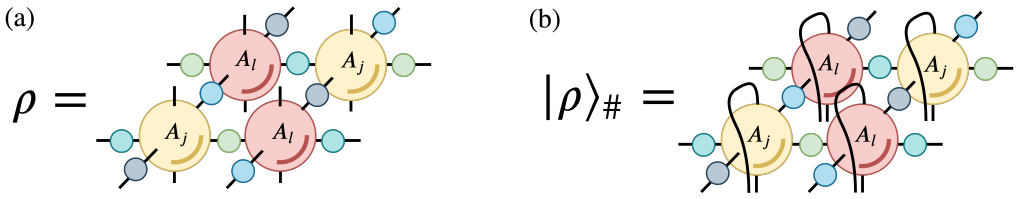

Figure 4.3: (a) The density operator ρ of a two-site unit cell of a square lattice represented by an infinite projected entangled pair operator (iPEPO). The iPEPO is composed of a set of unique tensors, in this case A_j and A_l and four unique bond matrices which are located on the bonds liking the As. (b) It is useful to work in the vectorised notation which, from an operational perspective transforms the iPEPO into the form of an iPEPS. (c) Scheme to initialise PEPO in the product state with Bloch vector $\vec{a}$ where $\vec{\sigma}$ is the matrix of Pauli operators.

tensor to each vertex of a square lattice. Assuming a translationally invariant system, it is convenient to represent only the tensors which form one unit cell of the lattice; this is demonstrated in Figure 4.3 (a). In this thesis, as a way of simplifying the algorithm, a pair of independent tensors A_j and A_l are used to represent the unit cell, although larger unit cells can also be considered via straightforward generalisations. The full system is then thought of as the repetition of this unit cell over the two-dimensional plane. Each of the sixth-rank tensors A has a pair of physical indices of dimensions d and a set of four bond indices of dimension D, which reflects the coordination number $z = 4$ of a square lattice. The physical dimension d corresponds to the dimension of the local Hilbert space at each lattice site, for a lattice of two-level spins $d = 2$. Like in the MPO, the bond dimension D is a variational parameter which controls the accuracy of the ansatz. For the purposes of the numerical algorithm, it is convenient to work with the vectorised form of the density operator. At the level of the iPEPO, this corresponds to vectorisation of the pair of local Hilbert space indices as demonstrated in Figure 4.3 (b) and has the effect of transforming the iPEPO into the form of an iPEPS. It is also useful to associate to each unique bond a *bond matrix* σ which is a diagonal matrix similar to that used in one dimensional MPS representations.

Similar to Matrix Product Operators (MPOs), the PEPO ansatz is not inherently

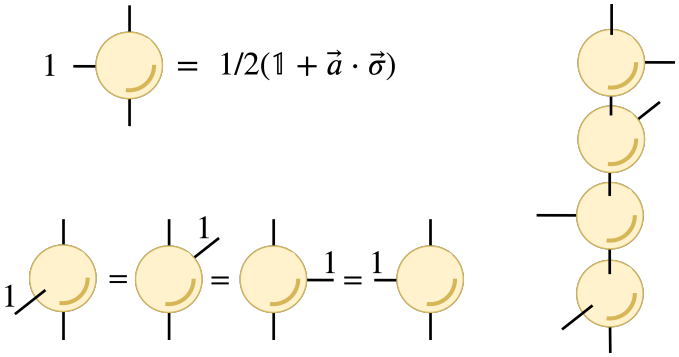

Figure 4.4: A method of initialising a PEPO in the product state with Bloch vector $\vec{a}$ where $\vec{\sigma}$ is the matrix of Pauli operators. The PEPO is constructed by contraction of four copies of the tensor.

positive and therefore not all PEPOs represent physical states. This is of particular relevance for the present case of an *infinite* PEPO where we do not have access to the full spectrum of its eigenvalues. It has been shown in the case of MPOs and discussed in chapter 2, that deciding whether a given MPO represents a physical state in the thermodynamic limit is provably undecidable, see [96]. It therefore necessary to rely on the positivity of the initial state and the dynamical maps to maintain the physicality of the iPEPO throughout the time evolution. In practice we find that, in most cases, the reduced density matrices calculated from the iPEPO, which can easily be diagonalised to check their eigenvalues, typically remain physical for larger bond dimensions.

A simple method to initialise the PEPO as a product state of spins with Bloch vector $\vec{a}$ is shown in Figure 4.3 (c), the bond matrices σ, not to be confused with the vector of Pauli operators $\vec{\sigma}$, are initialised as the identity matrix of size $D = 1$ and are not shown in the diagram. The PEPO is constructed by contraction of four copies of the same tensor.

Effective Environments

All of the spins in the system which do not form part of the *unit cell* are referred to as its *environment* (see Figure4.5). Importantly, this environment should not be confused

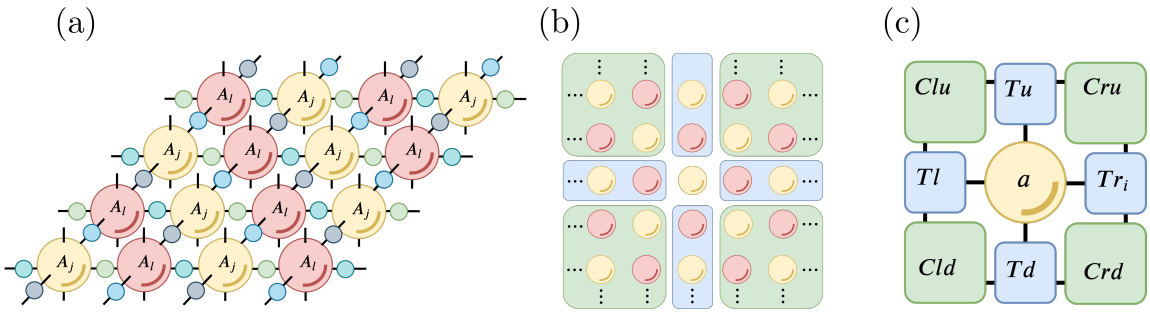

Figure 4.5: (a) The two-site unit cell of the iPEPO tiles the plane. (b) The corner transfer matrices (green) and the half-row and half-column tensors (blue) encapsulate the environment at each lattice site. (c) A single site on the lattice is surrounded by its environment.

with system's *bath* or *reservoir*, which is accounted for in the Lindblad master equation. In the thermodynamic limit of an infinite system, the unit cell tiles the plane as shown in Figure 4.5 (a), the environment is therefore all other spins on the plane which are not in the unit cell. Of course, representing this infinite set of spins exactly is not possible. A solution is to represent the environment approximately by associating to each tensor in the unit cell an *effective environment* which is denoted $\mathcal{E}$. The effective environment of each unique tensor in the unit cell $\mathcal{E}_j$ consists of a set of tensors which include four corner transfer matrices $C_{\mu\nu}$ and four half row or half column tensors T_μ, where the labels μ and ν take the appropriate first letter of left, right, up and down as illustrated in Figure 4.5 (c). These corner transfer matrices and half row and column tensors can be thought of as encapsulating the "rest" of the lattice as illustrated in Figure 4.5 (b). For the purposes of the algorithm, it is useful to consider two different types of effective environment, each playing an important role in the method, these are the *trace effective environment* $\mathcal{E}^{\text{tr}}$and the *Hilbert-Schmidt effective environment* $\mathcal{E}^{\text{hs}}$.

Trace Effective Environment

The *trace effective environment* $\mathcal{E}^{tr}$ illustrated in Figure 4.6 (d) is constructed by first tracing over the local Hilbert space dimensions d of each of the tensors in the unit cell.

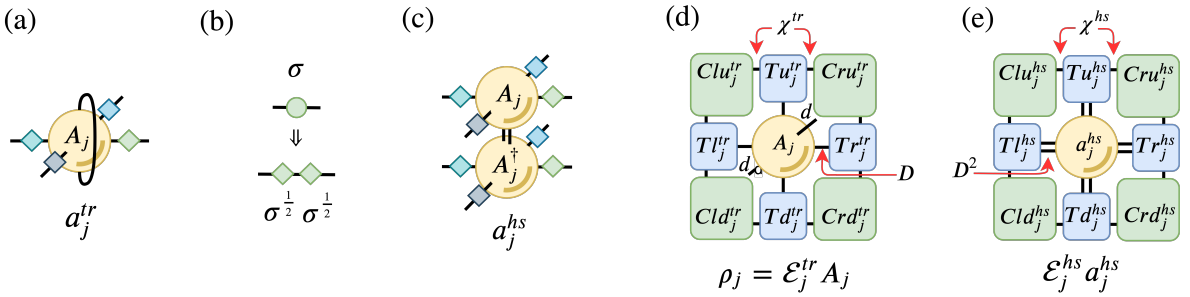

Figure 4.6: (a) At each site of the unit cell, the tensors $a_j^{tr} = \mathrm{tr}_d A_j$ are found by tracing over the physical dimensions of A_j. (b) It is useful to split the bond matrices in half by taking the square root of the diagonal matrix σ. (c) At each site of the unit cell, the tensors $a_j^{hs} = \mathrm{tr} A_j^\dagger A_j$ are found by taking the Hilbert-Schmidt inner product of A_j. (d) The unit cell tensor A_j contracted with its trace effective environment $\mathcal{E}_j^{tr}$ results in the reduced density matrix ρ_j at site j.

This gives the set of fourth-rank tensors a_j^{tr} where $a_j^{tr} = \mathrm{tr}_d A_j$ as shown in Figure 4.6 (a) where the diamond shaped matrices are square roots of the bond matrix Figure 4.6 (b). The trace effective environment is used to calculate the reduced density matrices of the system. For example, Figure 4.6 (d) corresponds to the reduced density matrix ρ_j at the lattice site j.

Hilbert-Schmidt Effective Environment

The Hilbert-Schmidt effective environment $\mathcal{E}^{hs}$ is formed by first contracting $a_j^{hs} = \mathrm{tr} A_j A_j^\dagger$ as shown graphically in Figure 4.6 (c) which gives the Hilbert-Schmidt inner product of the tensor A_i with itself. The resulting tensors a^{hs} are of eighth-rank, where all bond indices D have been left uncontracted. The Hilbert-Schmidt effective environment is used to calculate an optimal truncation of enlarged bond dimensions. The proper calculation of the effective environments is of central importance to the algorithm and indeed is usually the most numerically expensive subroutine contributing most to the overall complexity of the algorithm.

4.3 Calculating the Effective Environments

The effective environments $\mathcal{E}^{tr}$ and $\mathcal{E}^{hs}$ are calculated using a variant of the corner transfer matrix renormalisation group (). The basic idea of this approach originated with the work of [8, 9] and has undergone development through the years, most recently used in the context of classical [130, 131] and quantum [36, 62, 136] lattice systems. There are now many variants of the CTMRG algorithm which differ in their precise details. The particular variant used throughout this thesis is the one which, to our knowledge, was first developed in the work of [62]. This variant makes use of an intermediate SVD to improve the numerical stability an convergence properties. We will refer to this variant as CTMRG-SVD and give a detailed account of it in this subsection.

Consider the iPEPO consisting of the set of tensors A_j making up the unit cell, then, the idea is to find an effective environment $\mathcal{E}$ which obeys the fixed point equation

$$\mathcal{E} \times \{A_j\}_{j\in\text{unit cell}} \approx \mathcal{E}$$

up to some tolerance of convergence. In other words, we wish to find an environment $\mathcal{E}$ which represents a fixed point of a coarse graining and renormalisation procedure whereby a unit cell of the system is absorbed into the environment. This is illustrated in Figure 4.8 which shows one iteration of the coarse graining; an absorption step contracts the unit cell with the left part of the environment and a renormalisation step results in an updated representation of the environment.

The basic steps of the algorithm can be divided into three parts. First, the environment is initialised, next an absorption step is performed in one of the four directions left, right, up or down. This is followed by renormalisation of the enlarged environment tensors along the absorption direction. The absorption-renormalisation steps are repeated in all directions until the environment converges to a fixed point.

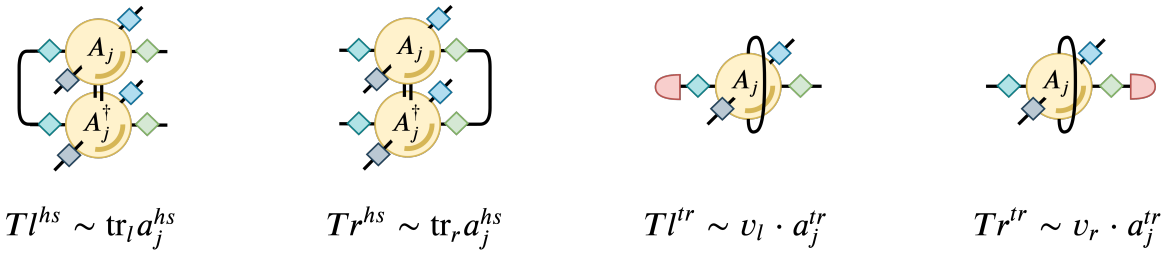

Figure 4.7: Initialisation of the half-row tensors $Tl^{\mathrm{hs}}$and Tr^{hs} using the iPEPO tensors A_j, two of the uncontracted bonds of a_j^{hs} are traced over. Initialisation of the half-row tensors Tl^{tr} and Tr^{tr} using the iPEPO tensor A_j, by defining a vector v one of the four uncontracted bonds of a_j^{tr} is contracted over.

Initialisation

An initial guess for the environment tensors can in principle be a set of random tensors of the appropriate dimensions, however this can slow done the speed of convergence, it is useful to initialise the environment tensors using the tensors of the iPEPO unit cell. Consider a set of tenors $\{A_j\}$ representing a two site unit cell as an iPEPO, arranged in a checkerboard lattice as in Figure 4.5 (a). The effective environments can be initialised using the $\{A_j\}$; for example, to initialise Tl_j^{hs}, simply contract over the left indices of a_k^{hs} as shown in Figure 4.7 (a) and normalise. The tensor Tr_j^{hs} can be initialised by tracing over the right bond and so on. To initialise $\mathcal{E}^{tr}$ one can simply contract over all but the first components of a^{tr} along the appropriate directions and normalise. For example, to initialise Tl^{tr}, retain only the first component of a^{tr} in the left direction, ie. set $Tl_j^{tr} = \sum_d v_{[l]} a_k^{tr[d,r,u,l]}$ where the vector $v = (1, 0, \ldots, 0)$ as shown in Figure 4.7 (c), the other half-row tensors are calculated in a similar way. Alternatively, one could choose the vector $v = (1, 1, \ldots, 1)$, however, we find that retaining the first component only works well enough to create an initial guess. Similarly, the corner transfer matrices can be constructed by setting for example $Clu_j^{tr} = \sum_{l,u} v_{[l]} v_{[u]} a_k^{tr[d,r,u,l]} \quad k \neq j$ etcetera. During the course of a typical algorithm where the environment is calculated at each step of the optimisation, it is very useful to re-use the effective environment from the

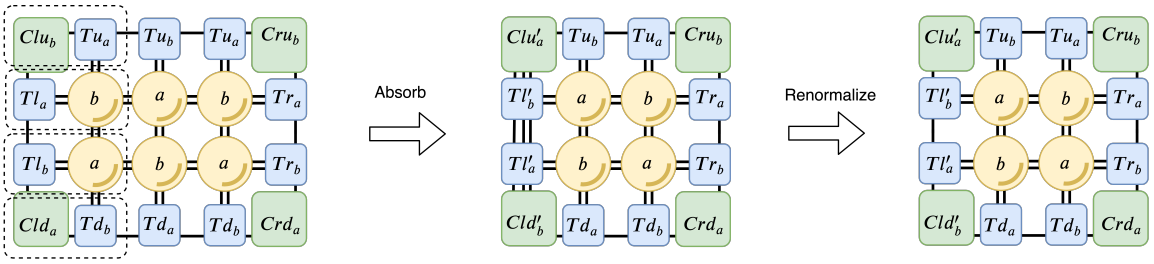

Figure 4.8: The left-move coarse graining step updates the tensors associated to the left of the environment by inserting one column of the unit cell a and b, contracting and then renormalising to find Clu'_a, Cld'_b, Tl'_a and Tl'_b. An analogous diagram made by swapping $a \leftrightarrow b$ is used to find Clu'_b and Cld'_a.

n^{th} optimisation step to initialise the effective environment of the $n+1^{th}$, this becomes possible if the gauge of the network is properly fixed, a topic will will be discussed later.

Left-Move

After initialisation, the CTMRG-SVD algorithm proceeds by performing a so called **left-move**, which updates those tensors associated with the left part of the environment Clu, Cld and Tl, as illustrated graphically in Figure 4.8. The left-move can be thought of as inserting a column of the unit cell tensors a and b, absorbing them into the left environment tensors Clu', Cld' and Tl' before renormalising them by projecting the dimension of the enlarged bonds back to their original size and normalising the magnitude of the each tensor's components. To aid the presentation of the left-move subroutine, Figure 4.9 shows the basic steps involved in the left-move graphically. In particular the following steps are associated to the left-move routine used to calculate $\mathcal{E}^{hs}$, the calculation of $\mathcal{E}^{tr}$ is almost identical.

1. Label the tensors $a^{hs}_j \rightarrow a$ and $a^{hs}_k \rightarrow b$.

2. By means of tensor contraction, construct the upper and lower half system transfer matrices and decompose using a SVD to find the upper and lower decompositions $Uu_a Su_{ab} Vu^\dagger_b$ and $Ud_a Sd_{ab} Vd^\dagger_b$; Figure 4.9 (a).

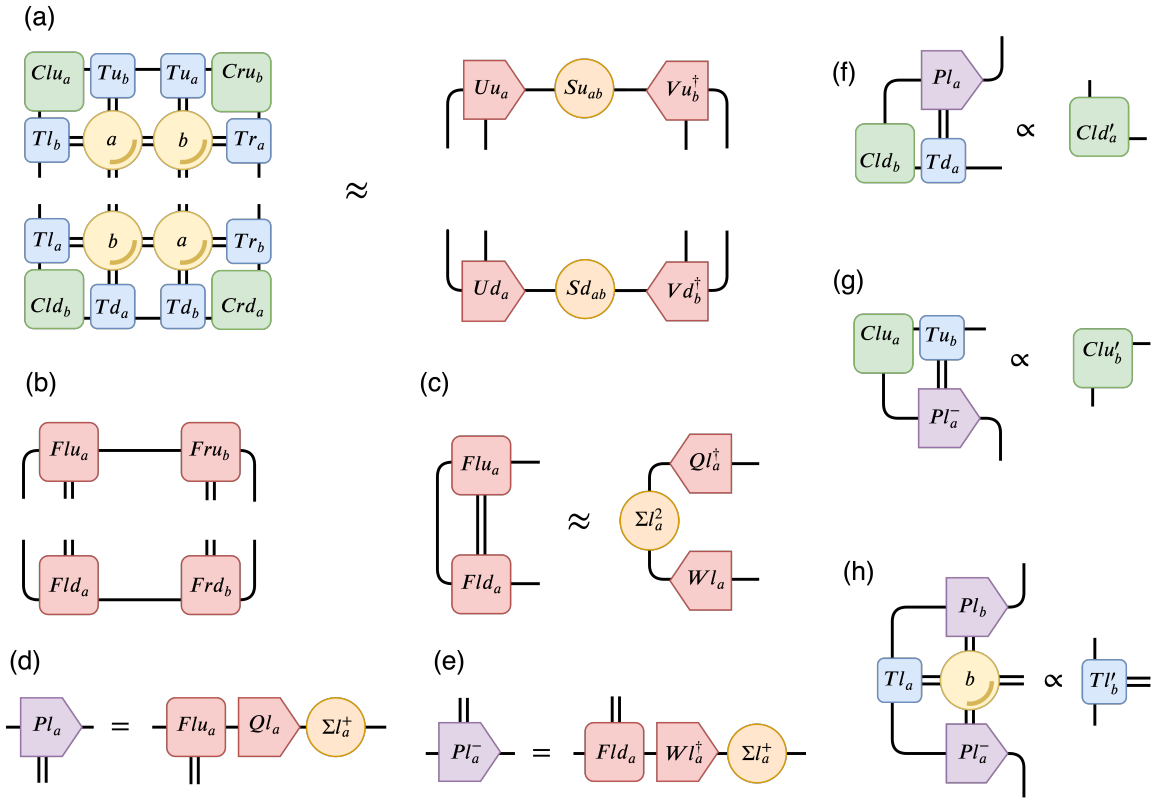

Figure 4.9: Steps involved in the left-move subroutine of the CTMRG algorithm with an intermediate SVD. (a) The upper and lower half-system transfer matrices are constructed and the first (intermediate) SVD is performed as shown. (b) The tensors $Flu_a \equiv Uu_a Su_{ab}^{1/2}$, $Fru_a \equiv Su_{ab}^{1/2} Vu_a^\dagger$, $Fld_a \equiv Ud_a Sd_{ab}^{1/2}$ and $Frd_a \equiv Sd_{ab}^{1/2} Vd_a^\dagger$ are calculated. (c) Next, the matrices Wl_a, Ql_a and the diagonal matrix Σl_a^2 are found. (d) and (f). The projectors $Pl_a = Flu_a Ql_a \Sigma l_a^+$ and $Pl_a^- = Fld_a Wl_a^\dagger \Sigma l_a^+$ are found and used in (e) (g) and (h) to find the updated environment tensors.

3. Define the tensors $Flu_a \equiv Uu_a Su_{ab}^{1/2}$, $Fru_a \equiv Su_{ab}^{1/2} Vu_a^\dagger$, $Fld_a \equiv Ud_a Sd_{ab}^{1/2}$ and $Frd_a \equiv Sd_{ab}^{1/2} Vd_a^\dagger$, where singular values of some small relative tolerance are truncated; Figure 4.9 (b).

4. Use the so called *biorthogonalisation* procedure (see [62] for further details) to calculate Pl and Pl^-. The first step is to contract Flu_a with Fld_a and perform a SVD to find Wl_a, Ql_a and the diagonal matrix Σl_a^2; Figure 4.9 (c).

5. Calculate the projectors $Pl_a = Flu_a Ql_a \Sigma l_a^+$ and $Pl_a^- = Fld_a Wl_a^\dagger \Sigma l_a^+$. Here the $+$ notation in Σl^+ denotes the Moore-Penrose pseudoinverse of Σl with a tolerance ; Figure 4.9 (d) and (f).

6. Repeat steps (d-j) to calculate Pl_b and Pl_b^- by replacing $a \leftrightarrow b$ in the upper and lower half system transfer matrices.

7. Using all of the projectors found, calculate the updated environment tensors Tl'_b, Tl'_a, Clu'_a, Clu'_b, Cld'_a, Cld'_b and normalise; Figure 4.9 (e), (g) and (g).

This completes on iteration of the left-move subroutine.

right-, up- and down-move

After the left-move subroutine is complete, the next step is to perform a right-move subroutine. The right-move involves inserting a column of tensors and absorbing from the right in order to update the tensors associated to the right side of the effective environment. Similarly, there are up-move and down-move subroutines. These four subroutines are repeated in sequence until convergence of the corner transfer matrices is achieved. In particular, the criterium for convergence used here is to demand that the norm of the difference between the vectors of singular values of all of the corner tensors between steps falls below some small tolerance . More precisely, after step $s+1$, test the inequality $|c^s - c^{s+1}| < \epsilon_\chi$ where the c^s denote the vectors of singular values

of the corner transfer matrices at step s and the inequality is tested over all unique corner transfer matrices. We have found that it is useful to set $\epsilon_{svd} \approx 10^{-3}\epsilon_{pinv}$ and is is convenient to perform **right-move** at the same time as **left-move** by following the biorthogonalisation routine starting with Fru_b and Frd_b calculated in step (b) above, similarly for **up-move** and **down-move**. A similar sequence of steps is used to perform the **right-move**, **up-move** and **down-move** steps in CTMRG-SVD.

Larger Unit Cells

The above presentation of the CTMRG-SVD algorithm is based on a iPEPO with a two site unit cell. It is straightforward to extend the algorithm to larger unit cells with a few modifications. For a unit cell of size $L_x \times L_y$ there will be $N = L_x \times L_y$ unique environment tensors of each type; $4N$ corner transfer matrices and $4N$ half-row and half-column tensors, one unique environment for each independent tensor in the unit cell. The associated left and right-moves will correspond to the insertion, absorption and renormalisation of one full $L_x \times L_y$ unit cell, resulting in L_x absorption steps. Similarly, the up- and down-moves will have L_y absorption and renormalisation steps.

Complexity

For a typical algorithm based on iPEPS or iPEPO, the principal contribution to the computational complexity comes from the calculation of the effective environment. This is particularly true if it is calculated at each optimisation or time evolution step. The leading cost of the version of the CTMRG-SVD used here arises from a singular value decomposition of order $O(\chi^3 D^6)$ in step (a) of Figure 4.9. Improvements in performance can therefore be achieved by optimising this step, for instance making sure that the optimal contraction pattern is used can help here. Alternatively, one can consider using another renormalisation algorithm or a fixed point method such as the FPCM of [62].

Lastly it is noted that there are other ways of representing the effective environment such as approximating the effective environment by using a boundary MPS to represent the boundary of the system. In this vain, a number of algorithms can be used to calculate the fixed point of an MPS, for example using time-evolving block decimation (TEBD) [135, 175] or the more advanced variational MPS-tangent space methods (VUMPS) [62, 75, 129, 168, 195]. Fixed point methods can lead to a significant speed up, particularly for systems which are close to being critical [62].

4.4 Optimisation

The optimisation of the network is performed using a Time Evolving Block Decimation (TEBD) algorithm. This algorithm is commonly used to fine ground states of Hamiltonians via imaginary time evolution or to generate dynamics via real time evolution. In the current setting of open systems we are either interested in evolving the system from some initial state towards a steady state via real time evolution or using imaginary time evolution to anneal an infinite temperature maximally mixed state down to low temperatures using imaginary time evolution. In principle it is also be possible to find the steady state directly by searching for the ground state of the Hermitian operator $\mathcal{L}^\dagger\mathcal{L}$, for example, via imaginary time evolution, however the object $\mathcal{L}^\dagger\mathcal{L}$ tends to be highly non-local and more difficult to use in the context of a standard TEBD algorithm. To make the discussion concrete, we will consider the case of an open quantum system with dynamics generated by two local Liouvillian $\mathcal{L}$ and restrict the discussion to real time evolution, imaginary time evolution for the calculation of thermal states can be considered a simplification of this.

Dynamical Map

Starting from some initial state ρ_0, time evolution is obtained by the application of the dynamical map $\rho_t = e^{t\mathcal{L}}\rho_0$ where t is a real number in the case of real time evolution. The Liouvillian superoperator $\mathcal{L}$ is assumed to be two-local and can therefore be written as a sum of superoperators which act on nearest neighbours of the square lattice. In particular, $\mathcal{L}$ can be decomposed as

$$\mathcal{L} = \sum_{\langle\alpha,\beta\rangle} \mathcal{L}_{\alpha,\beta} = \sum_{\langle\alpha,\beta\rangle} \mathcal{H}_{\alpha,\beta} + \mathcal{D}_{\alpha,\beta}. \tag{4.2}$$

where the labels α and β correspond to the coordinates of the lattice site j and l respectively. Specialising to the case of a superoperator in Lindblad form, $\mathcal{L}_{\alpha\beta}$ can be further decomposed into the coherent part governed by the Hamiltonian H and the dissipative part, which is governed by the set of Lindblad operators L. The Hamiltonian part of the evolution is included in the superoperator $\mathcal{H}$ and the dissipative part in the superoperator $\mathcal{D}$. If the convention for matrix vectorisation is to stack the matrix column-by-column, then, these are are constructed as shown in equations 4.3 and 4.4 respectively:

$$\mathcal{H}_{\alpha,\beta} = -i\left(\mathbb{I}_{\alpha,\beta} \otimes H_{\alpha,\beta} - H^T_{\alpha,\beta} \otimes \mathbb{I}_{\alpha,\beta}\right), \tag{4.3}$$

$$\mathcal{D}_{\alpha,\beta} = \frac{1}{2}(2L^*_{\alpha,\beta} \otimes L_{\alpha,\beta} - I_{\alpha,\beta} \otimes L^\dagger L_{\alpha,\beta} - L^T L^*_{\alpha,\beta} \otimes I_{\alpha,\beta}). \tag{4.4}$$

The vectorised operators in the exponent are then split into those acting on even and odd pairs of lattice sites along both the x and y lattice dimensions. This gives four sets of vectorised operators $\mathcal{L}^e_x$, $\mathcal{L}^o_x$, $\mathcal{L}^e_y$ and $\mathcal{L}^o_y$ which are defined in terms of $\mathcal{L}_{\alpha\beta}$ as

$$\mathcal{L}^e_r = \sum \mathcal{L}_{2r,2r+1}, \quad \mathcal{L}^o_r = \sum \mathcal{L}_{2r-1,2r}. \tag{4.5}$$

As is common in algorithms based on TEBD, the full time evolution $e^{t\mathcal{L}}$ is decomposed into a set of layers via a Trotter decomposition with $\tau = t/n$ where $n \gg 1$ is the Trotter number. Each Trotter layer is given by

$$e^{\tau\mathcal{L}} = e^{\tau\mathcal{L}_x^e} e^{\tau\mathcal{L}_x^o} e^{\tau\mathcal{L}_y^e} e^{\tau\mathcal{L}_y^o} + \mathcal{O}(\tau^2). \tag{4.6}$$

where each of the four dynamical maps in the decomposition is applied to pairs of nearest neighbour tensors A_j and A_l in turn.

Consider one of these dynamical maps $e^{\tau\tilde{\mathcal{L}}}$, a useful method to calculate its action on the pair of tensors A_jA_l is to use Krylov methods. To do this, the linear map $\tilde{\mathcal{L}}(A_jA_l)$ is defined, where the linear operator $\tilde{\mathcal{L}}_{j,l}^{j',l'}$ acts on the pair of tensors A_j and A_l such that A_jA_l behaves as a vector in the linear map as illustrated in Figure 4.10 (a). By repeated application of this map, an approximation to the tensor $e^{\tau\mathcal{L}}A_jA_l$ Figure 4.10 (b) is calculated using a Krylov subspace algorithm. This method eliminates the need for explicit exponentiation of $e^{\tau\mathcal{L}}$.

Truncation

To complete the update, the resulting tensor $e^{\tau\mathcal{L}}A_jA_l$ needs to be decomposed into a new pair of tensors A_j' and A_l' as illustrated in Figure 4.10 (b-d). This is typically achieved via a singular value decomposition (SVD), where in the general case, the new bond dimension D'—which is equal to the number of singular values associated with the SVD—will be enlarged such that $(D' > D)$. In principle one could keep all singular values, however, the complexity of the algorithm would very quickly increase after only a few time steps and the benefits of using the TN ansatz diminished. Therefore, the enlarged bonds need to be truncated in an appropriate way for the algorithm to remain efficient. The number of singular values to retain could be chosen by keeping singular values above some relative tolerance, in the present case however, we choose to truncate

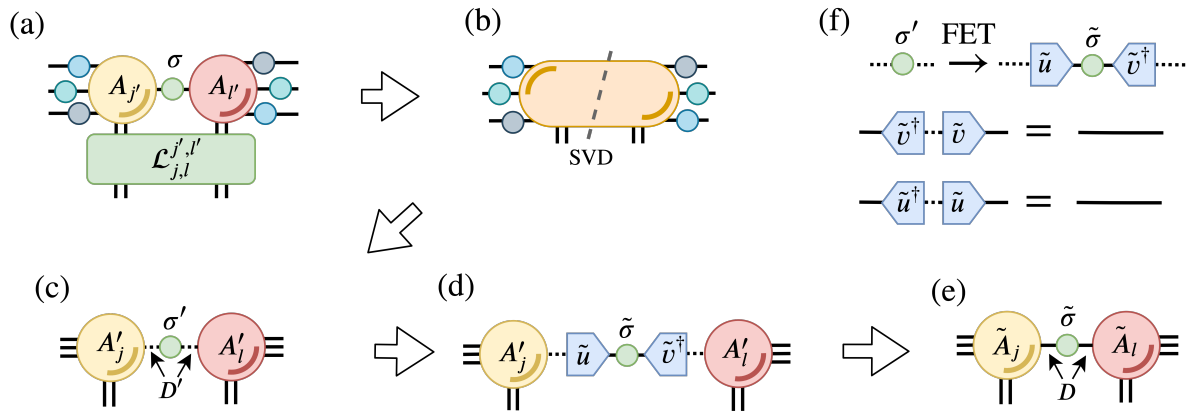

Figure 4.10: (a) Two site Trotter map $\mathcal{L}$ is applied to the nearest neighbour tensors A_j and A_l, repeated application of this map is used to find $\exp(\tau\mathcal{L})A_jA_l$using Krylov methods. (b) The resulting contracted tensor is decomposed using a SVD resulting in (c) A'_j , A'_l and a new $D' \times D'$ bond matrix σ' . (d-e) The enlarged bonds $D'$are truncated back to their original dimension D via the isometries $\tilde{u}$ and $\tilde{v}$. The isometries giving an optimal truncation with respect to the surrounding environment can be found using full environment truncation (FET).

D' back to its original size D after the action each dynamical map and subsequent decomposition.

For TNs without closed loops—also known as acyclic, TNs—finding the basis which results in the optimal truncation of singular values benefits greatly from the ability to efficiently apply a gauge transformation and transform the network to a canonical form, for example, for an MPS in mixed canonical form, the singular values have a clear correspondence to the Schmidt coefficients associated to the bipartition at the orthogonality centre. For TNs with closed loops—also called cyclic TNs—such a canonical form cannot be defined uniquely and finding the basis in which the truncating the enlarged bond is optimal is much less straightforward. Furthermore, cyclic TNs can host so called internal correlations, these correlations have no influence on the properties of the quantum state but may cause computational problems if they are allowed to accumulate, see for example the discussion in [56]. Given that the present case of a square lattice is clearly a cyclic TN, we must be careful about how the singular values are truncated.

We proceed in the usual way: after the contraction of the dynamical we decompose the tensors using SVD and truncate the bond irrespective of the state of the environment, leaving a new enlarged dimension $D' \geq D$ which is chosen such that only those singular values greater than some small relative tolerance $\epsilon_{D'} \ll 1$ are retained as in . We are left with a bond matrix σ with the remaining D' singular values along its diagonal and the tensors A_i and A_j as shown in Figure 4.10 (c). To perform the truncation, the bond matrix σ is replaced with the product $\tilde{u}\tilde{\sigma}\tilde{v}^\dagger$ where $\tilde{u}$ and $\tilde{v}$ are isometries of dimension (D', D) such that $\tilde{u}\tilde{u}^\dagger = \tilde{v}\tilde{v}^\dagger = I$ and the matrix $\tilde{\sigma}$ is a new D dimensional diagonal bond matrix. The enlarged bond is then truncated by contracting A_j and A_l with $\tilde{u}$ and $\tilde{v}$ as illustrated in Figure 4.10 (d). This truncation method shifts the problem to that of calculating an optimal $\tilde{u}$, $\tilde{v}$ and σ.

To calculate the set $\tilde{u}$, $\tilde{\sigma}$ and $\tilde{v}$ we adapt the Full Environment Truncation (FET) algorithm of [56]. FET prescribes a neat method to find an optimal truncation of an internal index of an arbitrary cyclic TN for closed systems. In [56], the truncation is optimised with respect to a fidelity measure for pure states. Here, we are dealing with an open quantum system for which a pure state fidelity measure no longer holds, we therefore optimise the truncation with respect to an objective function suitable for mixed states. More precisely, the goal of the optimisation routine is to maximise a mixed state fidelity measure between the state ρ for which the enlarged bond dimension is left untruncated and the state ϕ in which the same bond has been truncated by $\tilde{u}$, $\tilde{\sigma}$ and $\tilde{v}$. Assuming that a global maximum is found, this procedure will find the isometries which leave the state ϕ as close as possible to ρ with respect to the chosen fidelity measure.

To this end, we choose to maximise the fidelity $\mathcal{F}(\rho, \phi)$, which has the Hilbert-Schmidt inner product of ρ and ϕ in its numerator and the geometric mean of their

purities $tr(\rho^2)$ and $tr(\phi^2)$ in its denominator discussed in [180]

$$\mathcal{F}(\rho,\phi) = \frac{\mathrm{tr}(\rho\phi)}{\sqrt{\mathrm{tr}(\rho^2)\mathrm{tr}(\phi^2)}}. \tag{4.7}$$

If we note that squaring $\mathcal{F}$ is convex, then the ρ and ϕ which maximise $\mathcal{F}^2(\rho,\phi)$ also maximise $\mathcal{F}(\rho,\phi)$. In practice it is easier to construct $\mathcal{F}^2(\rho,\phi)\,\mathrm{tr}(\rho^2)$ as a Rayleigh quotient of tensors which can then be maximised to find an optimal $\tilde{u}$, $\tilde{\sigma}$ and $\tilde{v}$.

Full Environment Truncation

The FET algorithm adapted from [56] is used to truncate enlarge bonds of the iPEPO as follows.

1. Let the state of the full system—the unit cell plus its environment—at a time t be ρ_t .

2. Calculate the Hilbert-Schmidt effective environment $\mathcal{E}^{hs}$ of the iPEPO representing ρ_t.

3. Find A'_j and A'_l by applying the dynamical map to the pair of iPEPO tensors A_j and A_l before decomposing and retaining the D' singular values with a magnitude (relative to the largest singular value) greater than $\epsilon_{D'}$.

4. Contract A'_j and A'_l with the effective environment $\mathcal{E}^{hs}$ leaving only the enlarged bonds uncontracted as illustrated in Figure 4.10 (b). This leaves us with the fourth-rank bond environment tensor Υ_{jl}.

5. Use the bond environment Υ_{ij} to calculate the tensors $\mathrm{tr}(\rho\phi)$, $\mathrm{tr}(\phi\phi)$ and $\mathrm{tr}(\rho\rho)$ which depend on the isometries u and v, the bond matrix σ and the bond environment Υ_{ij} as illustrated in Figure 4.10 (c-e)

6. Use $\mathrm{tr}\,(\rho\phi)$, $\mathrm{tr}\,(\phi\phi)$ and $\mathrm{tr}\,(\rho\rho)$ to construct the Rayleigh quotient proportional to $\mathcal{F}^2$, illustrated graphically in Figure 4.12, where we note that the term $\mathrm{tr}\,(\rho\rho)$ is independent of u, σ and v.

7. The alternating optimisation of u, v and σ then proceeds as follows, see Figure 4.12.

8. Define $R \equiv \sigma v$. Find the R_m which maximises $\mathcal{F}^2\,(\rho, \phi)\,\mathrm{tr}\,(\rho^2)$ by first keeping v fixed and solving the resulting generalised eigenvalue problem in R.

9. Calculate the updated tensors σ' and u' using a SVD.

10. Defining $L \equiv v'\sigma'$. Find the optimal L_m by solving the generalised eigenvalue problem in L

11. Use a SVD to find u'', σ'' and v''.

12. The alternating procedure of steps 9-12 is repeated n times, until the trace distances $1/2||u^{(n)} - u^{(n-1)}||_1$ and $1/2||v^{(n)} - v^{(n-1)}||_1$ are both below a small tolerance . Supposing that a global minimum is reached, this gives the optimal set $\tilde{u}$, $\tilde{\sigma}$ and $\tilde{v}$.

Rayleigh Quotient

A Rayleigh quotient $F(R)$ in terms of the matrices R, A, and B

$$F(R) = \frac{\vec{R}^\dagger A \vec{R}}{\vec{R}^\dagger B \vec{R}} \tag{4.8}$$

is maximised by the eigenvector $\vec{R}_m$, which corresponds to the largest eigenvalue λ_m of the generalised eigenvalue problem $A\vec{R}_i = \lambda_i B\vec{R}_i$. Given that in the above case, the matrix A is constructed as an outer product $A = \vec{P}^\dagger \vec{P}$ of vectors $\vec{P}$, then the $\vec{R_m}$ which

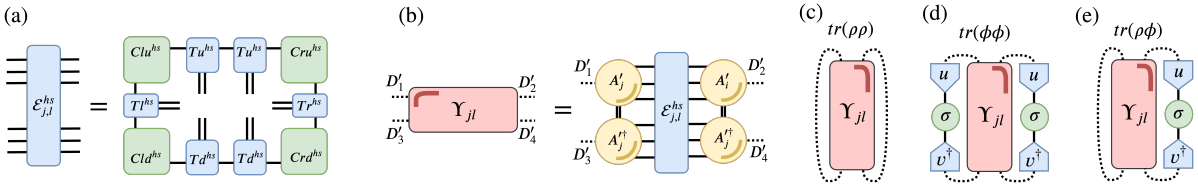

Figure 4.11: The environment of the unit cell. (a) The trace effective environment $\mathcal{E}_j^{tr}$ of the iPEPO tensor A_j used to calculate the $d \times d$ reduced density matrix ρ_j. (b) The Hilbert-Schmidt effective environment $\mathcal{E}_j^{hs}$ of the tensor a_j^{hs} used in constructing the bond environment. (c) The effective environment $\mathcal{E}_{j,l}^{hs}$ of the tensors at neighbouring sites j and l. (d) The bond environment $\Upsilon_{j,l}$ is the contraction of $\mathcal{E}_{j,l}^{hs}$ and the updated tensors A'_j and A'_l with enlarged bonds $\{D'_j\} \geq D$. (e-g) Using $\Upsilon_{j,l}$ the terms in the fidelity between the truncated (ϕ) and untruncated (ρ) density matrices are calculated by contracting with the isometries u, v and the bond matrix σ.

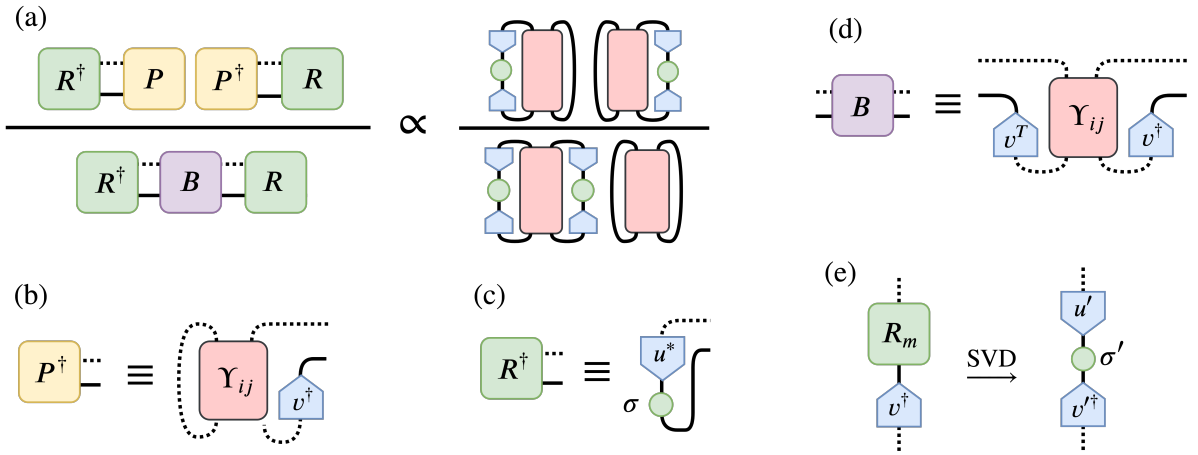

Figure 4.12: Tensor diagrams representing some of the steps involved in finding the isometries $\tilde{u}$ and $\tilde{v}$ and the bond matrix $\tilde{\sigma}$ which maximise the fidelity between the truncated and untruncated bonds. (a) The Rayleigh quotient in R is proportional to $\mathcal{F}^2$. (b) P is the contraction of the bond environment $\epsilon_{j,l}$ and the isometry v. (c) R is the contraction of the bond matrix σ and the isometry u. (d) B is the contraction of Υ_{jl} with the isometry v. (e) The new (primed) isometries are found by singular value decomposition of the contraction of the maximal eigenvector R_m and v.

maximises the Rayleigh quotient is also given directly by $\vec{R_m} = \vec{P}B^{-1}$. In practice there are a number of ways to find the maximum eigenvector. Firstly it is possible to calculate $\vec{R_m}$ directly by inverting B using a matrix inversion function. Secondly, $\vec{R_m}$ can be found by solving the system of linear equations $\vec{R_m}B = \vec{P}$ using, for example, a linear regression algorithm. Lastly, one can solve the generalised eigenvalue problem $A\vec{R} = \lambda B\vec{R}$ using an eigenvalue solver via full diagonalisation of an iterative solver. Care must be taken at this stage to maintain the stability of the algorithm. If solving by direct inversion, it useful to either use a Moore-Penrose pseudoinverse [138] or to solve via linear regression with an intermediate truncated singular value decomposition. All of the above methods give acceptable results. Note also that it is useful for the stability of this stage of the algorithm to symmetrise the bond environment such that $\Upsilon_{jl} = 1/2(\Upsilon^{\dagger}_{jl} + \Upsilon_{jl})$ and furthermore it is favourable to use the so called positive approximant of Υ_{jl} in which any small negative eigenvalues are set zero.

Simple Update

The Simple Update (SU) method can be thought of as discarding the effect of the environment on local dynamics by truncating enlarged bonds in a simplified way and also bypassing the gauge fixing step. Instead of keeping relative singular values above a small tolerance $\epsilon_{D'}$ in step 3 above (Figure 4.10 (c)), the tensors A'_j and A'_l are immediately truncated back to their original dimension D. This is equivalent to choosing both $\tilde{u} \rightarrow \tilde{u}_{su}$ and $\tilde{v} \rightarrow \tilde{v}_{su}$ as $D' \times D$ matrices with all diagonal entries equal to one and all other entries equal to zero and retaining only the D largest singular values of σ' in the truncated $\tilde{\sigma}_{su}$. In general, we observe that the set of $\tilde{u}$, $\tilde{v}$ and $\tilde{\sigma}$ found using FET are inequivalent to $\tilde{u}_{su}$, $\tilde{v}_{su}$ and $\tilde{\sigma}_{su}$. This suggests that, in the general case, SU does not yield a truncation which is optimal with respect to the objective function we use.

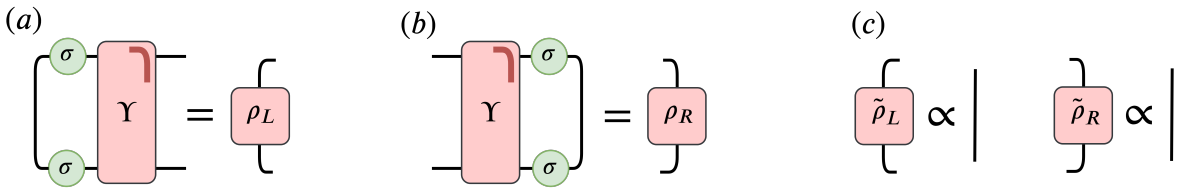

Figure 4.13: (a) The left boundary matrix ρ_L is constructed by left contraction of the bond environment with the bond matrices. (b) The right boundary matrix ρ_R is calculated by right contraction of the bond matrices. (c) The Weighted Trace Gauge is that for which the environment matrices $\tilde{\rho}_L$and $\tilde{\rho}_R$ are proportional to the identity matrix. Figure adapted from [56]

Gauge Fixing

There exists a gauge freedom across the internal bond in the network. This can be seen by inserting a resolution of the identity across across any internal bond $\mathbb{I} = xx^{-1}$, the gauge freedom arises from the freedom in choosing the isometry x. For the iPEPO algorithm, fixing the gauge plays two important roles, firstly, it fixes the basis in which the enlarged bonds are truncated making this basis consistent across all truncations secondly it allows for the recycling of the environments $\mathcal{E}^{hs}$ and $\mathcal{E}^{tr}$ calculated for use at each FET step of the algorithm as an initial guess for the CTMRG renormalisation procedure which precedes the following FET step. Recycling the effective environments in this way reduces the number of renormalisation iterations required at each time step which can significantly reducing the total runtime of the algorithm.

Following [56], the gauge is fixed to so called Weighted Trace Gauge by demanding that the so called left and right boundary matrices demonstrated graphically in Figure 4.13 are proportional to the identity matrix. A method for fixing an internal index to the WTG is given in [56] and requires only the bond environment and bond matrix as input making the procedure easy to generalise to arbitrary networks so long as the bond environment can be calculated efficiently. For a bond in WTG, the associated diagonal bond matrix contains the Weighted Trace Gauge Coefficients which reduce the Schmidt coefficients in the case where the network is acyclic or there are no internal correlations

across the bond.

Quantifying Internal Correlations

A convenient method of quantifying the extend of internal correlations was introduced in [56]. The so called cycle entropy across a bond in the cyclic TN joining sites i and j is defined in terms of the bond environment $\Upsilon_{i,j}$. The cycle entropy is defined as the von-Neumann entropy of the normalised spectrum of the bond environment left-contracted with the bond matrix. More precisely, defining $\bar{\Upsilon} \equiv (\sigma \otimes \sigma)\Upsilon$—similar to Figure 4.13 (a) without contracting over the left bonds—then the cycle entropy is given by $S_{\text{cycle}} = -\sum_\alpha \bar{\lambda}_\alpha \log_2 \bar{\lambda}_\alpha$ where the $\bar{\lambda}_\alpha$ are the normalised eigenvalues of $\bar{\Upsilon}$. If the cycle entropy is zero then no internal correlations are present across the bond, furthermore, if the gauge is fixed to WTG then the associated coefficients are equal to the Schmidt coefficients.

4.5 Measurement

Measurement of local observables is done by first constructing local reduced density matrices. For example, Figure 4.14 shows graphically, the tensor contractions required to calculate (a) the local density matrix ρ_j, (b) the nearest neighbour density matrix ρ_{jk} and (c) a longer range density matrix where intermediate spins are traced out ρ_{jm}. There is a unique single site reduced density matrix for each site in the unit cell. They are constructed by contracting the iPEPO tensors at each site A_j with its its trace effective environment $\mathcal{E}^{\text{tr}}$. Similarly, there is a unique two-site nearest neighbour tensors between each pair of unique lattice sites in the unit cell, constructed by contracting the pair of iPEPO unit cell tensors A_j and A_k with their trace effective environment $\mathcal{E}^{\text{tr}}_{jk}$. When calculating longer range correlations, say between a site j and some distant site m, rather than constructing the full density matrix, it is useful to trace out intermediate as

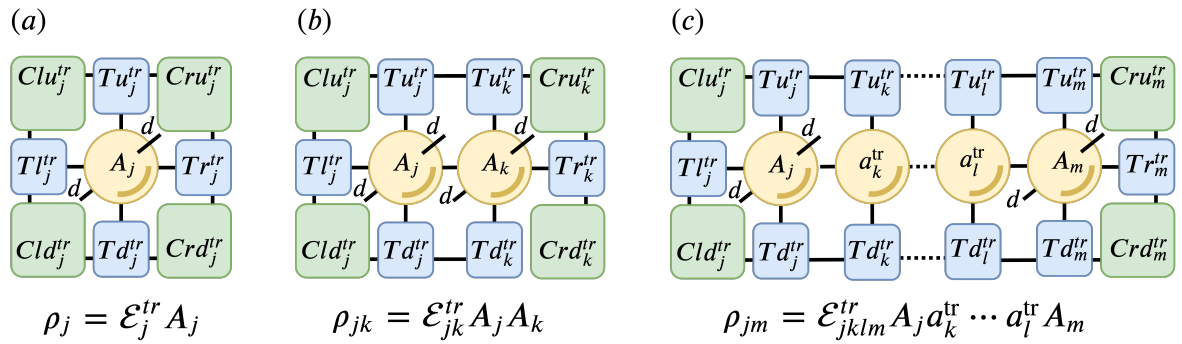

Figure 4.14: Calculation of the reduced density matrices via contraction of the trace effective environment $\mathcal{E}^{\mathrm{tr}}$with the iPEPO tensors A_j. Correlations between distant sites can be calculated efficiently by sandwiching a^{tr}between measurement sites as shown.

shown in Figure 4.14 (c). During the runtime of the algorithm, all tensors are normalised by their component with maximum absolute value, it is therefore usually necessary to normalise all density matrices calculated as shown in Figure 4.14 by dividing by their trace, i.e. $\rho \Leftarrow \rho/\mathrm{tr}\rho$.

In principle, once the iPEPO representation is obtained one can construct arbitrarily large two-dimensional reduced density matrices, however the size is limited by the complexity of contracting the associated TN. For the full infinite system, we do not have access to the full eigenspectrum and deciding whether or not the full system represents a physical state is a difficult problem. For reduced density matrices of a small to moderate size, the full eigenspectra can be calculated exactly and the positivity of their eigenvalues checked explicitly—this is an import check to perform after constructing the density matrices. We have found that in the majority of cases there are no negative eigenvalues for small reduced density matrices on the order of a few lattice sites. If any negative eigenvalues do appear, then they tend to be found for the multisite density matrices and often disappear as the bond dimension is increased. While the possibility of having negative eigenvalues in the reduced density matrices is a potential drawback of the method, we find that for most of the use cases we are interested in, significant problems do not arise.

4.6 A Dissipative Transverse Ising Model

As a first benchmark of the algorithm we calculate the dynamics of a dissipative transverse quantum Ising model with Hamiltonian

$$H_{TI} = \frac{V}{z} \sum_{\langle j,l \rangle} \sigma_j^z \sigma_l^z + \sum_j \frac{h_x}{2} \sigma_j^x, \tag{4.9}$$

where V is the rate of hopping between sites, h_x is the strength of a transverse field and z is the coordination number of the lattice. The spins undergo dissipation at a rate γ which is described by the local Lindblad jump operators $L_j = \sqrt{\gamma}\frac{1}{2}\left(\sigma_j^y - i\sigma_j^z\right)$, which are equivalent at each lattice site. We refer to the resulting Liouvillian as $\mathcal{L}[H_{TI}, L_j]$. The purely dissipative dynamics $\mathcal{D}\left(\rho_{dis}\right) = 0$ drive the system towards a steady state $\rho_{dis} = \bigotimes |{\downarrow_x}\rangle\langle{\downarrow_x}|$ which does not commute with the Hamiltonian H_{TI} , therefore, the ordered phases of the Hamiltonian can be frustrated by the dissipation.

Efficiently Solvable Model

To facilitate a quantitative test of accuracy for the FET+WTG method it is useful to compare to an exactly solvable model. In two-dimensional open quantum lattice models exacly solvable systems are difficult to find. However the work of [64] identifies a family of models which are efficiently solvable under certain conditions. In the case of zero transverse field $h^x/\gamma = 0$, the Liouvillian $\mathcal{L}[H_{TI}, L_j]$ belongs to the family of efficiently solvable dissipative models described in [64]. In particular, the Liouvillian has a structure such that coherences are not mapped to populations (and vice versa) therefore as shown in [64] correlations remain localised. If some local observables of interest initially have support on a suitably small sublattice, then, the numerically exact time evolution of those observables can be calculated efficiently.

An observable $O(t)$, which initially has support on a set of lattice sites $\mathcal{A}$, can be

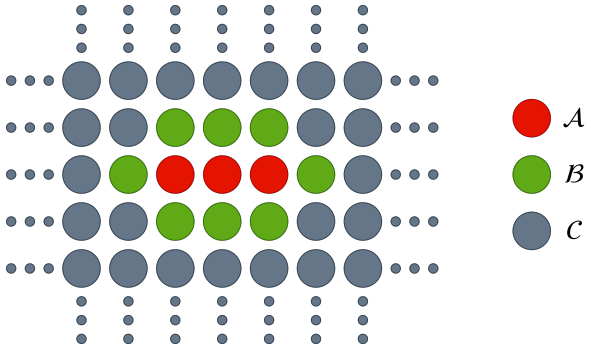

Figure 4.15: An efficient solution can be obtained if the initial state has support on a small subset of spins $\mathcal{A}$ and one can numerically calculate the solution of the subset $\mathcal{A} \cup \mathcal{B}$. Here we choose A as a set of three contiguous spins in the lattice and since the Liouvillian is two-local, we identify $\mathcal{B}$ as the set of eight lattice sites which are nearest neighbours of $\mathcal{A}$. The set $\mathcal{A} \cup \mathcal{B} \cup \mathcal{C}$ represents the full system.

calculated to all times by solving, in the Schrödinger picture:

$$\langle O \rangle(t) = \mathrm{Tr}_{\mathcal{A}\cup\mathcal{B}} \left[O \exp\left(t\mathcal{L}_{\mathcal{A}\mathcal{B}}\right) \rho_{\mathcal{A}\mathcal{B}} \right], \tag{4.10}$$

where where the sublattice $\mathcal{B}$ is the set of lattice sites which are nearest neighbours of the sublattice $\mathcal{A}$ and for which the Hamiltonian has simultaneous support on both $\mathcal{A}$ and $\mathcal{B}$. To test the accuracy of local observables up to next-nearest neighbour (along a lattice row or column) correlations $S^{xx}_{jl}(t)$ in time, we choose as $\mathcal{A}$ the set of three contiguous lattice sites in a row in either the x or y lattice dimension. For the two-local Liouvillian $\mathcal{L}[H_{TI}, L_j]$, the sublattice $\mathcal{B}$ is identified as the eight nearest-neighbour lattice sites of $\mathcal{A}$, shown in Figure 4.15. Starting from an initial product state, the observables $O(t)$ are calculated efficiently by solving equation 4.10 using standard techniques from quantum optics; we use the Julia package QuantumOptics.jl [98] . Results calculated using this method are labelled $EXACT$.

Method

The system is initialised in the product state of spins $\rho_0 = \bigotimes|\uparrow_z\rangle\langle\uparrow_z|$ and the evolution in time is calculated at four different pairs of the parameters $(V/\gamma, h^x/\gamma)$. These are in a strongly dissipative regime with $V/\gamma = 0.2$, $h^x/\gamma = 0$, a moderately dissipative regime with $V/\gamma = 1.2$, $h^x/\gamma = 1.0$ and a weakly dissipative regime where the hopping term is larger $V/\gamma = 4.0$, $h^x/\gamma = 0$, the fourth pair of parameters $V/\gamma = 0.5$, $h^x/\gamma = 1.0$ model a regime which has a nonzero transverse field and no longer admits an efficient solution via the method of [64].

For all results pertaining to this transverse Ising model the parameters of the FET+WTG method are chosen as: $\epsilon_{D'} = 10^{-8}$, $\epsilon_\chi = 10^{-10}$, $\epsilon_{FET} = 10^{-10}$, $\epsilon_{svd} = 10^{-10}$. The time step is set to $\tau\gamma = 0.01$ in all instances cases except for the calculation of the weakly dissipative regime where a value of $\tau\gamma = 0.005$ is chosen.

In each regime, the reduced density matrices ρ_j and ρ_l for each lattice site—labelled j and l—in the two-site unit cell as well as the set of four nearest neighbour reduced density matrices ρ_{jl} across each unique bond in the unit cell as well as the four next nearest neighbour reduced density matrices $\rho_{jj'}$ where j and j' are at a distance of two lattice constants rather than $\sqrt{2}$, the sites j and j' are in the same row or column. Although it is found that all of the reduced density matrices within each set are equivalent to a high precision, it is convenient to plot expectation values averaged over each set. More precisely, the average magnetisation is given by $m^x = \frac{1}{2}\left(\mathrm{tr}\left(\sigma^x\rho_j\right) + \mathrm{tr}\left(\sigma^x\rho_l\right)\right)$, the average purity of the single site reduced density matrices by $\Pi_1 = \frac{1}{2}\left(\mathrm{tr}\left(\rho_j^2\right) + \mathrm{tr}\left(\rho_l^2\right)\right)$. The non-local reduced density matrices are used to calculate S^{xx}_{12} and S^{xx}_{13}, where $S^{xx}_{jl}(t) = \mathrm{tr}(\sigma^x_j \otimes \sigma^x_l \rho^t)$, where once again, these are averaged over the four possible choices for j and l in each case. Lastly, the infidelity of truncation $\mathcal{I}(t) = 1 - \mathcal{F}(t)$ averaged over the four trotter layers which make up every time step τ is calculated, here $\mathcal{F}$ is the mixed state fidelity given in equation 4.7. The results are given for a range of bond dimensions

D and choose $\chi^{tr} = \chi^{hs} = \chi$ in each case where we have confirmed the convergence of the results with respect to increasing χ^{tr} and χ^{hs} in all results shown.

Strong Dissipation

In Figure 4.16 the results pertaining to the strongly dissipative regime are plotted. The EXACT behaviour of the calculated observables can be summarised as follows. Starting from an initial product state, as time progresses, the average magnetisation $m^x(t)$ varies monotonically towards a stationary state reflecting the strong spin damping. Each spin is initially a pure product state with $\Pi_1 = 1.0$ which becomes mixed during the time evolution and tends towards $\Pi_1 \approx 0.88$ after the transient evolution. Initially uncorrelated, the spin-spin correlations S^{xx}_{12} and S^{xx}_{13} become non-zero and remain finite after the short transient phase.

Comparing the results of the EXACT method with the FET+WTG solution, excellent convergence is achieved for bond dimensions $D = 4$ and $D = 5$. The results for $D = 2$ and $D = 3$ lie somewhere between the $D = 1$ MF solution and the EXACT solution. The $D = 1$ solution tends towards an uncorrelated product state of spins in the $|{\downarrow^x}\rangle$ phase which reflects the dominance of the dissipative processes in the solution of the MF theory. Increasing the bond dimension to $D = 2$ and $D = 3$ it is found that S^{xx}_{12} and S^{xx}_{13} become non-zero and for $D = 3$ the solution tracks the EXACT dynamics closely at early times ($t\gamma \lessapprox 1$), however, after the transient stage the spins again tend towards an almost pure steady state in the $|{\downarrow^x}\rangle$ phase, similar to the MF solution. By increasing the bond dimension to $D = 4$ and $D = 5$ it is found that the FET+WTG method reproduces the EXACT dynamics to and excellent precision for all observables calculated.

In the bottom right panel of Figure 4.16, the infidelity of truncation as a function of time $\mathcal{I}(t)$ is plotted and its behaviour is similar for all values of D. A the dynamics

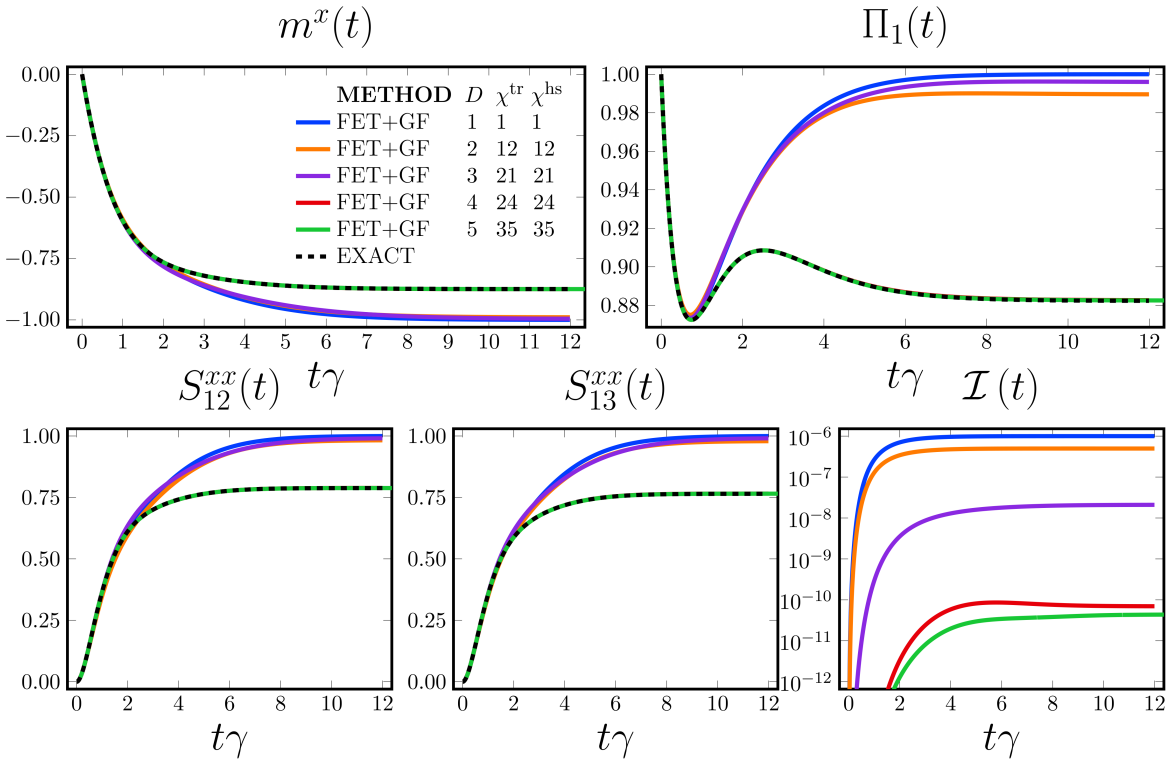

Figure 4.16: Strong damping regime of the dissipative transverse Ising model with parameters: $V/\gamma = 0.2$, $h^x/\gamma = 0$. The $D = 1$ results show that the MF theory give incorrect results. For bond dimensions $D \in [2, 3]$ the results fall somewhere between the EXACT and MF results while for $D \in [4, 5]$ the FET+WTG algorithm reproduces the EXACT dynamics to excellent precision.

progress from the initial product state and the correlations begin to deviate from zero, $\mathcal{I}(t)$ increases from $\mathcal{I} \ll 1$ where the error which is introduced by truncation of enlarged bonds is negligible, to a nonzero value indicating that the truncation causes the state to deviate from the case in which bonds are left untruncated. Nevertheless, for bond dimensions of $D = 4$ and $D = 5$, $\mathcal{I}(t)$ remains below $\approx 10^{-10}$ throughout the dynamics. This indicator of the accuracy of the results. Note that $\mathcal{I}(t)$ has a dependence on the time step τ—a smaller time steps will tend to induce smaller correlations per step that a large one.

Moderate and Weak Dissipation

Displayed in Figure 4.17 are the results in the moderate damping regime with model parameters $V/\gamma = 1.2$, $h^x/\gamma = 1.0$. In this case, the hopping strength is comparable to the rate of dissipation and therefore the EXACT dynamics of local observables display some transient oscillations which are quickly damped by the dissipation. The EXCAT solution again contrasts significantly to the $D = 1$ solution where the system tends towards a pure steady state with all spins in the $|\downarrow^x\rangle$ state. The FET+WTG method reproduces the EXACT dynamics to good precision for the single site observables for $D > 3$. For the non-local observables, S^{xx}_{12} and S^{xx}_{13} also show good agreement with EXACT particularly for $D = 7$.

The case of weak dissipation $V/\gamma = 4.0$ and $h^x/\gamma = 0.0$ is plotted in Figure **??**. In the EXACT results, weakly damped oscillations at early times reflect the dominance of the hopping term. The $D = 1$ solution clearly gives incorrect results, while the results for $D \in [5, 6]$ reproduce the EXACT solution at early times but begin to deviate after approximately $t\gamma = 2 - 3$, although still retaining similar qualitative behaviour. The $D = 7$ results again reproduce the EXACT results at early times but start to deviate significantly at later times. That larger bond dimension are required to reproduce the exact results for early times is indicative of the greater role played by correlations in this coherent hopping dominated regime.

Beyond Efficiently Solvable Regime

For nonzero transverse field h^x, the Liouvillian does not fulfil the conditions for an efficient solution using the EXACT method. Of course, the FET+WTG method makes no assumption as to extent of correlations and should therefore be applicable for these parameters. As an example, the case of $V/\gamma = 0.5$ and $h^x/\gamma = 1.0$ is presented in Figure **??**. Using FET+WTG, the values of local observables as a function of time are

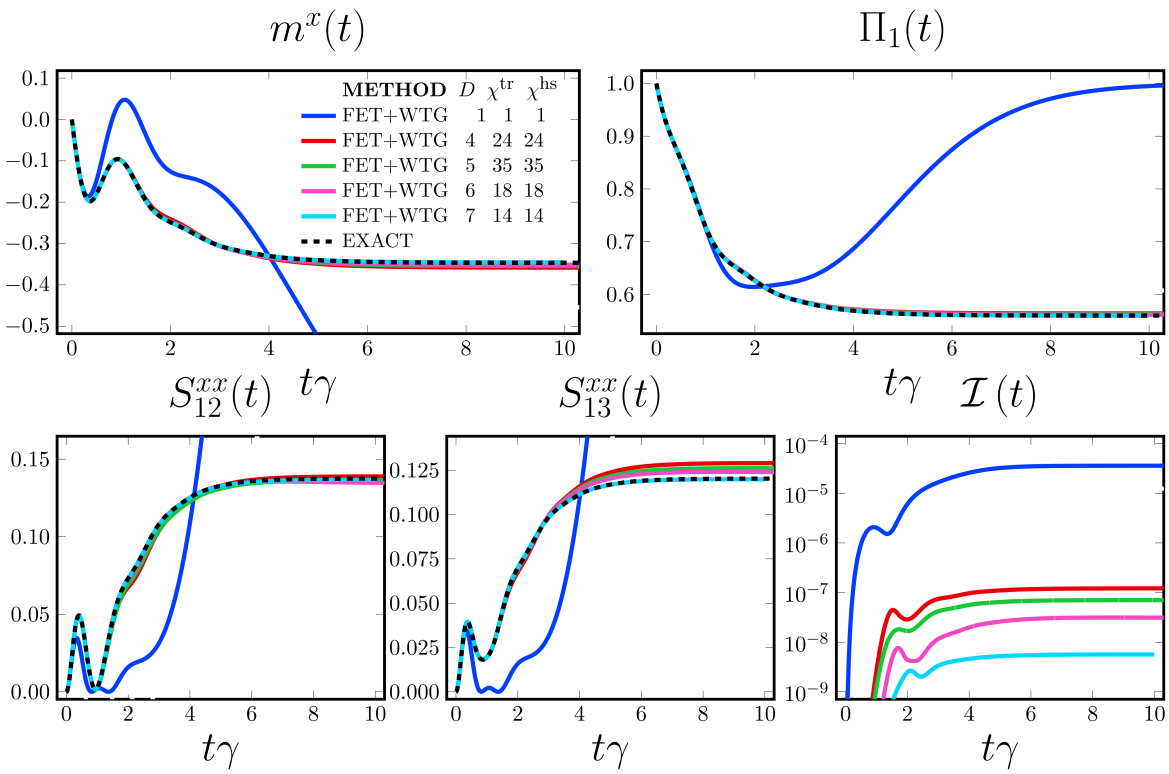

Figure 4.17: Moderate damping regime of the dissipative transverse Ising model with parameters: $V/\gamma = 1.2$, $h^x/\gamma = 0$. The MF $D = 1$ results are qualitatively incorrect while the EXACT results are well approximated using the FET+WTG method for $D \in [6, 7]$.

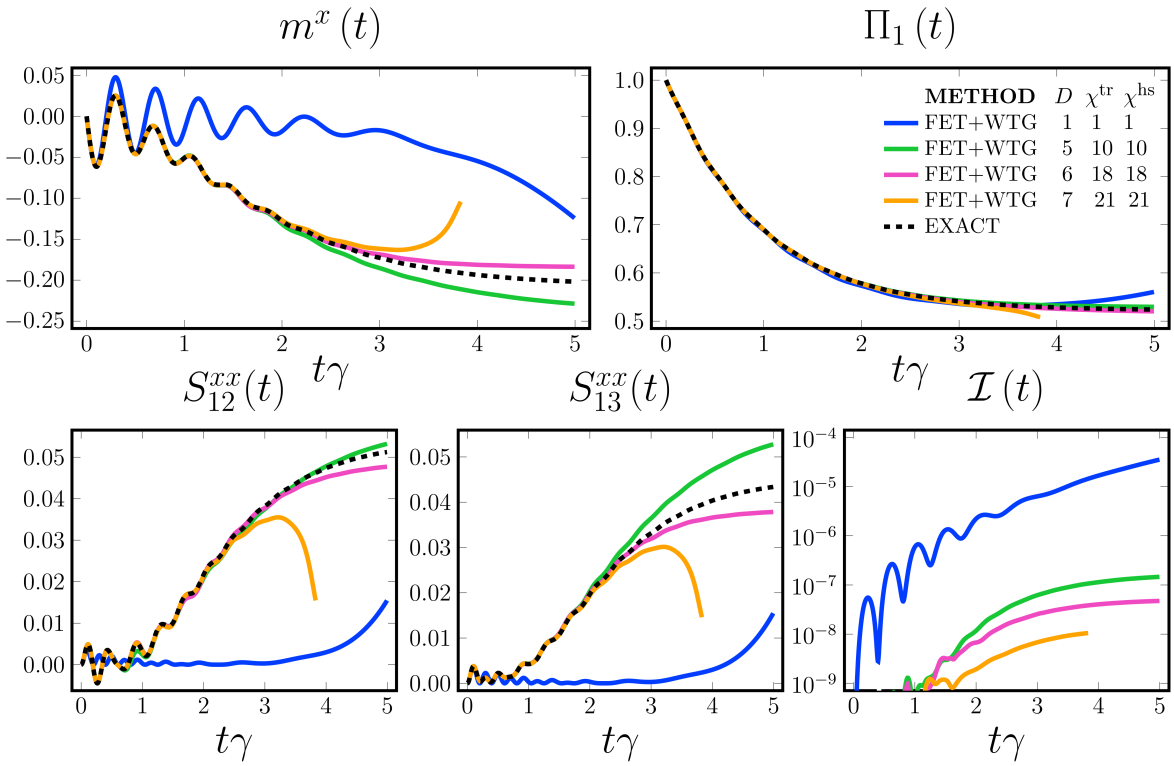

Figure 4.18: Weak damping regime of the dissipative transverse Ising model with parameters: $V/\gamma = 4.0$, $h^x/\gamma = 0$. The EXACT results are well approximated at early times using a bond dimension $D \in [5, 6, 7]$ however they begin to deviate after $t\gamma \sim 2 - 3$ which suggests that the system quickly becomes correlated. The large deviation seen for $D = 7$ is due to numerical instability.

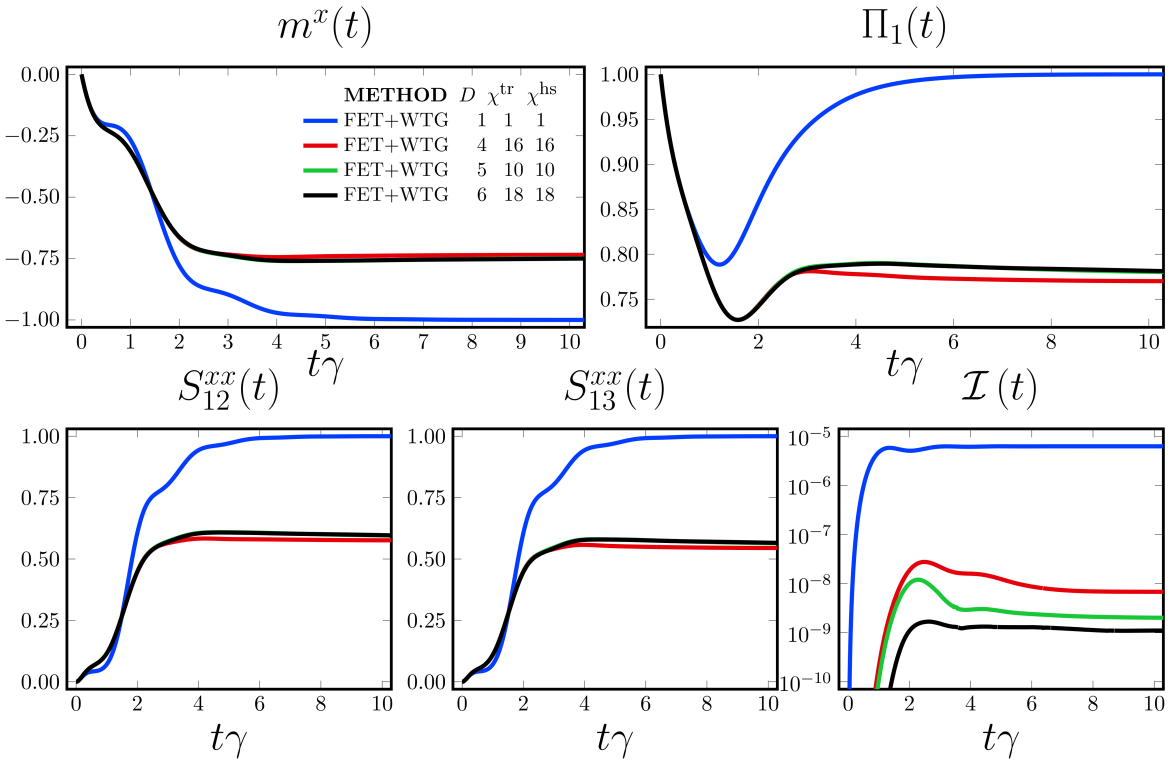

Figure 4.19: Beyond efficiently solvable regime of the dissipative transverse Ising model with parameters: $V/\gamma = 0.5$, $h^x/\gamma = 1.0$. For bond dimensions $D \in [5, 6]$ the dynamics appear well converged. In this case there is no EXACT with which to compare, however the behaviour is broadly similar the efficiently solvable cases with strong and moderate dissipation.

found to converge as the iPEPO bond dimension is increased. Results for $D \in [1, 4, 5, 6]$ converge well for $D \geq 5$. Considering the converged results, the behaviour of the system remains similar to the efficiently solvable cases: after after transient phase with damped oscillations, the initial pure product state tends towards a correlated mixed state, the converge results are qualitatively different from the $D = 1$ mean field solution. The infidelity of truncation remains well below $\mathcal{I}(t) < 10^{-8}$ for the converged results, a value which is consistent with the other benchmarking results.

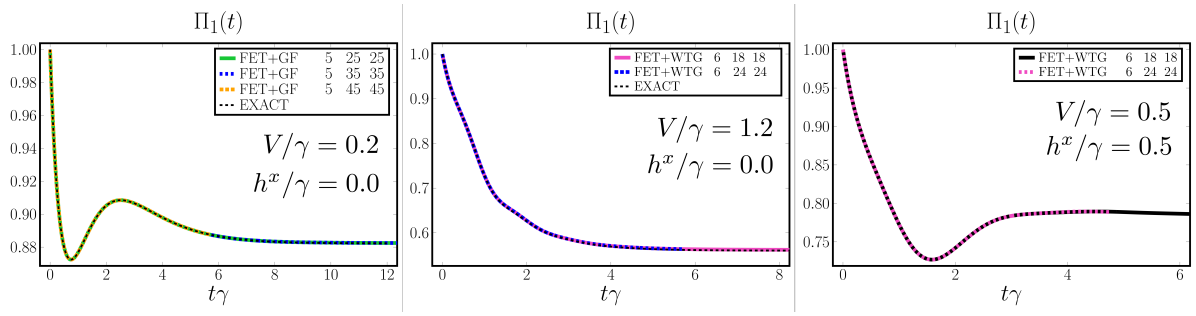

Figure 4.20: Convergence with respect to χ^{hs} in (a) the strongly damped (b) weakly damped and (c) outside the efficiently solvable regime. In each case there is no significant change upon increase of χ^{hs} suggesting that the Hilbert-Schmidt effective environment is well approximated.

Convergence with Respect to Environment

In Figure 4.20 the results for the averaged purity $\Pi_1(t)$ as a function of time of the one-site reduced density matrices are plotted for the three regimes which show good convergence: the strongly damped, moderately damped and beyond the efficiently solvable regime. In each case, results calculated for a bond dimension for which Π_1 appears well converged is plotted for a number of values of the environment bond dimensions $\chi^{\text{hs}} = \chi^{\text{tr}} = \chi$. In all cases, the purity shows almost no dependence on χ, confirming that the results are well converged with respect to χ. This is not surprising in the cases which admit an efficient solution using the EXACT method since we know a priori that the length scale of correlations remains small. It is likely that convergence with respect to χ^{hs} will be more important when correlations are longer ranged.

4.7 Comparison with Simple Update

In this section we compare and contrast the FET+WTG algorithm with the Simple Update (SU) algorithm. To do so, we focus on the moderate damping regime of the transverse Ising model discussed in the previous section. Using each method the dynamics in time of local observables are calculated for the parameters $V/\gamma = 1.2$ and $h^x/\gamma = 0$ for a

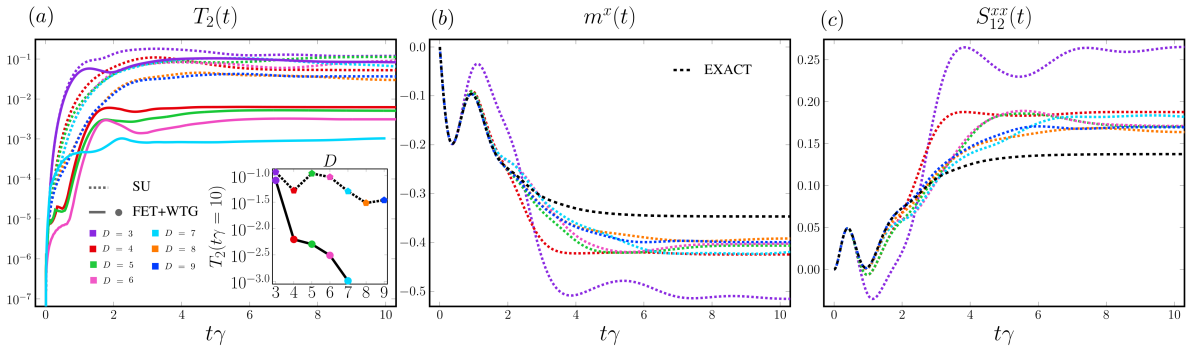

Figure 4.21: Comparison between FET+WTG and SU. (a) Trace distance between the EXACT two-site density matrices an those calculated using each method, SU and FET+WTG. inset: Trace distance at $t\gamma = 10$ clearly showing the scaling of the accuracy of results as the bond dimension is increased. (b) Magnetization $m^x(t)$ calculated using the SU method as compared to the EXACT results. (c) Nearest neighbour correlations $S^{xx}_{12}(t)$ calculated using the SU method and compared to the EXACT results.

range of bond dimensions. All parameters are the same for both methods; we use a time step of $\tau\gamma = 0.01$ and the parameters related to the CTMRG algorithm are $\epsilon_\chi = 10^{-10}$. For the FET+WTG algorithm we choose $\epsilon_{FET} = 10^{-8}$. The only difference between the results is in how $\tilde{u}$, $\tilde{v}$ and $\tilde{\sigma}$ are calculated and the SU method does not fix the gauge.

In Figure 4.21, the observables $m^x(t)$ and $S^{xx}_{12}(t)$ are compared directly with the results of EXACT, furthermore we provide a quantitative measure of the accuracy of each method by calculating the trace distance between the two-site reduced density matrices form the EXACT method at each time step and the corresponding reduced density matrix calculated using either the SU or FET+WTG methods. In particular, the trace distance $T_2(t)$ of the nearest neighbour reduced density matrices $T_2\left(\rho_{jl}, \phi_{jl}\right) = \frac{1}{2}\mathrm{tr}\left(\sqrt{(\rho_{jl} - \phi_{jl})^\dagger(\rho_{jl} - \phi_{jl})}\right)$ is calculated, where $T_2(t)$ is averaged over the four unique nearest neighbour reduced density matrices given by the two-site unit cell.

It is clear from Figure 4.21 (a-c) that the SU method does not reproduce the EXACT results to the same accuracy as FET+WTG. Figure 4.21 (a) and its inset demonstrate that FET+WTG undergoes a clear systematic improvement in accuracy as D is increased. On the other hand, SU shows only a minor improvement in $T_2(t\gamma = 10)$ which

is not systematic, even if D is increased well beyond that for which FET+WTG already demonstrates good convergence. For values of $D > 3$, T_2 is consistently approximately an order of magnitude smaller for FET+WTG than it is for SU, this illustrates the much improved compression and greater accuracy of WTG+FET. The observables in Figure 4.21 (b-c) calculated using SU tend to deviate from the EXACT dynamics considerably when compared to FET+WTG (compare to Figure 4.17), it is observed that at times $t\gamma \gtrapprox 2$, the SU method struggles to capture the EXACT results for all of the bond dimensions shown.

It is instructive to investigate how each algorithm deals with internal correlations in the network. The cycle-entropy S_{cycle} plotted in Figure 4.22 (a) and quantifies the extent of internal correlations as a function of time. Initially the network representing the product state, has no cycle entropy. In time however, S_{cycle} grows and saturates at a finite value. Importantly, S_{cycle} grows more slowly and saturates at a lower value if using FET+WTG than it does is using SU. This clearly illustrates that the more optimal truncation of bonds curtails the growth of internal correlations in the network. While the growth of S_{cycle} in the present case remains relatively benign throughout the time evolution, the failure of SU to curtail the accumulation of internal correlations may contribute to instabilities in the algorithm in some circumstances.

As a final comparison, the infidelity of truncation $\mathcal{I}$ as a function of time is plotted in Figure 4.22 for the two different methods. It is clear that FET+WTG outperforms SU; the infidelity between truncated an untruncated bonds is improved by approximately an order of magnitude. To summarise: the variational degree of the ansatz is equivalent in each case, they have same D and χ, however, the method by which the enlarged bonds are truncated is crucial in finding the optimal representation and reducing the accumulation of errors due to inadequate truncation and ultimately giving the most accurate results.

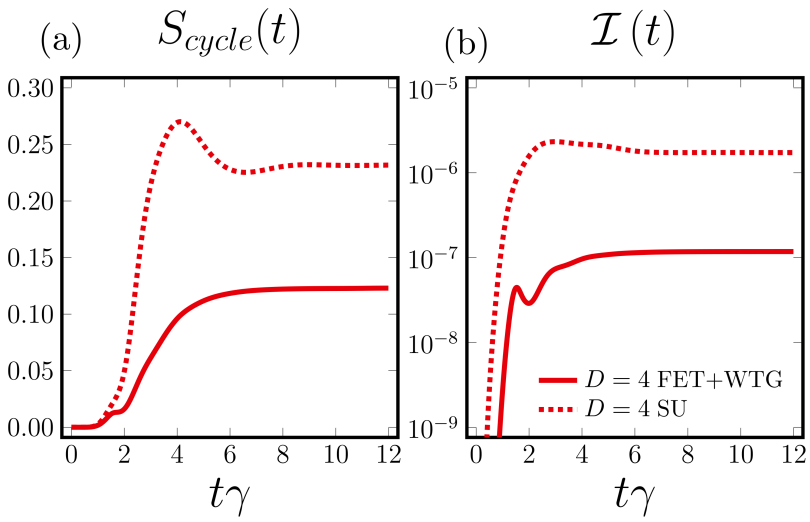

Figure 4.22: Comparison between the cycle entropy produced using the SU and FET+WTG methods during the time evolution in the moderately damped regime of the dissipative transverse Ising model for a bond dimension $D = 4$. The FET+WTG method curtails the growth of internal correlations producing a more efficient compression of the state.

4.8 Driven-Dissipative Hard-Core Bose Hubbard Model

An important class of open quantum system are those which are driven by an external source to counteract losses to the environment. For example, these systems are frequently encountered in quantum optics; a coherent or incoherent light source replenishes photons lost to the environment, see [30] for a review. Driven-dissipative systems are often well described by the Markovian approximation of the Lindblad master equation. In this section we test the FET+WTG method in this context by calculating steady state properties of a driven-dissipative hard core boson model. In this model, the on-site interactions between bosons hopping on the lattice are taken to infinity such that no two bosons can occupy the same lattice site. The model can therefore be mapped to a lattice of interacting spin-1/2 particles. In the reference frame rotating at the frequency of a coherent drive, the Hamiltonian is written as

Table 4.1: Expectation values in the steady state of a hard core boson model on an infinite square lattice. The model parameters are $\Delta/\gamma = 5.0$, $F/\gamma = 2.0$ and $J/\gamma = 1.0$ and are calculated using the iPEPO FET+WTG method. A time step of $\tau\gamma = 0.0025$ is used in all results. To facilitate a comparison, equivalent results for the same parameters calculated using the Corner-Space Renormalisation Method introduced in [60] for different sizes $N_x \times N_y$ are tabulated below.

$J/\gamma = 1.0 \quad F/\gamma = 2.0 \quad \Delta/\gamma = 5.0$

D	χ	$\epsilon_{D'}$	n	$\Re(\langle\sigma^-\rangle)$	$g^{(2)}_{\langle j,l\rangle}$
1	1	10^{-6}	0.09482	0.27619	1.0
3	9	10^{-4}	0.09545	0.27674	1.06243
	9	10^{-5}	0.09534	0.27680	1.06353
	9	10^{-6}	0.09534	0.27681	1.06360
	9	10^{-7}	0.09535	0.27680	1.06344
	15	10^{-7}	0.09535	0.27680	1.06344
4	8	10^{-7}	0.09548	0.27670	1.06440
	12	10^{-7}	0.09548	0.27670	1.06443
5	10	10^{-7}	0.09548	0.27670	1.06443
	15	10^{-7}	0.09548	0.27670	1.06443
$N_x \times N_y$	Corner Space Renormalization Method				
4×4			0.0954(1)	0.2764(2)	1.0643(3)
8×4			0.09527(2)	-	1.0436(3)
8×8			0.0948(2)	-	1.0237(6)

$$H = \sum_j [-\Delta\sigma_j^+\sigma_j^- + F(\sigma_j^+ + \sigma_j^-)] - \frac{J}{z}\sum_{\langle j,l\rangle}\sigma_j^+\sigma_l^-$$

where $\Delta = \omega_p - \omega_c$ is the detuning between the drive frequency ω_p and the on site energy ω_c of the cavity. The term F is the drive field strength, J is the rate of hopping between nearest neighbour lattice sites and the sum $\sum_{\langle j,l\rangle}$ runs over nearest neighbours in the lattice of coordination number z. The spins undergo local dissipation at a rate γ which is modelled by a local Lindblad jump operator $L_j = \sqrt{\gamma}\sigma_j^-$ which is the same at each lattice site. The operators $\sigma^\pm \equiv \frac{1}{2}(\sigma^x \pm i\sigma^y)$ are the spin raising and lowering operators.

A challenge which arises when trying to benchmark and test the accuracy of al-

gorithms for open quantum lattice models is that there are very few exactly or efficiently solvable models to compare to. Furthermore, there are only a handful of numerical techniques which are capable of simulating two-dimensional systems. In the following, we compare the steady state expectation values of the driven-dissipative hard-core Bose Hubbard model, calculated using the iPEPO method to those calculated using the Corner-Space Renormalisation Method (CSRM) first introduced in [60]. The CSRM simulates finite sized systems. In order to access lattices of increasing size it merges pairs of smaller lattices and retains only the most probable states, thereby restricting the system to a small subspace of the full Hilbert space. By systematically increasing the size of the finite system and hoping for convergence the results corresponding to large systems sizes are approached.

In order to facilitate a clear comparison, the steady of a square lattice hard core bosons with $\Delta/\gamma = 5$, $F/\gamma = 2$ and $J/\gamma = 1$ is simulated and the average single site density $n = 1/2(n_j + n_l)$ and nearest neighbour ($\langle j, l\rangle$) correlation functions $g^{(2)}$ are calculated and averaged over all combinations of ($\langle j, l\rangle$), where

$$g^{(2)}_{j,l} = \frac{\langle \sigma_j^+ \sigma_l^+ \sigma_j^- \sigma_l^- \rangle}{\langle \sigma_j^+ \sigma_j^- \rangle \langle \sigma_l^+ \sigma_l^- \rangle}, \quad n_j = \mathrm{tr}(\sigma_j^+ \sigma_j^- \rho_{ss})$$

For completeness, the average real part of $\Re\left[\mathrm{tr}\left(\sigma^- \rho_{ss}\right)\right]$ at each lattice site is also shown. The steady state values are found as follows. Initialising the system in maximally mixed product state, the iPEPO steady state for one set of parameters D, χ and $\epsilon_{D'}$ are found. Convergence in time is achieved when all expectation values o up to next nearest neighbour terms meet a convergence criterion of $\epsilon_t < 10^{-6}$ where

$$\epsilon_t = \frac{\left|\mathrm{tr}\left(o\rho_{t+\tau}\right) - \mathrm{tr}\left(o\rho_t\right)\right|}{\left|\mathrm{tr}\left(o\rho_t\right)\right|\tau}.$$

For higher bond dimensions the steady state iPEPO calculated for one set of parameters is used as an initial state for the next set until convergence to the desired precision is

achieved.

The results generated using this procedure are presented in TABLE 4.1 alongside the results for the same model for the same parameters calculated using the CSRM. As the variational parameters of the iPEPO algorithm are increased, the steady state values converge well. In particular, good convergence is observed in the results for $D = 4$ and $D = 5$. The on-site average expectation values n and $\Re(\langle\sigma^-\rangle)$ change only slightly from their MF $D = 1$ values as the bond dimension is increased. The nearest neighbour correlation function $g^{(2)}_{\langle j,l\rangle}$ is unity for the case of $D = 1$ whereas the system exhibits nearest neighbour bunching ($g^{(2)}_{j,l} > 1$) for $D > 1$ which is in agreement with the predictions of CSRM.

Although the values calculated using the iPEPO algorithm converge as the variational parameters are increased and are close to the results of the CSRM, there is a small discrepancy between the two sets of results. We might expect that increasing the CSRM lattice size $N_x \times N_y$ will converge towards the iPEPO method which represents the thermodynamic limit directly, instead it is found that the opposite is true; a lattice size of 4×4 is in closer agreement to the converged iPEPO results than a lattice size 8×8.

The source of the discrepancy is not clear however it could arise from a few different areas. For example it may result from finite size effects or a translational symmetry breaking, which could be present in the $N_x \times N_y$ results which are averaged over the lattice, such edge effects would not arise in the iPEPO solution. By choosing an iPEPO ansatz with a two-site unit cell a two-site translational invariance has been enforced. However, translational symmetry breaking can arise due to tunnelling induced instability, for example this has been observed in the work of [88, 107]. The presence, or otherwise, of any translational symmetry breaking could be investigate using the iPEPO FET+WTG method by increasing the size of the iPEPO unit cell.

An alternative source of the discrepancy might be lack of true convergence in the fi-

nite system size of the CSRM. The steady state expectation values of a driven-dissipative Bose-Hubbard model on a two-dimensional Lieb lattice were addressed in TABLE II of [49]. Those results were calculated using an algorithm based on the Positive-P representation; a method which gives the numerically exact solution provided the associated numerics remain stable. The results of [49] demonstrate that quite large lattices—on the order of 10×10 unit cells of the Lieb lattice—are necessary to achieve good convergence, particularly with respect to the correlations like $g^{(2)}$. A full investigation of the precise origin of this discrepancy is, however, a topic for future exploration.

4.9 Order to Disorder Transition in the Two Dimensional Classical Ising Model

The iPEPO algorithm for Lindblad dynamics can easily be extended to exploring two-dimensional thermal systems using an annealing approach. To our knowledge this was first implemented by the authors of [100] using the SU algorithm. The central idea is that one can describe a thermal state of a Hamiltonian system H in the canonical ensemble as $\rho \propto e^{\beta H}$ up to some normalisation, where $\beta = 1/T$ is an inverse temperature. Noticing that the thermal state can be written as

$$\rho \propto e^{-\beta H} = e^{-\beta H/2} \mathbb{I} e^{-\beta H/2},$$

the maximally mixed state $\mathbb{I}$ can be decomposed as a tensor product and is therefore straightforward to represent exactly as an iPEPO on a two dimensional lattice. Then, by representing the infinite temperature maximally mixed state as $\rho = \mathbb{I}$, one can "anneal" the infinite temperature state down to a temperature T .

The optimisation—or annealing—from the infinite temperature state $\mathbb{I}$ is achieved via imaginary time evolution applied to vector space "ket" of state and to its dual "bra"

space. To reach the desired temperature T, one divides the inverse temperature β into an integer m number of slices, each of which cools the system by some small amount $\Delta\beta = \beta/m$, then by repeated application of the vector and dual space operators $e^{\Delta\beta H/2}$, the state at temperature T can be written as

$$\rho = (e^{\Delta\beta H})^{m/2}\mathbb{I}(e^{\Delta\beta H})^{m/2}.$$

If we consider a two-local Hamiltonian, then the operator $e^{(\Delta\beta/2)H}$ can be well approximated by a Suzuki-Trotter decomposition. Like the case of Lindblad dynamics, it is convenient to work in the vectorised description of the iPEPO such that the propagator in the vectorised space takes the form

$$|\rho(T)\rangle = (e^{-\Delta\beta(H\otimes\mathbb{I}+\mathbb{I}\otimes H^T)})^{m/2}|\mathbb{I}\rangle. \tag{4.11}$$

Note that if we compare this to the propagator use for Lindblad dynamics in equation 4.2 and 4.3, the modifications in equation 4.11 simply involve setting all dissipation rates to zero and changing the sing of the dual space operator. While in [100], the authors use the SU time evolution scheme, here we test whether the method remains accurate using the FET+WTG update scheme.

As a simple example we repeat the numerical experiment of [100] and calculate the order disorder transition in the two-dimensional classical Ising model which was solved exactly by Onsager [133]. In the model, classical spins σ_j reside on a square lattice interact via a homogeneous nearest neighbour interaction governed by the Hamiltonian

$$H = -J\sum_{\langle j,k\rangle}\sigma_j\sigma_k.$$

The exact solution shows that there is a first order phase transition from a high temperature disordered phase to a low temperature phase in which the spins are ordered at a

critical temperature T_c which obeys the equation $\sinh(2J/\kappa T_c)^2 = 1$, where $\beta_c = 1/\kappa T_c$. The magnetisation as a function of inverse temperature takes the for $m = (1-k^2)^{1/8}$ where $k = 1/\sinh(2J/\kappa T)^2$, valid for $T < T_c$. Below the critical temperature, the magnetisation is zero.

This thermal transition offers a useful—albeit classical—testbed for the iPEPO annealing algorithm. In particular, it serves as a test of whether the algorithm is working as expected. To test the accuracy of the iPEPO annealing algorithm we set $J = 1$, where the critical point is $\beta_c = \sinh^{-1}(1)/2 \approx 0.44$. It is known a priori (see [100]) that, the exact solution can be represented as an iPEPO with bond dimension $D = 2$, we therefore chose this value in all of the following numerical experiments. To begin, the maximally mixed state is represented as an iPEPO with a two site unit cell and a bond dimension $D = 2$. Then, the state is annealed at a rate of $\Delta\beta$ until the system reaches an inverse temperature $\beta = 1$. The annealing process is repeated using an environment bond dimension $\chi = 16$ and $\Delta\beta \in [0.01, 0.002, 0.001, 0.0005]$. The other parameters associated to the FET and CTMRG algorithms are;$\epsilon_{D'} = 10^{-10}$, $\epsilon_{svd} = 10^{-10}$, $\epsilon_{pinv} = 10^{-8}$, $\epsilon_\chi = 10^{-10}$ and $\epsilon_{FET} = 10^{-10}$.

In Figure 4.23 the results of the iPEPO annealing routine are plotted alongside the exact result. In particular, in Figure 4.23, the magnetisation m_z is found to match the exact result for the majority of the phase diagram. The results show the largest deviation from the exact solution just above the critical temperature $\beta \lessapprox \beta_c$ the likely arises form the difficulty of approximating a discontinuous transition using the imaginary time evolution algorithm which is composed of a sequence of small dynamical maps. Decreasing the time-step makes little difference to the results as observed in Figure 4.23 inset. We have also confirmed that increasing the environment bond dimension do not change the value of the magnetisation, this is because the Hamiltonian is classical and the FET routine—bond truncation optimisation with respect to the environment—is

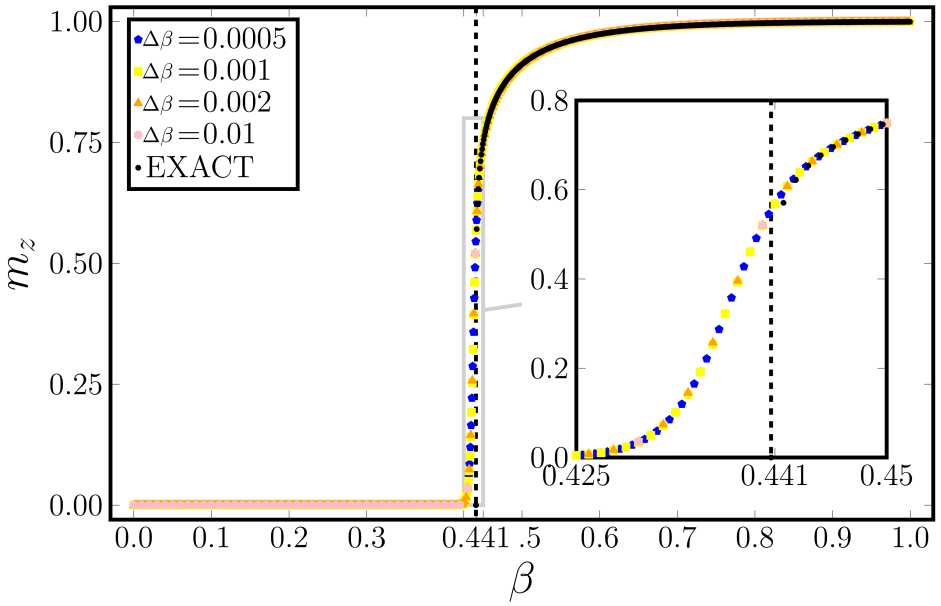

Figure 4.23: Order disorder transition in the two-dimensional classical Ising model calculated using the iPEPO annealing algorithm superimposed with the exact phase diagram. The iPEPO bond dimension $D = 2$ with the environment bond dimension is $\chi = 16$. Above the critical temperature β_c (dashed line) the magnetisation calculated using the iPEPO method agrees well with the exact solution. At temperatures just above the transitions point $\beta \lessapprox \beta_c$however, the iPEPO solution deviates from the exact value ($m_z = 0$) more significantly.

not required.

We have verified that the annealing method accurately captures this classical first order phase transition and is able to plot a phase diagram which is very close to the exact solution. For this classical Hamiltonian, the full machinery of the iPEPO method with gauge fixing and full environment truncation is not necessary, indeed we find that, the FET subroutine is never actually triggered during the annealing process since the Hamiltonian is classical and the enlarged bond dimension does not grow beyond $D = 2$ to warrant its use. The principal sources of error are therefore the Trotter error and any error in calculating the trace effective environment $\mathcal{E}^{\mathrm{tr}}$, particularly near the transition point where correlations can be long ranged. One could attempt to decrease the Trotter error by using a higher order decomposition. In the simplest case this can be achieved by reversing the order of the application of two-local trotter gates at each step in the time evolution. Improvements near the phase transition point could potentially be achieved by using an alternative time evolution method based on MPOs or Runge-Kutta stepper algorithms or moving to a variational approach. The error in calculating $\mathcal{E}^{\mathrm{tr}}$can be improved by increasing the environment bond dimensions χ, or using a more sophisticated renormalisation algorithm, however, we find no improvement above $\chi = 16$.

4.10 Discussion

This chapter concerned TN algorithms for simulating two-dimensional open quantum lattice models. In sections 4.2 and 4.2 the preexisting ansätze, the Projected Entangled Pair State and the Projected Entangled Pair Operator were discussed. In section 4.3 the methods used to calculate effective environments by contracting the two dimensional network using a variant of the Corner Transfer Matrix method given in [62] was discussed in detail. In section 4.4 details of a new algorithm for integrating the Lindblad master equation on an infinite square lattice—which is referred to as FET+WTG—was then

discussed; the key improvement over the existing Simple Update integration technique of [101] was the adaptation of the Full Environment Truncation and gauge fixing to Weighted Trace Gauge presented in [56] to the context of open systems and the iPEPO ansatz. The new algorithm was tested for accuracy against an efficiently solvable model in section 4.6 and it was compared to the Simple Update method of [101]in section 4.7. In section 4.8, the new algorithm was compared to the Corner Space Renormalisation method [60] and in section 4.9, the ability of the method to simulate thermal states using the annealing algorithm of [100] was demonstrated for the simple case of a classical thermal Ising model.

The PEPS was introduced as an example of a two-dimensional TN ansatz, its properties were discussed and important differences distinguishing two-dimensional TNs form one-dimensional TNs were discussed, in particular the additional considerations which arise when using cyclic rather than acyclic tensor networks were addressed. With a view to developing a TN algorithm for two dimensional open quantum systems, the operator analogue of the PEPS, the PEPO was discussed. The PEPO, and its translationally invariant infinite version, the iPEPO, inherit many of the features of the PEPS and iPEPS, in particular the complexity of contraction which arises from the two-dimensional geometry as well as features of operator TN ansätze in one-dimensional systems such as the lack of inherent positivity of the associated density matrix. While the positivity problem is difficult to overcome, it may be possible to use a two-dimensional analogue of a purification ansatz such as locally purified tensor network [186] to guarantee positivity of the density matrix, however, this is likely to come at the cost of larger bond dimensions which are already severely restricted by the complexity of the algorithm.

The role of the effective environments was discussed in some detail, in particular the Hilbert-Schmidt and trace effective environments were introduced and details of a particularly numerically stable variant of the CTMRG algorithm for calculating them

was discussed. Calculation of the effective environments is the most numerically costly step in the FET+WTG algorithm and any significant speedup of the overall algorithm is likely to come from improving the efficiency of this step. There are a range of existing algorithms which could be used to calculate the effective environments including those based on the calculation of fixed points and boundary MPS methods as discussed. The merits of using an alternative algorithm for this step would be an interesting area for exploration. Moreover, it could be interesting the incorporate the Neighbourhood Tensor Update method of [52] which lies somewhere between Simple Update and calculation of the full environment using CTM or boundary MPS methods. Moreover, is likely that any environment calculation algorithm would benefit greatly form implementation on a graphical processing unit (GPU).

The integration of the master equation using a TEBD algorithm was discussed in detail. The key step in the integration is the truncation of enlarged bonds and a Full Environment Truncation (FET) method based on the maximisation of a the fidelity between states with truncated and untruncated bonds was used for this purpose. This framework relied on a very general construction in terms of the so called bond environment introduced in [56]. In our implementation, the FET method required the calculation of the full Hilbert-Schmidt effective environment before each truncation took place. However, it may also be possible to consider alternative bond environments which may be less numerically costly to calculate. For example, one could think of constructing the bond environment from a local cluster of lattice sites, a kind of Partial Environment Truncation similar to [52] with analogies to cluster based algorithms. A very convenient aspect of performing the truncation of enlarged bonds in terms of the bond environment is that the method can easily be generalised to arbitrary networks, so long as the bond environment can be calculated efficiently.

The transverse dissipative Ising model dynamics were compared to those calculated

in an efficiently solvable regime using the method of [64]. The FET+WTG algorithm performed very well in regimes of strong and moderate dissipation and was able to reproduce both local and non-local observables to a high accuracy. For cases of weak dissipation dominated by coherent hopping between lattice sites, the FET+WTG algorithm performed well only at early times but began to deviate from the exact solution later in the time evolution. Furthermore it was possible to solve for the dynamics of the model beyond the narrow efficiently solvable regime necessary for using the method of [64] which would allow allow for a fuller exploration of the phases of the model. An interesting topic of research would be to quantify the dynamical growth of entanglement in this model, particularly in cases for which the FET+WTG method deviates significantly from the exact solution.

To facilitate a comparison between the FET+WTG and SU algorithms, the transverse dissipative Ising model was solved in the regime of moderate dissipation using both algorithms. It was found that the optimal truncations of the FET+WTG method are of central importance in achieving accurate results. Furthermore, by investigating the extent of external correlations by calculating the cycle entropy, it is found that the FET+WTG algorithm curtailed the growth of internal correlations.

For steady states of the driven-dissipative hard core boson model the FET+WTG method the results were found to be comparable to those of the Corner Space Renormalisation method [60], with some small deviations, the origin of which is a topic for future research. In principle it should also be possible to simulate the driven-dissipative Bose-Hubbard model with strong on-site interactions by introducing a local Hilbert space cutoff for the number of bosons allowed on each lattice site.

Inspired by the work of [100] the ability of the FET+WTG method to calculate thermal states was investigated and results were compared to the classical Ising model in two dimensions. In this vein it would be interesting to compare the results of the SU

method to the FET+WTG for calculating thermal states of systems with non-classical correlations such as a transverse quantum Ising model. In this setting it is likely that the FET+WTG method will give more optimal truncations and therefore result in more accurate phase diagrams.

Chapter 5

The Anisotropic Dissipative XY-model on a Square Lattice

Two dimensional systems host a unique set of phenomena in which the dimensionality plays a crucial role in the physics. Consider for example the topological phase transitions mediated by binding and unbinding of vortex-antivortex pairs [97] or phase transitions in the Ising model [133] which have a lower critical dimension of $\mathcal{D} = 2$. In this chapter, aspects of a dissipative anisotropic XY-model on a square lattice are addressed. This model is interesting for a number of reasons. A simple MF solution [108] shows the stabilisation of a spontaneously symmetry broken staggered-XY (sXY) phase in the stationary state, however it is not clear whether the sXY phase remains accessible in a two-dimensional system if fluctuations at the microscopic level are accounted for or if any (quasi-)long range order associated with the sXY phase is present. Furthermore, the model satisfies the criteria of $\mathcal{PT}$-symmetry in the sense of [83] which suggests a transition from a pure state at strong dissipation to a maximally mixed state at very weak dissipation, the character of the transition between the opposite limits of dissipation as dictated by the $\mathcal{PT}$-symmetry is an open question for the spin-1/2 model on a two-dimensional lattice.

The aim of this chapter is to address these questions by solving the model using the FET+WTG algorithm based on the iPEPO ansatz. Firstly, the model is introduced and its symmetries including its identification as being $\mathcal{PT}$-symmetric are discussed. The results of the MF analysis are reviewed in Section 5.2. The findings of other works on the model which use a Keldysh field theory approach are discussed in Section 5.3. The methodology used to address these questions using the iPEPO tensor network method is given in section 5.5 and the results are presented in Section 5.6.

5.1 The Model

The model describes an array of spin-1/2 particles arranged on a a square lattice spanning the plane. The spins interact with their nearest neighbours and with a bath or reservoir via an incoherent dissipation process. The dynamics of the system are modelled using a Lindblad master equation for the system's density matrix ρ

$$\dot{\rho} = -i[H, \rho] + \Gamma \sum_j [\sigma_j^- \rho \sigma_j^+ - \frac{1}{2}(\sigma_j^+ \sigma_j^- \rho + \rho \sigma_j^+ \sigma_j^-)]. \tag{5.1}$$

The Liouvillian which generates this map is referred to succinctly as $\mathcal{L}[H_{XY}; \sqrt{\Gamma}\sigma^-]$, where the Hamiltonian has the form

$$H_{XY} = \frac{J}{z} \sum_{\langle j,k \rangle} \sigma_j^x \sigma_k^x - \sigma_j^y \sigma_k^y = \frac{2J}{z} \sum_{\langle j,k \rangle} \sigma_j^+ \sigma_k^+ + \sigma_j^- \sigma_k^-, \tag{5.2}$$

where σ_j^x, σ_j^y and σ_j^z are the Pauli spin operators at each lattice site and the Hamiltonian is parameterised by the nearest neighbour hopping J and coordination number z. The dissipator in 5.1 is written in terms of the local spin raising and lowering operators $\sigma_j^\pm = \frac{1}{2}(\sigma_j^x \pm \sigma_j^y)$ and describes incoherent dissipation at a rate Γ. The model is parameterised in terms of the dissipation rate by the single parameter J/Γ.

The anisotropy has an important influence on the steady state which can be under-

stood as follows. Each of the spins will experience an effective magnetic field dependent on the orientation of its neighbours. Since the coupling is anisotropic—the $\sigma_j^x\sigma_k^x$ and $\sigma_j^y\sigma_k^y$ terms have opposite sign—the effective field experienced by a spin will be perpendicular to the magnetisation of its neighbouring spins. While spins decaying towards $|\downarrow^z\rangle$ at a rate Γ, the precession from the effective field may be strong enough to counteract the dissipation pointing the spin away from $|\downarrow\rangle$ and exotic forms of magnetism may arise [108].

It is straightforward to solve the simple MF equations for these kinds of dissipative spin models and doing so has shown a wealth of unconventional magnetism, however, studies which include correlations beyond MF show that a qualitatively different picture can emerge. For example, the MF phase diagram of the dissipative XYZ model has been shown [108] to host a range of exotic phases such as ferromagnetic, anti-ferromagnetic and spin density waves. Beyond the basic MF approximation the phase diagram becomes qualitatively different [88]; for example, a transition from a paramagnetic to a ferromagnetic phase, followed by a re-entrance to the paramagnetic phase not predicted by the MF theory has been shown. Furthermore, for the case of a coherently driven dissipative XY-model where the MF theory predicts bistable behaviour coupled with a sharp transition between high- and low-density states, the full solution, where correlations are taken into account, shows that this sharp MF transition is instead replaced by a smooth bunching to antibunching transition [119].

Symmetries

The Liouvillian $\mathcal{L}[H_{XY};\sqrt{\Gamma}\sigma^-]$ 5.1 has a weak—in the sense of [24]—continuous $U(1)$ symmetry between the A and B sublattice spin orientations. This can be shown by defining $U_\phi^z = e^{-i\phi\sum_{uc}(\sigma_A^z-\sigma_B^z)}$ where the sum is over the two-site unit cell and showing that

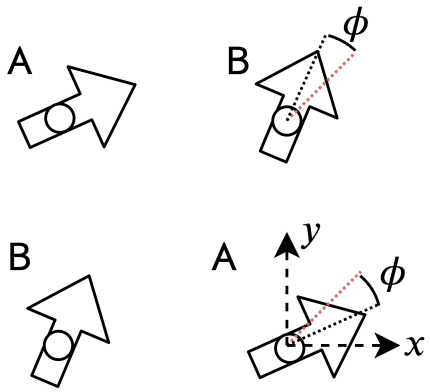

Figure 5.1: A possible spin configuration of a square lattice plaquette in the staggered XY (sXY) phase of the anisotropic dissipative XY-model. In the sXY phase the lattice arranges in a checkerboard patter with two sublattices A and B. In the $x-y$ plane, the spins are staggered by an angle ϕ about the $x=y$ line (dashed red). Spins in the uniform phase (U) which is not shown, have no component along the x or y directions.

$$\mathcal{L}(U_\phi^z \rho U_\phi^{z\dagger}) = U_\phi^z \mathcal{L}(\rho) U_\phi^{z\dagger}.$$

As observed by the authors of [108], in the MF theory steady state solution this continuous symmetry is spontaneously broken and the spins on the A and B sublattices acquire an angle of ϕ and $-\phi$ relative to the $x=y$ line on the Bloch sphere as shown in Figure 5.1. As dictated by the continuous symmetry, any value of ϕ corresponds to a possible solution and this gives rise to topological defects similar to vortices and around which the relative orientation of the two sublattices rotates by 2π.

Recently the authors of [83] generalised the notion of parity-time $\mathcal{PT}$-symmetry to arbitrary open quantum systems for which its definition in terms of a non-Hermitian Hamiltonian is not applicable. The idea is to note that the physical effect of the $\mathcal{T}$ operator is to interchange the role of loss and gain rather than to implement time reversal. For example, in the case of a quantum harmonic oscillator with loss described by a jump operator $c=\sqrt{\Gamma}a$, the transformation between loss and gain is achieved by replacing c with its adjoint $c \to c^\dagger = \sqrt{\Gamma}a^\dagger$. Using this as a guide they consider generic bipartite

quantum systems with a total Hamiltonian H composed of two subsystems A and B which have the same Hilbert space dimension d and which are under the influence of an incoherent dissipation described by local jump operators. Such a system can generically be written a $\mathcal{L}[H; c_A, c_B]$. With this in mind, a definition of $\mathcal{PT}$-symmetry can be written in terms of the anti-unitary transformation for operators,

$$\mathbb{PT}(O) = \mathcal{P}O^{\dagger}\mathcal{P}^{-1} \tag{5.3}$$

where the parity operator $\mathcal{P}$ has the effect of swapping subspaces such that $\mathcal{P}(A \otimes B)\mathcal{P}^{-1} = B \otimes A$. A Liouvillian is then $\mathcal{PT} - symmetric$ if it satisfies the equation

$$\mathcal{L}[\mathbb{PT}(H); \mathbb{PT}(c_A), \mathbb{PT}(c_B)] = \mathcal{L}[H; c_A, c_B], \tag{5.4}$$

which can be generalised if the Liouvillian remains invariant under a unitary U, in which case the parity operator is given by $\mathcal{P} \to \mathcal{P}U$. In Appendix A we follow [83] to show that equation 5.4 is satisfied for the Liouvillian $\mathcal{L}[H_{XY}, \sqrt{\Gamma}\sigma_A^-, \sqrt{\Gamma}\sigma_B^-]$.

Invariance of $\mathcal{L}[H_{XY}, \sqrt{\Gamma}\sigma_A^-, \sqrt{\Gamma}\sigma_B^-]$ with respect to this $\mathcal{PT}$-symmetry implies the existence of stationary states that have parity symmetry which can either be broken or preserved. If the spectrum of H_{XY} is non-degenerate, then the system should tend towards a highly mixed stationary state in the limit of $\Gamma \to 0^+$—i.e. in the limit of vanishingly small but finite dissipation $\rho_{ss}(\Gamma \to 0^+) \propto I$. To show this, the arguments form [83] is recounted here: Consider the Liouvillian $\mathcal{L}[H; c_A, c_B]$, by writing the density operator in the Hamiltonian eigenbasis $\rho = \sum_{n,m} \rho_{n,m}|E_n\rangle\langle E_m|$ where $H|E_n\rangle = E_n|E_n\rangle$, we find that for $\Gamma = 0$,any diagonal state with $\rho_{n,m} = 0$ for $n \neq m$ is a stationary solution of the master equation with populations $p_n = \rho_{n,n}$ not uniquely determined. It can be shown that for small but finite Γ only the fully mixed state is dynamically stable by writing $p_n = 1/d^2 + \delta p_n$where d is the Hilbert space dimension and expanding the master equation up to first order in Γ which gives $\delta\dot{p}_n = \frac{2}{d^2}\langle E_n|[c_A, c_A^{\dagger}] + [c_B, c_B^{\dagger}])|E_n\rangle$. Making

use of the relation $\mathcal{P}c_B\mathcal{P}^{-1} = c_A^\dagger$ and that the eigenstates of the Hamiltonian are also eigenstates of the parity operator $\mathcal{P}|E_n\rangle = \pm|E_n\rangle$ allows to show that $\langle E_n|[c_B, c_B^\dagger]|E_n\rangle = \langle E_n|\mathcal{P}[c_B, c_B^\dagger]\mathcal{P}^{-1}|E_n\rangle = -\langle E_n|[c_A, c_A^\dagger]|E_n\rangle$ which means that $\delta\dot{\rho}_n = 0$. Therefore, in the presence of a small amount of dissipation, the fully mixed state is the stable stationary state. For a more detailed proof which includes a treatment of degenerate eigenstates, the reader is referred to [83].

Of course in many cases, in the limit of strong dissipation $\Gamma \to \infty$, the stationary state will clearly not be anything like the maximally mixed state, consider for example the present case of the anisotropic XY-model where a strong dissipator drives the system to the uniform $|\downarrow^z\rangle$ configuration. The existence of both the pure and maximally mixed phases as limiting cases of J/Γ provides a framework for the investigation of the system's phase diagram and suggests that there should be a transition at intermediate values of J/Γ from a pure to a highly mixed phase. With this in mind, a natural question to ask is: What is the character of this transition for the case of the two-dimensional anisotropic XY-model on a square lattice?

5.2 Mean Field Theory

It is insightful to recount and reproduce the results of the MF theory for the anisotropic dissipative XY-model. The MF (MF) equations for the expectation values $X_j = \langle\sigma_j^x\rangle$, $Y_j = \langle\sigma_j^y\rangle$ and $Z_j = \langle\sigma_j^z\rangle$ of a spin at lattice site j can be written as a set of coupled nonlinear Bloch equations. For a hopping rate J and dissipation rate Γ, these equations

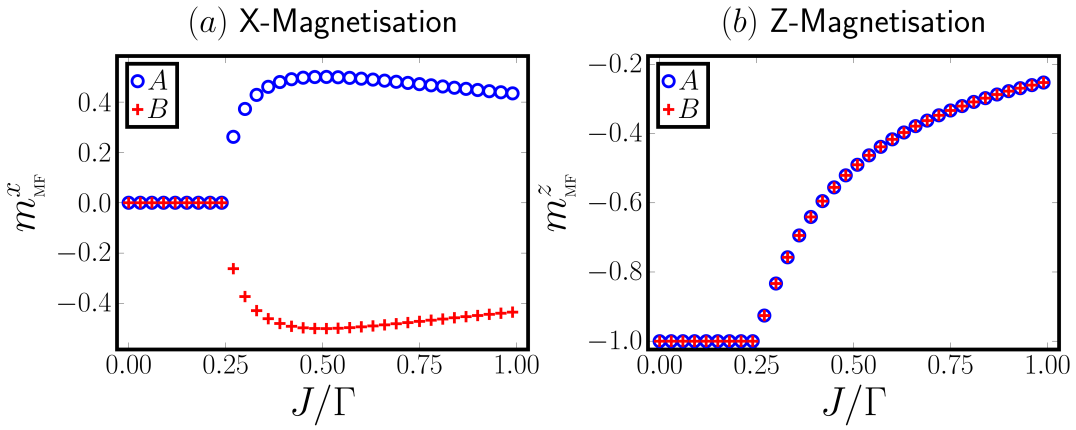

Figure 5.2: MF steady state phase diagram of the anisotropic dissipative XY-model. A phase transition from a uniform (U) phase to a staggered-XY (sXY) phase occurs at a critical field strength of $J/\Gamma = \frac{1}{4}$ above which spins arrange into A and B sublattices which form a checkerboard pattern. The mean field magnetisation (m^x_{MF}) and (m^z_{MF}) across the transition are shown subfigures (a) and (b) respectively. Results are calculated by solving the six coupled MF equations 5.5.

take the form

$$\begin{aligned}
\frac{dX_j}{dt} &= -\frac{\Gamma}{2}X_j - \frac{J}{\mathcal{D}}\sum_m [Z_j Y_m], \\
\frac{dY_j}{dt} &= -\frac{\Gamma}{2}Y_j - \frac{J}{\mathcal{D}}\sum_m [Z_j X_m], \\
\frac{dZ_j}{dt} &= -\Gamma(Z_j + 1) + \frac{J}{\mathcal{D}}\sum_m [Y_j X_m + X_j Y_m].
\end{aligned} \tag{5.5}$$

Here, the integer $\mathcal{D} = z/2$ is the dimension of the cubic lattice and the sum over m runs over the nearest neighbours of the spin at site j. There is always a paramagnetic (PM) solution with $X_j = Y_j = 0$ and $Z_j = -1$, which, via a linear stability analysis (see [108]), is found to be unstable to $\mathcal{D}-$dimensional perturbations with wave vector $\vec{k} = (k_1, k_2, \ldots, k_{\mathcal{D}})$ for $J/\Gamma > 1/4$.

Given that it is known from [108] that this model hosts an sXY phase in which the spins divide into two sublattices A and B with angles $\pm\theta$ relative to the $x = y$ line on the Bloch sphere, the two site spatial inhomogeneity is accounted for by solving a set of six coupled differential equations for the two sets of expectation values X_A, Y_A, Z_A

and X_B, Y_B, Z_B which reside on A and B sublattices respectively, in two dimensions this becomes a checkerboard pattern of A and B sites. To observe this phase in the numerical MF results, we choose initial conditions such that this symmetry is explicitly broken, in particular $X_A = 1$ and $X_B = -1$, and solve for the long time limit of the Bloch equations. The results for a range of $J \in [0, 1]$ are plotted in Figure 5.2.

In Figure 5.2 the magnetisations m^x and m^z are plotted as a function of J/Γ. The transition from the PM phase to the sXY phase at $J/\Gamma = 1/4$ is clearly visible. Above $J/\Gamma = 1/4$, the two sublattice magnetisations m^x_A and m^x_B take equal and opposite values as the lattice splits into two sublattices in an checkerboard pattern as has been shown in Figure 5.1. Also shown are the magnetisations m^z_A and m^z_B. At zero hopping, the dissipation drives the system to the pure product state with $m^x_A = m^z_B = -1$. Above $J/\Gamma = 1/4$ the magnetisation m^z begins to move towards $m^z = 0$ and remains equal across both sublattices for all values of J/Γ.

5.3 Keldysh Field Theory Treatment

The question of whether or not the sXY phase remains stable in a two-dimensional system if corrections beyond MF theory are accounted for has previously been studied using a Keldysh field theory approach in [114]. In that work, an effective model is constructed by mapping the spins to bosons. This approach does not capture the microscopic physics of the spin lattice model, but instead addresses the behaviour of the system in the limit of long wavelengths. Under that approximation it is found that the steady state physics of the effective model is described by a partition function which is in the same universality class as the classical XY-model and therefore, one should expect that there will be a Kosterlitz-Thouless transition if the system is two-dimensional. However it is also predicted by the same authors—based on a simple MF theory analysis which we recount below—that the effective temperature of the system in the steady state will be

greater than the effective Kosterlitz-Thouless temperature associated to the dissipation. Due to this high effective temperature, the ordered phase is predicted to be inaccessible when quantum fluctuations are included and therefore any long range algebraic order which might have been associated to a symmetry broken phase is likely to be absent or at least significantly diminished.

To illustrate the findings of [114] in some more detail, the basic thread of their argument is recounted here, for a detailed derivation we refer the reader to the original publication. After mapping spins to bosons and retaining only the relevant terms, the Keldysh Lagrangian has a partition function of the form

$$\int D\left[\psi(\boldsymbol{x})\right] \exp\left[-\frac{1}{T_{\text{eff}}}\int_{\boldsymbol{x}} \frac{1}{2}\tilde{J}|\nabla\psi|^2 + r|\psi|^2 + u|\psi|^4\right], \tag{5.6}$$

where the effective temperature is $T_{\text{eff}} = \Gamma + \cdots$ and the ellipses represent corrections are due to renormalisation. The important points are that this partition function belongs to the universality class of the classical XY-model and that the effective temperature is of the order of the dissipation rate $T_{\text{eff}} \sim \Gamma$ up to some corrections. In the classical XY-model, a finite temperature transition between a high temperature disordered phase and a low temperature phase with quasi long-range order is possible; the disordering mechanism arises due to the possibility of having topological defects in the form of vortices [91].

The quasi long-range order is realised below a critical temperature T_c which is related to the balance between the energy and entropy cost of forming a vortex; if T_{eff} is the effective temperature then the ordered phase is stable for $\frac{\tilde{J}|\psi|^2}{T_{\text{eff}}} > \frac{2}{\pi}$ [91]. This condition is normally well satisfied at sufficiently low temperatures, however, in this case as $T_{\text{eff}} \to 0$ so does $|\psi|$. In particular from the MF analysis, it is found that $\psi \to 0$ in as $\Gamma \to 0$. To see this, consider that $\psi = 1/\sqrt{2}(\sigma^x + \sigma^y)$ and using $|\langle\sigma^x\rangle| = |\langle\sigma^y\rangle|$ the density term takes the value $|\psi|^2 = 2|\langle\sigma^x\rangle|^2$ which is a quantity which we know from the MF analysis

and takes the value of $|\langle\sigma^x\rangle| = \sqrt{4J\Gamma - \Gamma^2}/4\Gamma$. Putting this together, the condition for the KT transition then takes the form $\frac{1}{4} - \frac{1}{16j} > \frac{1}{\pi}$ where $j \equiv J/\Gamma$. Again from the MF theory we have that $j = J/\Gamma > 1/4$ in the symmetry broken sXY phase, the transition condition is therefore never satisfied. One should expect that any algebraic quasi long-range order in two dimensions will be significantly diminished or completely disappear with the addition of fluctuations.

Clearly all of the above analysis relies heavily on the MF theory. Of course, the MF results are unlikely to remain a good description when quantum fluctuations are properly included, particularly near the transition point. It is therefore interesting to asses whether this simple analysis captures all of the relevant physics or whether properly accounting for microscopic fluctuations by directly solving the microscopic lattice model will give an alternative picture.

5.4 Research Questions

The discussion of the anisotropic dissipative XY-model in terms of its MF solution, its treatment using a Keldysh formalism and its symmetries raises a few open questions. The first question is whether or not the sXY phase remains stable in the two-dimensional model if microscopic quantum fluctuations are included and the spin model is solved directly and without appealing to a long wavelength approximation. The Mermin-Wagner theorem does not hold in this out of equilibrium context and while it is expected that in one dimension there will be no symmetry breaking, whether or not $\mathcal{D} = 2$ is a lower critical dimension for symmetry breaking in this setting remains unclear. This question is particularly relevant near a possible phase boundary where quantum correlations may play a more prominent role. The second question which can be addressed is the form of the correlations in the stationary state; if the sXY phase remains stable, then we might expect quasi long-range algebraic order, on the other hand if it is completely suppressed

then the correlations are likely to be short range. Finally we can address the question of the character of the transition between the pure state at strong dissipation and the maximally mixed state predicted by $\mathcal{PT}$-symmetry as the dissipation tends to zero.

5.5 Methods

iPEPO Steady State Calculations

The dynamics and steady state expectation values are calculated using the FET+WTG iPEPO algorithm presented in Chapter 4. A two-site unit cell with two unique iPEPO tensors A and B is used to represent the system and the environments $\mathcal{E}^{tr}$ and $\mathcal{E}^{hs}$ are calculated using the CTMRG-SVD algorithms. To test the stability of the sXY phase, the iPEPO is initialised in a state for which the $U(1)$ symmetry is explicitly broken, in particular, $\langle\sigma_A^x\rangle = 1$ and $\langle\sigma_B^x\rangle = -1$. From here, steady states for all bond dimensions are calculated up to $D = 4$. For results with bond dimensions $D > 4$, we calculate the steady state for a bond dimension D using that calculated for $D-1$ as an initial state. In all cases, convergence in time is reached when the local expectation values o satisfy the inequality $\epsilon_t < 10^{-6}$, where

$$\epsilon_t = \frac{|\mathrm{tr}\,(o\rho_{t+\tau}) - \mathrm{tr}\,(o\rho_t)|}{|\mathrm{tr}\,(o\rho_t)|\tau}.$$

iPEPO Dynamics Calculations

To explore the dynamical evolution of the system starting from the symmetry broken phase, we first initialise the system in a state for which the $U(1)$ symmetry is explicitly broken then calculate the $D = 1$ steady state. For all higher bond dimensions $D > 1$ shown we initialise the system with the $D = 1$ steady state and then calculate its time evolution up to a total time of $t\Gamma = 50$. At each time step the magnetisations of the

sublattices are measured.

Entanglement Negativity

In assessing the nature of the transition between the pure steady state at large dissipation rates and the maximally mixed state at low dissipation rates, it is useful to employ some measures of non-classical correlations. In particular, we would like to understand the structure of the state from the perspective of entanglement and correlations. Two tools are used in this regard, the first is the entanglement negativity and the second is the von Neumann entropy.

Given that we are working with mixed states, the entanglement negativity $\mathcal{N}$ and the related logarithmic negativity are useful indicators of the presence of entanglement. First defined in [178], entanglement negativity has become an important tool in understanding the structure of mixed state systems. Importantly, it is a easily computable measure of entanglement in that it does not require optimisation over all possible states in the relevant Hilbert space which is the case for some other entanglement measures and in can be computed directly from the bipartite density matrix of a system.

The entanglement negativity $\mathcal{N}(\rho)$ is defined in terms of a generic state ρ of a bipartite system with a finite-dimensional Hilbert space $\mathcal{H}_A \otimes \mathcal{H}_B$. The partial transpose ρ^{T_A} denotes the transposition of the subspace $\mathcal{H}_A$. More precisely, the indices of the partially transposed matrix ρ^{T_A} are related to the density matrix ρ such that $\langle i_A, j_B|\rho^{T_A}|i'_A, j'_B\rangle \equiv \langle i'_A, j_B|\rho|i_A, j'_B\rangle$. With the partial transpose defined, the negativity can be understood as the absolute value of the sum of the negative eigenvalues of ρ^{T_A}. In terms of the trace norm $||M||_1 = \mathrm{tr}\sqrt{M^\dagger M}$, the negativity is defined as $\mathcal{N}(\rho) = \frac{1}{2}(||\rho^{T_A}||_1 - 1)$. This definition comes from the fact that for any Hermitian matrix M, the trace norm is equivalent to the sum of the absolute values of the eigenvalues of M and given that the partial transpose preserves the unit trace of ρ the trace norm of

ρ^{T_A} is related to the negativity as $||\rho^{T_A}||_1 = 1 + 2|\sum_i \mu_i|$, where the μ_i are the negative eigenvalues of ρ^{T_A}.

For any separable state, the partial transpose is also separable such that it remains a positive semidefinite matrix and therefore has zero negativity. As shown in [178], the negativity is an entanglement monotone, meaning that it does not increase under local transformation and it is a convex function of ρ. In practice, if the density matrix is known, then the negativity is easily computed using standard eigenvalue solvers for Hermitian matrices. As noted previously, the iPEPO representation cannot guarantee positivity of the reduced density matrices, it is therefore important to check that this criterion for the proper representation of physical states is fulfilled before calculating negativity.

With the negativity defined we need to choose a subsystem A which is to be transposed. Given the $\mathcal{PT}$-symmetric structure of the Liouvillian discussed previously, it is natural to consider a bipartition between the A and B checkerboard sublattices. This is perhaps a somewhat unusual bipartition—it is more common to consider bipartitions of two blocks of contiguous lattice sites—however, as we shall see in the results, we find no entanglement negativity between sites on the same sublattice and in this case choosing to partially transpose over the space of one of the two sublattices offers insight into the entanglement between the subsystems with respect to which a symmetry breaking may or may not occur.

With this in mind we compute the entanglement negativity with respect to reduced density matrices of differing sizes representing rectangular blocks of spins. In particular we consider reduced density matrices $\rho_{n_x \times n_y}$ where n_x and n_y are the cartesian sizes of the rectangular blocks. The smallest non-trivial $\rho_{n_x \times n_y}$ is $\rho_{2\times 1}$ which contains one spin from the A sublattice and one spin from the B sublattice. In cases where the translational invariance affords more than one equivalent choice of $\rho_{n_x \times n_y}$ we average

over the contributions. For example, for the reduced density matrices involving two lattice sites we have $\mathcal{N}_{2\times1} = \frac{1}{4}[\mathcal{N}(\rho_{2\times1}^{T_A}) + \mathcal{N}(\rho_{2\times1}^{T_B}) + \mathcal{N}(\rho_{1\times2}^{T_A}) + \mathcal{N}(\rho_{1\times2}^{T_B})]$.

Calculation of Correlation Functions

Correlations functions are calculated starting from the steady state iPEPO solution. For a given value of the bond dimension D, the trace effective environment $\mathcal{E}^{\text{tr}}$ is calculated such that convergence is achieved with respect to the environment bond dimension χ^{tr}. By constructing multi-site reduced density matrices, values such as $\langle\sigma_j\sigma_k\rangle$ where j and k are within a few lattice sites of each other, are straightforward to calculate as described in Chapter 4. For example when calculating "off-axis" correlations $\langle\sigma_j\sigma_k\rangle$ in which j and k do not lie on the same row or column of the lattice, it is simplest to first calculate the $n_x \times n_y$ density matrices and then calculate $\text{tr}(\sigma_j \otimes \sigma_k \rho_{n_x\times n_y})$. Using this method limits the off-axis correlations calculated to smaller distances given the cost of calculating $\rho_{n_x\times n_y}$is equivalent the that of contracting a PEPS which is know to be a computationally hard problem in the complexity class $\sharp P$ [157].

To calculate correlation functions at distances $r = |j - k|$ larger than a few lattice sites and along the same row or column, it is convenient to first construct the transfer matrices in the x-direction and the y-direction for each unique iPEPO tensor in the unit cell. For example, calculating longer range correlations in the x-directionas illustrated in Figure 4.14 benefits from first calculating the transfer matrices $Ta^{\text{tr}}T_u^{\text{tr}}$ and $T_d^{\text{tr}}b^{\text{tr}}T_u^{\text{tr}}$, where $a^{tr} = \text{tr}_d(A)$ and $b^{tr} = \text{tr}_d(B)$. The transfer matrices can then be chained together to represent the traced sites between site j and k in the correlation.

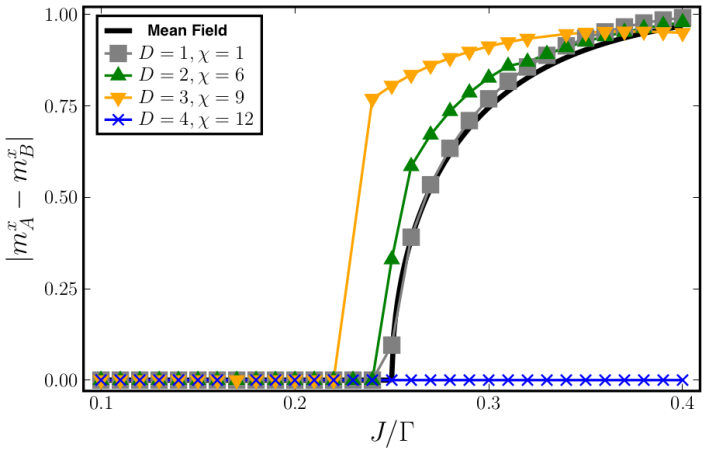

Figure 5.3: Phase diagram close to the transition point. The magnitude of the difference between m^x magnetisations on the A and B sublattices. For the MF theory and the iPEPO up to $D = 3$, a clear transition to the sXY phase is visible. For $D = 4$, the transition is absent.

5.6 Results

Phase Diagram Near the MF Transition

We first find the steady state iPEPO representation of the model for a bond dimension $D = 1$ which is equivalent to a MF solution at a range of values crossing the MF transition point at $J/\Gamma = 0.25$. To do this, the iPEPO is initialised in a in a state for which the symmetry is explicitly broken $\langle \sigma_A^x \rangle = -\langle \sigma_B^x \rangle = 1$ and evolve the system in real time with $D = 1$ until a steady state is reached using the WTG+FET method. Then, using the resulting iPEPO solution as an initial state, fluctuations are systematically introduced by calculating steady states for bond dimensions $D \in [2, 3, 4]$, until convergence in time is reached in each case. Results of this procedure are plotted in Figure 5.3 along with the corresponding results from the MF method.

Comparing first the MF solution to the $D = 1$ iPEPO solution, we find good agreement as expected, while the $D = 1$ solution deviates slightly from the MF solution for $J/\Gamma \gtrapprox 0.3$, the $D = 1$ solution still shows a transition between the PM and sXY

phases at $J/\Gamma = 1/4$. The sXY phase remains stable for bond dimensions of $D = 2$ and $D = 3$ evidenced by the finite value of $S_\perp$, interestingly however, the transition point is shifted to slightly smaller values of J/Γ in both cases, at these bond dimensions, the fluctuations stabilise rather than suppress the sXY phase. Ultimately, for a bond dimension of $D = 4$ the sXY phase is completely suppressed throughout the range of hopping strengths calculated.

It is interesting to consider the reasons behind the qualitative difference between the phase diagram for $D \leq 3$ and $D = 4$—the former show a stable sXY phase while in the latter it appears completely suppressed. Remembering that the Keldysh field theory of [114] concluded that this model's steady state is in the same universality class as the classical XY-model, one might suspect that the disordering mechanism is due to topological defects and perhaps smaller bond dimensions suppress the relevant disordering defects. One possible way to study this feature further would be to try and adapt the entanglement order parameter construction recently introduced in [85] for the study of topological phases in iPEPS to the current iPEPO setting. However, the origin of this feature remains unclear and uncovering it is left for future work.

Dynamics in the sXY Phase

To further study the stability of the sXY phase we calculate the time dynamics of local magnetisations at a particular value of the hopping-dissipation ratio $J/\Gamma = 0.3$. Using the steady state calculated using a bond dimension of $D = 1$ as the initial state for higher bond dimensions, time dynamics are integrated and local expectation values calculated for a total time of $t\Gamma = 50$, at which point we observe a good convergence with respect to time. The results are plotted in Figure 5.4. For a bond dimensions $D = 3$ the system remains in the sXY phase, this is consistent with the phase diagram of Figure 5.3 discussed in the previous section. For $D \in [4, 5, 6]$, however, the spin magnetisation

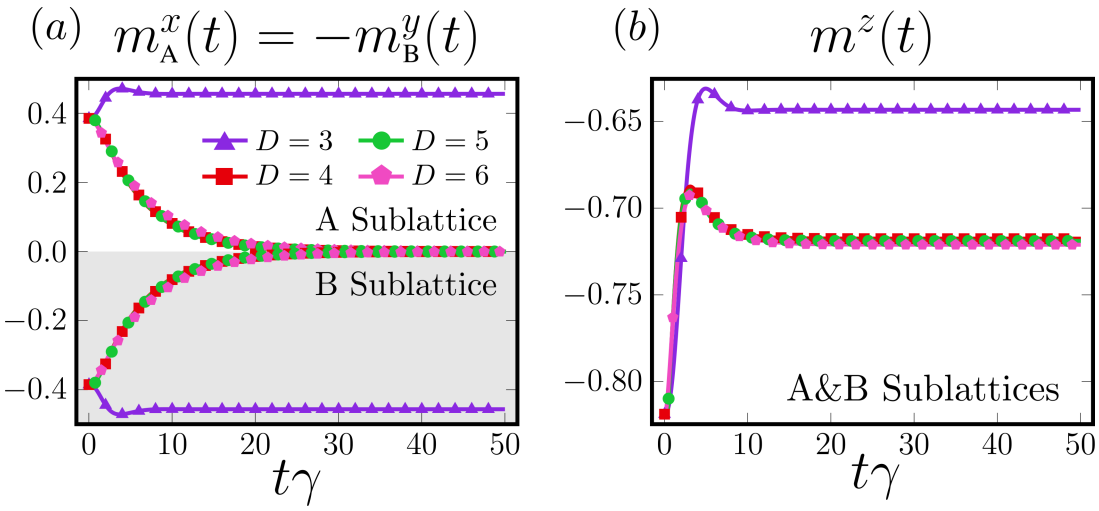

Figure 5.4: The fate of staggered-XY phase at $J/\Gamma = 0.3$. The local magnetisations $m^{x,y,z}(t)$ on the A and B sublattices are calculated as the state evolves from the $D = 1$ steady state solution in which the sXY phase is stable for bond dimensions of increasing sizes $D \in [3, 4, 5, 6]$. For $D = 3$, the system remains in the sXY phase. For $D \in [4, 5, 6]$, the transverse magnetisations m^x and m^y on both sublattices tend towards zero and the sXY is suppressed. The m^z, magnetisation, equal on both sublattices remains finite. The numerics are well converged for $D \geq 5$.

$m^z(t)$, which is uniform across both sublattices, is slightly modified and the magnetisations $m^x(t)$ and $m^y(t)$ on each sublattice tend towards zero such that the continuous symmetry breaking appears to be completely suppressed in the stationary state. The sXY phase therefore appears unstable to quantum fluctuations. These results corroborate the Keldysh field theory predictions of [114] and suggest that the long wavelength fluctuations captured by the approximate theory along with the arguments based on the MF theory are enough to capture the suppression of the sXY phase.

Transition From Pure to Mixed Steady State

In Figures 5.5 and 5.7 we show the phases of the steady states across a range of J/Γ between the limits of large dissipation where the dissipation drives the system to the pure product state with all spins in their $|\downarrow^z\rangle$ configuration and the limit of large hopping where, based on the model's classification as $\mathcal{PT}$-symmetric, the system should tend

towards a maximally mixed steady state. All data points in Figures 5.5 and 5.7 were calculated using the FET+WTG iPEPO method with bond dimensions $D = 6$ and $\chi = 18$ and with a time step of $\tau = 0.005$ for which we find good convergence.

In Figure 5.5 (a) $S_z = \frac{1}{2}(m_A^z + m_B^z)$ and $S_\perp = \frac{1}{2}\sum_{j\in A,B}\sqrt{\langle\sigma_j^x\rangle^2 + \langle\sigma_j^y\rangle^2}$ are plotted as a function of J/Γ. We find that $S_\perp = 0$ for all values of J/Γ which is consistent with the complete suppression of the sXY phase. The magnetisation $S_z = -1$ in the large dissipation limit and varies smoothly as J/Γ increases, consistent with a smooth transition between the two limiting regimes.

In Figure 5.5 (b) the purity of the steady state reduced density matrices $\mathrm{tr}(\rho^2_{n_x\times n_y})$ where $n_x \times n_y$ indicates the number of lattice sites represented by the reduced density matrix is plotted as a function of J/Γ. For each of the sizes $n_x \times n_y$ the reduced density matrices are found to be pure in the limit of large dissipation and tend towards being maximally mixed as the dissipation increases where the minimum purity of an $n_x \times n_y$ reduced density matrix is indicated by the horizontal dashed line. Between the two limiting regimes, the purity of all reduced density matrices varies smoothly as a function of J/Γ.

In Figure 5.6 the negativity for two types of reduced density matrix containing two lattice sites is plotted. As demonstrated in Figure 5.6 inset, the first type (orange data) contains two neighbouring lattice sites along a diagonal from the same sublattice A or B and the second type (blue data) contains one lattice site from each of the two sublattices. The data show that the entanglement negativity between lattice sites on the same sublattice is zero throughout the phase diagram while the negativity is peaked at an intermediate value of J/Γ if it is measured between sublattices. Note that in the data, all possible reduced density matrices of each type have been averaged over.

In Figure 5.7 (a), the entanglement negativity $\mathcal{N}(\rho_{n_x\times n_y})$ for reduced density matrices of different sizes is plotted as a function of J/Γ. In each case, the partial trace is taken

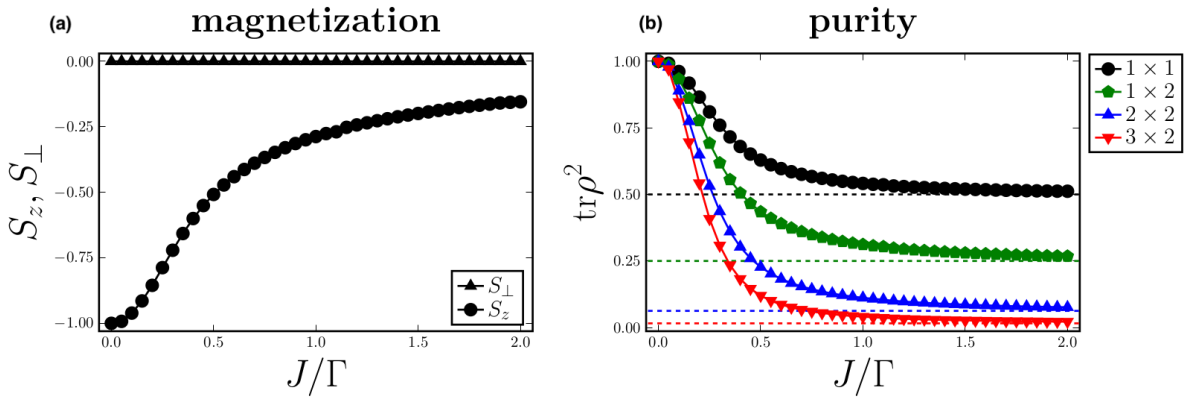

Figure 5.5: (a) The transverse magnetisation $S_\perp = \frac{1}{2}\sum_{j=A,B}\sqrt{\langle\sigma_j^x\rangle^2 + \langle\sigma_j^y\rangle^2}$ remains zero throughout the phase indicating that the symmetry broken phase is suppressed while the magnetisation S_z smoothly towards zero J/Γ is increased. (b) The purity of the system as a function of J/Γ. The purely dissipative dynamics at $J/\Gamma = 0$ drive the system towards a pure state in the $\rho = \bigotimes|\downarrow^z\rangle\langle\downarrow^z|$ configuration while for larger values of the hopping, the reduced density matrices tend towards their maximally mixed phases indicated by the dashed lines.

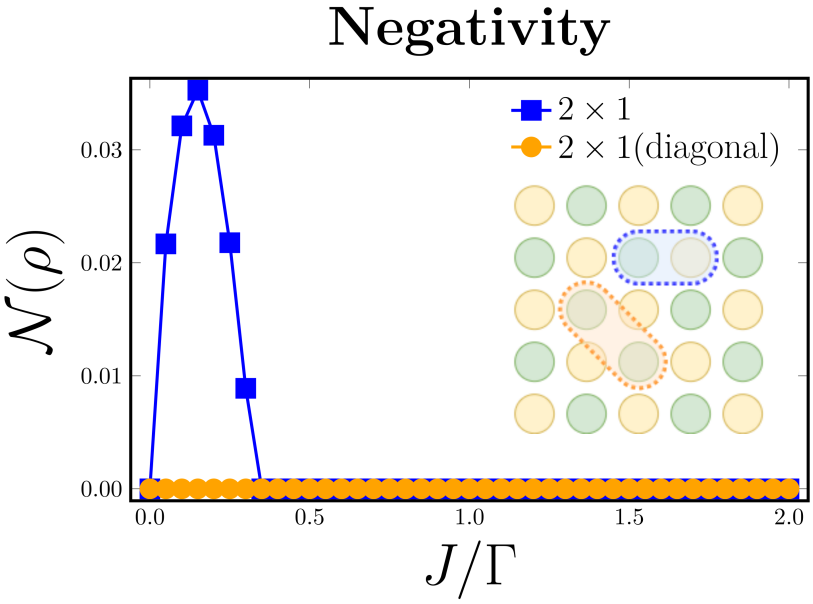

Figure 5.6: Entanglement negativity for reduced density matrices containing two lattice sites as shown in the diagram inset. The partial trace is performed on the space of one two sites. Entanglement negativity between two sites on the same sublattice is zero throughout the phase diagram whereas it is peaked at an intermediate value of J/Γ if each site is from a different sublattices. Note that the negativity has been averaged over all possible reduced density matrix of each type.

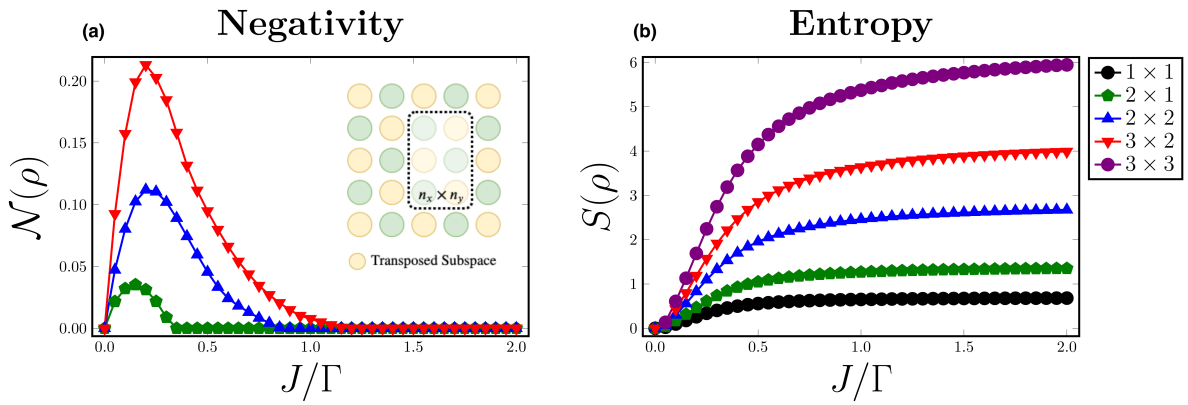

Figure 5.7: (a) The entanglement negativity between the A and B sublattices for reduced density matrices with even numbers of lattice sites shows a peak near the symmetry breaking transition of the MF theory. Inset: The partially transposed reduced density matrices of size $n_x \times n_y$. (b) The von Neumann entropy $S(\rho)$ as a function of J/Γ for reduced density matrices of various sizes.

over the A or B subsystem as discussed in the methods section and indicated in the inset. The data shows that the negativity tends to zero in the limits of small and large dissipation while in between these limits it peaks at a value which is close to the MF critical point at $J/\Gamma = 1/4$. The position of the peak changes by a small amount with respect the size of of the reduced density matrix however it is not clear if this is a systematic effect and it is difficult to assess this given that the reduced density matrices are quite small.

In Figure 5.7 (b) the von Neumann entropy $S(\rho) = -\mathrm{tr}(\rho \ln \rho)$ is plotted as a function of J/Γ for reduced density matrices of varying sizes. The slope of the curves is maximal in the region of the MF transition point $J/\Gamma = 1/4$ and for larger values of the hopping rate, the von Neumann entropy reaches a plateau as the density matrices approach the maximally mixed phase, behaviour which is reminiscent of a second order thermal phase transition [148].

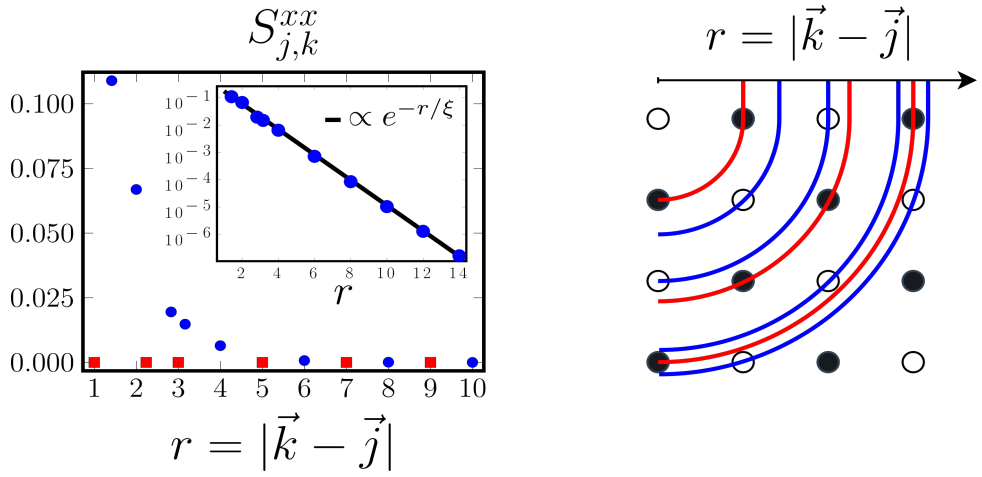

Figure 5.8: Left: The correlation function $S^{xx}_{j,k} = \langle \sigma^x_j \sigma^x_k \rangle$ against distance r displays a staggered form which is a remnant of the sXY phase; the correlations at odd step radii (red squares) are zero while those at even step radii (blue circles) are finite and decaying with r. Left Inset: Exponential fit to even step correlations giving exponent $\xi \approx 0.93$. Right: Odd and even step radii on the square lattice.

Correlations

In Figure 5.8 the correlation function $S^{xx}_{k,j} = \langle \sigma^x_j \sigma^x_k \rangle$ (note that $\langle \sigma^x_j \rangle \langle \sigma^x_k \rangle \approx 0$) is plotted. It shows a staggered structure reminiscent of the sXY phase where correlations at a radii r (see Figure 5.8 (right)) which correspond to an odd number of steps on the lattice are zero, whereas correlations at even step radii are finite and decay with r. If only the even step correlations are considered it is found that the decay is well approximated by an exponential function of the form $S^{xx}_{r\in\text{even}} \propto e^{-r/\xi}$ with $\xi \approx 0.93$. Any long range algebraic order which might have been associated to the symmetry broken phase is not observed in the iPEPO solution. This is consistent with the Keldysh field theory result and would suggests that the system is in the disordered phase. It is important to note once again here that while the iPEPO ansatz can describe an algebraic decay of correlations at least for classical systems, more work needs to be done to assess whether this remains true in the present context. Good convergence is found for $D = 6$ and $\tau\Gamma = 0.005$ resulting in infidelity of truncation $\mathcal{I}(t) < 10^{-9}\ \forall t$.

It is important to note here that, while the iPEPO ansatz can in principle represent algebraic correlation functions, further research needs to be done to assess whether it is capable of faithfully representing algebraic correlations which may appear in the present context. For some classical models such as the thermal Ising model on a square lattice, it is possible to construct an exact representation of the system at any temperature, including the critical temperature $\beta_c = \frac{1}{2}\ln(1+\sqrt{2})$ [133] where correlations decay as $\sim 1/\sqrt{r}$ [133, 173]. Furthermore, an iPEPS ansatz has been used to study criticality in the two-dimensional classical XY-model [169, 194] and the iPEPO used to represent the state of the Bose Hubbard model in [100] where in the latter, spontaneous breaking of the model's $U(1)$ symmetry giving a finite condensate fraction is observed but the authors suggest that the finite bond dimension seems to introduce a finite correlation length in the system and it may be necessary to perform a finite-D scaling to correctly probe the thermodynamic limit. In the present work, it would be interesting to compare correlation functions computed for $D \leq 3$ where local symmetry breaking appears to remain stable to those computed for $D \geq 4$ in order to assess any qualitative difference in the correlation functions between these two regimes.

Convergence

The value of the von Neumann entropy is a good choice to test for convergence since it is sensitive to small changes in the density matrix. This can be seen from the spectral decomposition $S(\rho) = -\mathrm{tr}(\rho \ln \rho) = -\sum_r p_r \ln(p_r)$ where the p_r are the probabilities associated to the spectral decomposition $\rho = \sum_r p_r |\psi_r\rangle\langle\psi_r|$. Due to the logarithmic terms in the summation, $S(\rho)$ is sensitive to small values of p_r. To test the convergence of the numerics the von Neumann entropy of the 2×2 reduced density matrices are plotted for a range of bond dimensions D and environment dimensions χ^{hs} in Figure 5.9 (a) and in (b) of the same Figure, the difference between $S(\rho)$ calculated using

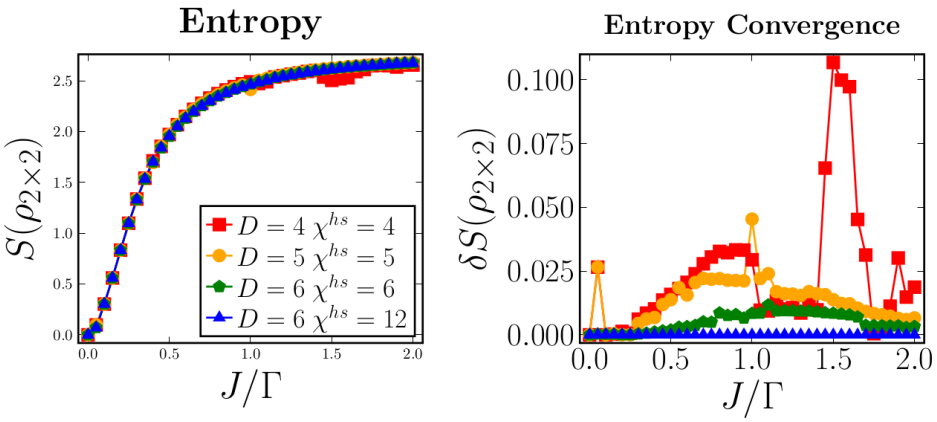

Figure 5.9: (a) The von Neumann entropy $S(\rho) = -\mathrm{tr}(\rho \ln \rho)$ of the $n_x \times n_y = 2 \times 2$ reduced density matrices for a range of bond dimensions D and environment dimensions χ^{hs}. (b) The difference $\delta S_{D,\chi} = |S_{D,\chi} - S_{D_{max},\chi_{max}}|$ where $D_{max} = 6$ and $\chi_{max} = 12$ are the largest values calculated for a range of bond and environment dimensions.

the largest iPEPO parameters $D_{max} = 6$ and $\chi^{hs}_{max} = 12$ and those of lower convergence parameters $\delta S_{D,\chi} = |S_{D,\chi^{hs}} - S_{D_{max},\chi^{hs}_{max}}|$ is given. For $D \geq 6$ the data appear reasonably well converged with $\delta S_{6,6} \lessapprox 0.01$ for all values of J/Γ.

5.7 Discussion

In this chapter the dissipative anisotropic XY-model was studied on a two-dimensional lattice using the FET+WTG iPEPO TN algorithm presented in Chapter 4. In section 5.1 the model was introduced in the Lindblad formalism and its symmetries were discussed, this included as discussion of its identification as $\mathcal{PT}$-symmetric in the sense of [83]. In section 5.2 the mean field description of the model from [108] was reproduced and the symmetry broken staggered phase (sXY) shown. In section 5.3 the Keldysh field theory treatment of the model from [114] was recounted and the expectations of this long wavelength approximation were given, in particular, the steady state physics of the effective model was predicted to belong to the same universality class as the classical XY model but that a the steady state should remain disordered phase throughout the

phase diagram. In section 5.4 a set of research questions were proposed and in section 5.5 the methodology used to integrate the master equation using the iPEPO method and calculate observables was described. Section 5.6 explored the results of the study.

The main result of the is that the symmetry broken sXY phase characterised by the local magnetisation which is stable in the MF approximation appears to be completely suppressed in the iPEPO solution when correlations are taken into account above a bond dimension $D \geq 4$. This finding is broadly in line with the long wavelength Keldysh field theory treatment which predicts a disordered steady state in two dimensions. indeed, by calculating the dynamics of the system initialised in the symmetry broken sXY phase we find that finite magnetisations m_A^x and m_B^x characteristic of the sXY phase rapidly decay to zero. In an attempt to further characterise the nature of the steady state the phase diagram parameterised by the ratio of the hopping and dissipation J/Γ was calculated using the FET+WTG method for a range of iPEPO bond dimensions. Interestingly, while the sXY phase appears to be suppressed for bond dimensions $D \geq 4$ the sXY phase appears to remain stable for bond dimensions $D \leq 3$, an interesting research direction would be to assess the reason behind this qualitative change in the iPEPO solution and this may give insight into the disordering mechanism.

As discussed in section 5.1, apart from the $U(1)$ symmetry, the model is also $\mathcal{PT}$-symmetric in the parlance of [83]. This suggests a transition between a pure steady state in the limit of large dissipation and a highly mixed steady state in the limit of vanishing dissipation. The character of the transition between these two limits was investigated by calculating a range of quantities in the steady state, these included: local observables, the purity of reduced density matrices of different sizes $N_x \times N_y$, the von Neumann entropy and the entanglement negativity between A and B sublattices. From these results it was found that, in contrast to the MF solution, the transition mapped out by local observables is smooth. The purity of the finite sized reduced density matrices

transition smoothly from the pure to a highly mixed phases while the von Neumann entropy which is zero in the limit of large dissipation smoothly increases and plateaus as the dissipation decreases. To further characterise the purity of the state in the limit $\Gamma \to 0^+$it may be instructive to calculate the overlap of the unit cell iPEPO with an iPEPO representation of the maximally mixed state which can be constructed exactly. Furthermore, it would be interesting to assess whether the order of limits is important in this context: there are three limits to consider; the limit of time $t \to \infty$, system size $N \to \infty$ and dissipation rate $\Gamma \to 0^+$.

Interestingly the entanglement negativity calculated between two sites on the same sublattice is zero throughout the phase diagram, whereas, if the two sites are from different sublattices then the negativity is peaked at an intermediate value of J/Γ. Considering larger reduced density matrices and taking a partial trace over one of the two sXY sublattices it is found that the entanglement negativity is peaked in the region of the MF sXY transition at J/Γ. This suggests that entanglement is playing a role in the transition and it would be interesting to investigate this further; for example, by performing a finite size scaling analysis of the negativity and entropy or assessing alternative entanglement measures such as the mutual information.

By observing the correlation function $S^{xx}_{j,k}$ as a function of distance $r = |k - j|$ it is found that all correlations associated to odd numbers of lattice steps are zero while the even step correlations decay exponentially with distance. This appears to agree with the Keldysh field theory prediction, however more research needs to be done on whether the iPEPO ansatz is capable of faithfully representing an algebraic decay of correlations in this particular context. Nevertheless, the results appear to point towards a disordered steady state where an even-odd remnant of the sXY pattern is present in the correlations. To further characterise the steady state, it would be instructive to calculated other correlation functions in the model and compare these across different

bond dimensions, in particular, it would be interesting to assess any differences in the nature of the correlation functions between the ordered phases which appear to be stable at $D \leq 3$ and for $D \geq 4$.

Further possibilities in this direction are to model other systems which obey $\mathcal{PT}$-symmetric which could include alternating gain and loss. Alternatively, small deviations from the perfect $\mathcal{PT}$-symmetric could be studied in order to establish the stability with respect to perturbations of the results discussed in this chapter. As mentioned in the introduction, the general dissipative XYZ model of which the anisotropic dissipative XY-model is a special case, hosts a remarkable array of unconventional magnetic phases at the MF level. It would be interesting to study these models beyond MF theory particularly to probe the nature of phenomena which may be robust to—or arise from—the addition of quantum correlations.

Chapter 6

Conclusions and Future Work

Open many-body quantum lattice models describe many-body quantum systems which interact with their environment, for example via an external drive or some incoherent dissipative processes which requires an inherently non-equilibrium description. The subject of this thesis was the development of numerical tensor network methods to treat open many-body quantum lattice models. This chapters briefly reviews the content and findings of the thesis and suggests possible directions for future work.

6.1 Conclusion

Chapter 1 introduced the basic concepts of open quantum lattice models and the Lindblad master equation. It also discussed some of the phenomena related to open quantum lattice models, such as time crystallinity and non-equilibrium criticality. The extra richness provided by the non-equilibrium nature of these systems is likely to give rise to new and unexplored phenomena. Some of the numerical techniques which have been developed over the years to tackle open many-body quantum lattice modes were also discussed in Chapter 1. These included stochastic methods, phase space methods and cluster based methods among others, all of which aim to make progress beyond mean

field theories. It is clear from this discussion that there is no single ideal approach and that, depending on the nature of the system being studied, one or more of these methods will be more appropriate than the others.

In Chapter 2, tensor network methods for one-dimensional systems were introduced. This began with a bottom-up discussion of the structure of the tensor network ansatz from the perspective of closed quantum systems governed by Hamiltonians and drew upon notions related to correlations and entanglement which, as it turns out, lie at the heart of why tensor network methods have been so successful in this domain. The various tensor network ansatze associated to one-dimensional systems, including the Matrix Product State and the Matrix Product Operator where then introduced. Following this, a brief review of literature surrounding the various tensor network algorithms intended for open quantum systems was given. This discussion revealed the array of differing approaches which can be used to simulate open quantum systems using tensor networks. Chapter 2 concluded with a more detailed description of a tensor network algorithm for calculating steady states of one-dimensional open quantum lattice models in the framework of a cluster mean field theory.

The work presented in Chapter 3 focussed on the numerical modelling of steady state properties of a dissipative Jaynes-Cummings-Hubbard model with a two-photon drive. This model described a coupled resonator array where, in each resonator, a two-level systems coupled to the resonator modes. The numerical experiments probed the steady state properties of the system for coupled resonator arrays of different sizes. This allowed for a finite size scaling analysis with respect the critical exponents of the quantum Ising model similar to the work of [147]. From the results it was concluded that the one-dimensional Jaynes-Cummings-Hubbard model can act as a quantum simulator of the quantum Ising model at a finite temperature.

In Chapter 4 the focus shifted to two-dimensional tensor network methods where the

Project Entangled Pair State was discussed as the natural generalisation of the Matrix Product State. Some of the additional complexities associated to higher dimensional tensor networks were briefly discussed, these included the high computational cost of contracting a PEPS and the extra care needed to deal with internal correlations. Moving to open systems, as in [101] the Projected Entangled Pair Operator was considered as an ansatz for open quantum lattice models on a square lattice. The bulk of Chapter 4 was devoted to the details of an algorithm for calculating time dynamics and steady states based on the iPEPO ansatz. One of the key developments of this method was the identification of two types of effective environment: the trace effective environment was used to calculate reduced density matrices of the system which the Hilbert-Schmidt effective environment was used during the algorithm to find optimal truncations of enlarged bonds. The method introduced for optimising truncations was another of this chapter's key developments, the method adapted much of the machinery of [56] to the open systems context, in particular, truncations were optimised with respect to a objective function appropriate for open systems using the method of Full Environment Truncation. Other important details of the algorithms such as gauge fixing and measurement procedures were also presented. Chapter 4 concluded by testing the newly developed algorithm against exactly solvable cases and results from the literature in dissipative and driven-dissipative regimes. It was found that the algorithm performed well in regions where the mean field gave incorrect results, reproducing exact results to good accuracy. The method was also found to be easily adaptable to studying thermal systems and was tested against the exactly solvable classical Ising model. Although, no great advantage is observed by using the Full Environment Truncation technique in this setting, it is expected that it would improve the accuracy of numerical results in the case of a non-classical thermal model, such as a transverse quantum Ising model.

In Chapter 5 the iPEPO algorithm presented in Chapter 4 was used to study aspects

of an anisotropic dissipative XY-model on a square lattice. It was found that the unconventional magnetism observed in the mean field theory, a symmetry breaking transition to a staggered sXY phase appeared to be completely suppressed in the tensor network solution as quantum fluctuations were included. The model was parameterised by the ratio of the nearest neighbour hopping and the strength of dissipation which moved the system from a pure state in the limit of large dissipation to a maximally mixed state in the limit of weak dissipation. The transition was found to be smooth and featured a peak in the entanglement negativity between two checkerboard sublattices. Spatial correlation functions suggested that correlations decayed exponentially in space such that the system was not in an ordered phase but that a staggered structure in the correlations showed remnants of the sXY phase of the mean field theory.

6.2 Future Work

In terms of one-dimensional systems, it would be interesting to explore alternative optimisation protocols in the non-equilibrium open systems context. For example, instead of truncating with respect to the Frobenius norm distance, equivalent to discarding the smallest Schmidt coefficients in the TEBD setting, one could think of optimising with respect to a different norm. For example, the work of [187] simulated thermalisation of a closed quantum system using a TEBD algorithm with a a more sophisticated truncation scheme than the standard Frobenius method which preserved local symmetries.

In the context of the dissipative Jaynes-Cummings-Hubbard model with a two photon drive there are many avenues for exploration. With the Matrix Product Operator steady state representation at hand, it would be straightforward to correlation functions and spin structure factors. These non-local observables would give more insight into the nature of the system. The behaviour of the system as a function of the rate of single photon dissipation would be an interesting topic, in principle, the strength of the single-

photon dissipation should behave like the effective temperature of the system, further analogies could then be drawn with equilibrium systems. One advantage of the Jaynes-Cummings-Hubbard model over the Bose-Hubbard model is the ability to tune the details of the two-level system. In this vein, it would be interesting to explore the physics of the system in the atomic limit of the model where the qubit component of the polariton dressed states are dominant. Other avenues for exploration are transport properties of the system and the nature of quenches across the transition point where defects associated to spins and bosons could be investigated.

Numerical tensor network methods for two-dimensional open quantum systems remain very much in their infancy. As such there is a lot of room for improvement. The Full Environment Truncation framework presented in Chapter 4 can be adapted in many ways. Thanks to its construction in terms of the bond environment, the optimisation routine could be adapted in several ways. The bond environment construction is agnostic to the geometry of the network; optimisation of truncation of bonds on an arbitrary network geometry can be achieved in principle, so long as the bond environment can be calculated efficiently. For example, instead of calculating the full environment which is numerically costly algorithm, one could consider constructing the bond environment using a local set of tensors. A Partial Environment Truncation like this would have analogies to more traditional cluster based methods. Alternatively, one could specialise to finite size systems and calculate the bond environment by exactly or approximately contracting the network, some approximate contraction schemes might make this possible for example [112]. Extending the range of more traditional cluster mean field algorithms by representing the cluster as a finite size PEPO could be an interesting direction.

In the context of calculating the full environment there is likely much room for optimisation of the numerical routines used, particularly in the CTMRG environment calculation steps which could find significant, for example on a Graphical Processing

Unit or using a fixed point method, see for example [62]. Moreover, there are a number of ways one could conceive of calculating the environment beyond the framework of Corner Transfer Matrices, for example using a boundary MPS based approach [90].

The topic of non-Markovian master equations was not discussed in this thesis, however, these systems can also be modelled in the framework of tensor networks, see for example [164]. Modelling two-dimensional non-Markovian systems using tensor networks is likely a challenging problem, nevertheless it is possible that some progress can be made in this direction.

Extensions to larger unit cells is another obvious research direction, all elements of the work presented generalise to larger unit cells in a straightforward manner, albeit with extra computational complexity. The simulation of larger unit cells could be used to investigate any translational symmetry breaking or tunnelling induced instabilities which may not be captured if the unit cell is too small. Furthermore one could think about alternatives to the square lattice iPEPO, in the same way as is done in PEPS simulations (see for example [86]), Ruby, hexagonal, and even more complicated lattices could be treated.

The anisotropic dissipative XY model on the square lattice did not reveal an ordered phase when quantum correlations were included. A very interesting direction would be to study the phase diagram of the more general XYZ model or dissipative transverse Ising model in detail using the iPEPO algorithm, these models have both shown evidence of an ordered phase in two dimensions, see for example [88, 89, 101, 183].

References

[1] Albert, V.V. and Jiang, L. *Symmetries and conserved quantities in lindblad master equations*. Phys. Rev. A, **89**, 022118 (2014). doi:10.1103/PhysRevA.89.022118.

[2] Amo, A. and Bloch, J. *Exciton-polaritons in lattices: A non-linear photonic simulator*. Comptes Rendus Physique, **17**, 8, 934–945 (2016). doi:10.1016/j.crhy.2016.08.007. Polariton physics / Physique des polaritons.

[3] Aolita, L., de Melo, F., and Davidovich, L. *Open-system dynamics of entanglement:a key issues review*. Reports on Progress in Physics, **78**, 4, 042001 (2015). doi:10.1088/0034-4885/78/4/042001.

[4] Arute, F., Arya, K., Babbush, R., Bacon, D., Bardin, J.C., Barends, R., Biswas, R., Boixo, S., Brandao, F.G.S.L., Buell, D.A., Burkett, B., Chen, Y., Chen, Z., Chiaro, B., Collins, R., Courtney, W., Dunsworth, A., Farhi, E., Foxen, B., Fowler, A., Gidney, C., Giustina, M., Graff, R., Guerin, K., Habegger, S., Harrigan, M.P., Hartmann, M.J., Ho, A., Hoffmann, M., Huang, T., Humble, T.S., Isakov, S.V., Jeffrey, E., Jiang, Z., Kafri, D., Kechedzhi, K., Kelly, J., Klimov, P.V., Knysh, S., Korotkov, A., Kostritsa, F., Landhuis, D., Lindmark, M., Lucero, E., Lyakh, D., MandrÃ , S., McClean, J.R., McEwen, M., Megrant, A., Mi, X., Michielsen, K., Mohseni, M., Mutus, J., Naaman, O., Neeley, M., Neill, C., Niu, M.Y., Ostby, E., Petukhov, A., Platt, J.C., Quintana, C., Rieffel, E.G., Roushan, P., Rubin, N.C., Sank, D., Satzinger, K.J., Smelyanskiy, V., Sung, K.J., Trevithick, M.D.,

Vainsencher, A., Villalonga, B., White, T., Yao, Z.J., Yeh, P., Zalcman, A., Neven, H., and Martinis, J.M. *Quantum supremacy using a programmable superconducting processor.* Nature, **574**, 7779, 505–510 (2019). doi:10.1038/s41586-019-1666-5.

[5] Barthel, T., Schollwöck, U., and White, S.R. *Spectral functions in one-dimensional quantum systems at finite temperature using the density matrix renormalization group.* Phys. Rev. B, **79**, 245101 (2009). doi:10.1103/PhysRevB.79.245101.

[6] Bartolo, N., Minganti, F., Casteels, W., and Ciuti, C. *Exact steady state of a kerr resonator with one- and two-photon driving and dissipation: Controllable wigner-function multimodality and dissipative phase transitions.* Phys. Rev. A, **94**, 033841 (2016). doi:10.1103/PhysRevA.94.033841.

[7] Bartolo, N., Minganti, F., Lolli, J., and Ciuti, C. *Homodyne versus photon-counting quantum trajectories for dissipative kerr resonators with two-photon driving.* The European Physical Journal Special Topics, **226**, 12, 2705–2713 (2017). doi:10.1140/epjst/e2016-60385-8.

[8] Baxter, R.J. *Dimers on a rectangular lattice.* Journal of Mathematical Physics, **9**, 4, 650–654 (1968). doi:10.1063/1.1664623.

[9] Baxter, R.J. *Variational approximations for square lattice models in statistical mechanics.* Journal of Statistical Physics, **19**, 5, 461–478 (1978). doi:10.1007/BF01011693.

[10] Bell, J.S. *On the einstein podolsky rosen paradox.* Physics Physique Fizika, **1**, 195–200 (1964). doi:10.1103/PhysicsPhysiqueFizika.1.195.

[11] Bellman, R. *Dynamic programming princeton university press princeton.* New Jersey Google Scholar (1957).

[12] Bennett, C.H., DiVincenzo, D.P., Smolin, J.A., and Wootters, W.K. *Mixed-state entanglement and quantum error correction*. Phys. Rev. A, **54**, 3824–3851 (1996). doi:10.1103/PhysRevA.54.3824.

[13] Bethe, H.A. and Bragg, W.L. *Statistical theory of superlattices*. Proceedings of the Royal Society of London. Series A - Mathematical and Physical Sciences, **150**, 871, 552–575 (1935). doi:10.1098/rspa.1935.0122.

[14] Biella, A., Jin, J., Viyuela, O., Ciuti, C., Fazio, R., and Rossini, D. *Linked cluster expansions for open quantum systems on a lattice*. Phys. Rev. B, **97**, 035103 (2018). doi:10.1103/PhysRevB.97.035103.

[15] Biondi, M., Lienhard, S., Blatter, G., Türeci, H.E., and Schmidt, S. *Spatial correlations in driven-dissipative photonic lattices*. New Journal of Physics, **19**, 12, 125016 (2017). doi:10.1088/1367-2630/aa99b2.

[16] Blais, A., Grimsmo, A.L., Girvin, S.M., and Wallraff, A. *Circuit quantum electrodynamics*. Rev. Mod. Phys., **93**, 025005 (2021). doi:10.1103/RevModPhys.93.025005.

[17] Blatt, R. and Roos, C.F. *Quantum simulations with trapped ions*. Nature Physics, **8**, 4, 277–284 (2012). doi:10.1038/nphys2252.

[18] Blatt, R. and Wineland, D. *Entangled states of trapped atomic ions*. Nature, **453**, 7198, 1008–1015 (2008). doi:10.1038/nature07125.

[19] Bloch, I., Dalibard, J., and Nascimbène, S. *Quantum simulations with ultracold quantum gases*. Nature Physics, **8**, 4, 267–276 (2012). doi:10.1038/nphys2259.

[20] Booker, C., Buča, B., and Jaksch, D. *Non-stationarity and dissipative time crystals: spectral properties and finite-size effects*. New Journal of Physics, **22**, 8, 085007 (2020). doi:10.1088/1367-2630/ababc4.

[21] Brandão, F.G.S.L., Cubitt, T.S., Lucia, A., Michalakis, S., and Perez-Garcia, D. *Area law for fixed points of rapidly mixing dissipative quantum systems.* Journal of Mathematical Physics, **56**, 10, 102202 (2015). doi:10.1063/1.4932612.

[22] Brandão, F.G.S.L. and Horodecki, M. *Exponential decay of correlations implies area law.* Communications in Mathematical Physics, **333**, 2, 761–798 (2015). doi:10.1007/s00220-014-2213-8.

[23] Breuer, H.P., Petruccione, F., et al. *The theory of open quantum systems.* Oxford University Press on Demand (2002).

[24] Buča, B. and Prosen, T. *A note on symmetry reductions of the lindblad equation: transport in constrained open spin chains.* New Journal of Physics, **14**, 7, 073007 (2012). doi:10.1088/1367-2630/14/7/073007.

[25] Buča, B., Tindall, J., and Jaksch, D. *Non-stationary coherent quantum many-body dynamics through dissipation.* Nature Communications, **10**, 1, 1730 (2019). doi:10.1038/s41467-019-09757-y.

[26] Cahill, K.E. and Glauber, R.J. *Density operators and quasiprobability distributions.* Phys. Rev., **177**, 1882–1902 (1969). doi:10.1103/PhysRev.177.1882.

[27] Cai, Z. and Barthel, T. *Algebraic versus exponential decoherence in dissipative many-particle systems.* Phys. Rev. Lett., **111**, 150403 (2013). doi:10.1103/PhysRevLett.111.150403.

[28] Carmichael, H.J. *Statistical methods in quantum optics 2: Non-classical fields.* Springer Science & Business Media (2009).

[29] Carusotto, I. and Ciuti, C. *Spontaneous microcavity-polariton coherence across the parametric threshold: Quantum monte carlo studies.* Phys. Rev. B, **72**, 125335 (2005). doi:10.1103/PhysRevB.72.125335.

[30] Carusotto, I. and Ciuti, C. *Quantum fluids of light.* Rev. Mod. Phys., **85**, 299–366 (2013). doi:10.1103/RevModPhys.85.299.

[31] Chen, C.F., Kato, K., and Brandão, F.G.S.L. *Matrix product density operators: when do they have a local parent hamiltonian?* (2021).

[32] Chiorescu, I., Bertet, P., Semba, K., Nakamura, Y., Harmans, C.J.P.M., and Mooij, J.E. *Coherent dynamics of a flux qubit coupled to a harmonic oscillator.* Nature, **431**, 7005, 159–162 (2004). doi:10.1038/nature02831.

[33] Cirac, J.I., Pérez-García, D., Schuch, N., and Verstraete, F. *Matrix product states and projected entangled pair states: Concepts, symmetries, theorems.* Rev. Mod. Phys., **93**, 045003 (2021). doi:10.1103/RevModPhys.93.045003.

[34] Cirac, J.I. and Zoller, P. *Quantum computations with cold trapped ions.* Phys. Rev. Lett., **74**, 4091–4094 (1995). doi:10.1103/PhysRevLett.74.4091.

[35] Clark, S.R., Prior, J., Hartmann, M.J., Jaksch, D., and Plenio, M.B. *Exact matrix product solutions in the heisenberg picture of an open quantum spin chain.* New Journal of Physics, **12**, 2, 025005 (2010). doi:10.1088/1367-2630/12/2/025005.

[36] Corboz, P., Jordan, J., and Vidal, G. *Simulation of fermionic lattice models in two dimensions with projected entangled-pair states: Next-nearest neighbor hamiltonians.* Phys. Rev. B, **82**, 245119 (2010). doi:10.1103/PhysRevB.82.245119.

[37] Cramer, M. and Eisert, J. *Correlations, spectral gap and entanglement in harmonic quantum systems on generic lattices.* New Journal of Physics, **8**, 5, 71–71 (2006). doi:10.1088/1367-2630/8/5/071.

[38] Cramer, M., Eisert, J., and Plenio, M.B. *Statistics dependence of the entanglement entropy.* Phys. Rev. Lett., **98**, 220603 (2007). doi:10.1103/PhysRevLett.98.220603.

[39] Cubitt, T.S., Lucia, A., Michalakis, S., and Perez-Garcia, D. *Stability of local quantum dissipative systems.* Communications in Mathematical Physics, **337**, 3, 1275–1315 (2015). doi:10.1007/s00220-015-2355-3.

[40] Cui, J., Cirac, J.I., and Bañuls, M.C. *Variational matrix product operators for the steady state of dissipative quantum systems.* Phys. Rev. Lett., **114**, 220601 (2015). doi:10.1103/PhysRevLett.114.220601.

[41] Czarnik, P. and Dziarmaga, J. *Time evolution of an infinite projected entangled pair state: an algorithm from first principles.* Phys. Rev. B 98, 045110 (2018) (2018). doi:10.1103/PhysRevB.98.045110.

[42] Czarnik, P., Dziarmaga, J., and Corboz, P. *Time evolution of an infinite projected entangled pair state: an efficient algorithm.* Phys. Rev. B 99, 035115 (2019) (2018). doi:10.1103/PhysRevB.99.035115.

[43] Dagvadorj, G., Fellows, J.M., Matyjaśkiewicz, S., Marchetti, F.M., Carusotto, I., and Szymańska, M.H. *Nonequilibrium phase transition in a two-dimensional driven open quantum system.* Phys. Rev. X, **5**, 041028 (2015). doi:10.1103/PhysRevX.5.041028.

[44] Daley, A.J. *Quantum trajectories and open many-body quantum systems.* Advances in Physics, **63**, 2, 77–149 (2014). doi:10.1080/00018732.2014.933502.

[45] Dalibard, J., Castin, Y., and Mølmer, K. *Wave-function approach to dissipative processes in quantum optics.* Phys. Rev. Lett., **68**, 580–583 (1992). doi:10.1103/PhysRevLett.68.580.

[46] Dalla Torre, E.G., Demler, E., Giamarchi, T., and Altman, E. *Dynamics and universality in noise-driven dissipative systems.* Phys. Rev. B, **85**, 184302 (2012). doi:10.1103/PhysRevB.85.184302.

[47] De las Cuevas, G., Drescher, T., and Netzer, T. *Separability for mixed states with operator Schmidt rank two.* Quantum, **3**, 203 (2019). doi:10.22331/q-2019-12-02-203.

[48] de las Cuevas, G. and Netzer, T. *Mixed states in one spatial dimension: Decompositions and correspondence with nonnegative matrices.* Journal of Mathematical Physics, **61**, 4, 041901 (2020). doi:10.1063/1.5127668.

[49] Deuar, P., Ferrier, A., Matuszewski, M., Orso, G., and Szymańska, M.H. *Fully quantum scalable description of driven-dissipative lattice models.* PRX Quantum, **2**, 010319 (2021). doi:10.1103/PRXQuantum.2.010319.

[50] Diehl, S., Micheli, A., Kantian, A., Kraus, B., Büchler, H.P., and Zoller, P. *Quantum states and phases in driven open quantum systems with cold atoms.* Nature Physics, **4**, 11, 878–883 (2008). doi:10.1038/nphys1073.

[51] Drummond, P.D. and Gardiner, C.W. *Generalised p-representations in quantum optics.* Journal of Physics A: Mathematical and General, **13**, 7, 2353–2368 (1980). doi:10.1088/0305-4470/13/7/018.

[52] Dziarmaga, J. *Time evolution of an infinite projected entangled pair state: Neighborhood tensor update.* Phys. Rev. B, **104**, 094411 (2021). doi:10.1103/PhysRevB.104.094411.

[53] Eisert, J. *Entanglement and tensor network states.* Modeling and Simulation 3, 520 (2013) (2013).

[54] Eisert, J., Cramer, M., and Plenio, M.B. *Colloquium: Area laws for the entanglement entropy.* Rev. Mod. Phys., **82**, 277–306 (2010). doi:10.1103/RevModPhys.82.277.

[55] Else, D.V., Monroe, C., Nayak, C., and Yao, N.Y. *Discrete time crystals.* Annu. Rev. Condens. Matter Phys., **11**, 1, 467–499 (2020). doi:10.1146/annurev-conmatphys-031119-050658.

[56] Evenbly, G. *Gauge fixing, canonical forms, and optimal truncations in tensor networks with closed loops.* Phys. Rev. B, **98**, 085155 (2018). doi:10.1103/PhysRevB.98.085155.

[57] Evenbly, G. and Vidal, G. *Tensor network renormalization.* Phys. Rev. Lett., **115**, 180405 (2015). doi:10.1103/PhysRevLett.115.180405.

[58] Feiguin, A.E. and Fiete, G.A. *Spectral properties of a spin-incoherent luttinger liquid.* Phys. Rev. B, **81**, 075108 (2010). doi:10.1103/PhysRevB.81.075108.

[59] Feynman, R.P. *Simulating physics with computers.* International Journal of Theoretical Physics, **21**, 6, 467–488 (1982). doi:10.1007/BF02650179.

[60] Finazzi, S., Le Boité, A., Storme, F., Baksic, A., and Ciuti, C. *Corner-space renormalization method for driven-dissipative two-dimensional correlated systems.* Phys. Rev. Lett., **115**, 080604 (2015). doi:10.1103/PhysRevLett.115.080604.

[61] Fisher, M.E. and Barber, M.N. *Scaling theory for finite-size effects in the critical region.* Phys. Rev. Lett., **28**, 1516–1519 (1972). doi:10.1103/PhysRevLett.28.1516.

[62] Fishman, M.T., Vanderstraeten, L., Zauner-Stauber, V., Haegeman, J., and Verstraete, F. *Faster methods for contracting infinite two-dimensional tensor networks.* Phys. Rev. B, **98**, 235148 (2018). doi:10.1103/PhysRevB.98.235148.

[63] Foss-Feig, M., Niroula, P., Young, J.T., Hafezi, M., Gorshkov, A.V., Wilson, R.M., and Maghrebi, M.F. *Emergent equilibrium in many-body optical bistability.* Phys. Rev. A, **95**, 043826 (2017). doi:10.1103/PhysRevA.95.043826.

[64] Foss-Feig, M., Young, J.T., Albert, V.V., Gorshkov, A.V., and Maghrebi, M.F. *Solvable family of driven-dissipative many-body systems.* Physical Review Letters, **119**, 19, 190402 (2017). doi:10.1103/physrevlett.119.190402.

[65] Gangat, A.A., I, T., and Kao, Y.J. *Steady states of infinite-size dissipative quantum chains via imaginary time evolution.* Phys. Rev. Lett., **119**, 010501 (2017). doi:10.1103/PhysRevLett.119.010501.

[66] Gilchrist, A., Gardiner, C.W., and Drummond, P.D. *Positive p representation: Application and validity.* Phys. Rev. A, **55**, 3014–3032 (1997). doi:10.1103/PhysRevA.55.3014.

[67] Gisin, N. and Percival, I.C. *The quantum-state diffusion model applied to open systems.* Journal of Physics A: Mathematical and General, **25**, 21, 5677–5691 (1992). doi:10.1088/0305-4470/25/21/023.

[68] Glasser, I., Sweke, R., Pancotti, N., Eisert, J., and Cirac, I. *Expressive power of tensor-network factorizations for probabilistic modeling.* In H. Wallach, H. Larochelle, A. Beygelzimer, F. d'Alché-Buc, E. Fox, and R. Garnett, editors, *Advances in Neural Information Processing Systems*, volume 32. Curran Associates, Inc. (2019).

[69] Gray, J. and Kourtis, S. *Hyper-optimized tensor network contraction.* Quantum, **5**, 410 (2021). doi:10.22331/q-2021-03-15-410.

[70] Griffiths, D.J. and Schroeter, D.F. *Introduction to Quantum Mechanics.* Cambridge University Press, 3 edition (2018). doi:10.1017/9781316995433.

[71] Gross, C. and Bloch, I. *Quantum simulations with ultracold atoms in optical lattices.* Science, **357**, 6355, 995–1001 (2017). doi:10.1126/science.aal3837.

[72] Grujic, T., Clark, S.R., Jaksch, D., and Angelakis, D.G. *Non-equilibrium many-body effects in driven nonlinear resonator arrays.* New Journal of Physics, **14**, 10, 103025 (2012). doi:10.1088/1367-2630/14/10/103025.

[73] Gu, Z.C., Levin, M., and Wen, X.G. *Tensor-entanglement renormalization group approach as a unified method for symmetry breaking and topological phase transitions.* Phys. Rev. B, **78**, 205116 (2008). doi:10.1103/PhysRevB.78.205116.

[74] Haegeman, J., Cirac, J.I., Osborne, T.J., Pižorn, I., Verschelde, H., and Verstraete, F. *Time-dependent variational principle for quantum lattices.* Phys. Rev. Lett., **107**, 070601 (2011). doi:10.1103/PhysRevLett.107.070601.

[75] Haegeman, J., Lubich, C., Oseledets, I., Vandereycken, B., and Verstraete, F. *Unifying time evolution and optimization with matrix product states.* Phys. Rev. B, **94**, 165116 (2016). doi:10.1103/PhysRevB.94.165116.

[76] Hartmann, M.J. and Carleo, G. *Neural-network approach to dissipative quantum many-body dynamics.* Phys. Rev. Lett., **122**, 250502 (2019). doi:10.1103/PhysRevLett.122.250502.

[77] Hartmann, M.J., Prior, J., Clark, S.R., and Plenio, M.B. *Density matrix renormalization group in the heisenberg picture.* Phys. Rev. Lett., **102**, 057202 (2009). doi:10.1103/PhysRevLett.102.057202.

[78] Hastings, M.B. *Solving gapped hamiltonians locally.* Phys. Rev. B, **73**, 085115 (2006). doi:10.1103/PhysRevB.73.085115.

[79] Hastings, M.B. *An area law for one-dimensional quantum systems.* Journal of Statistical Mechanics: Theory and Experiment, **2007**, 08, P08024–P08024 (2007). doi:10.1088/1742-5468/2007/08/p08024.

[80] Hauschild, J., Leviatan, E., Bardarson, J.H., Altman, E., Zaletel, M.P., and Pollmann, F. *Finding purifications with minimal entanglement.* Phys. Rev. B, **98**, 235163 (2018). doi:10.1103/PhysRevB.98.235163.

[81] Hein, M., Eisert, J., and Briegel, H.J. *Multiparty entanglement in graph states.* Phys. Rev. A, **69**, 062311 (2004). doi:10.1103/PhysRevA.69.062311.

[82] Huang, C., Zhang, F., Newman, M., Ni, X., Ding, D., Cai, J., Gao, X., Wang, T., Wu, F., Zhang, G., Ku, H.S., Tian, Z., Wu, J., Xu, H., Yu, H., Yuan, B., Szegedy, M., Shi, Y., Zhao, H.H., Deng, C., and Chen, J. *Efficient parallelization of tensor network contraction for simulating quantum computation.* Nature Computational Science, **1**, 9, 578–587 (2021). doi:10.1038/s43588-021-00119-7.

[83] Huber, J., Kirton, P., Rotter, S., and Rabl, P. *Emergence of PT-symmetry breaking in open quantum systems.* SciPost Physics, **9**, 4 (2020). doi:10.21468/scipostphys.9.4.052.

[84] Iemini, F., Russomanno, A., Keeling, J., Schiró, M., Dalmonte, M., and Fazio, R. *Boundary time crystals.* Phys. Rev. Lett., **121**, 035301 (2018). doi:10.1103/PhysRevLett.121.035301.

[85] Iqbal, M. and Schuch, N. *Entanglement order parameters and critical behavior for topological phase transitions and beyond.* Phys. Rev. X, **11**, 041014 (2021). doi:10.1103/PhysRevX.11.041014.

[86] Jahromi, S.S., Orús, R., Kargarian, M., and Langari, A. *Infinite projected entangled-pair state algorithm for ruby and triangle-honeycomb lattices.* Phys. Rev. B, **97**, 115161 (2018). doi:10.1103/PhysRevB.97.115161.

[87] Jiang, H.C., Weng, Z.Y., and Xiang, T. *Accurate determination of tensor network*

state of quantum lattice models in two dimensions. Phys. Rev. Lett., **101**, 090603 (2008). doi:10.1103/PhysRevLett.101.090603.

[88] Jin, J., Biella, A., Viyuela, O., Mazza, L., Keeling, J., Fazio, R., and Rossini, D. *Cluster mean-field approach to the steady-state phase diagram of dissipative spin systems*. Physical Review X, **6**, 3, 031011 (2016). doi:10.1103/physrevx.6.031011.

[89] Jin, J., He, W.B., Iemini, F., Ferreira, D., Wang, Y.D., Chesi, S., and Fazio, R. *Determination of the critical exponents in dissipative phase transitions: coherent anomaly approach* (2021).

[90] Jordan, J., Orús, R., Vidal, G., Verstraete, F., and Cirac, J.I. *Classical simulation of infinite-size quantum lattice systems in two spatial dimensions*. Phys. Rev. Lett., **101**, 250602 (2008). doi:10.1103/PhysRevLett.101.250602.

[91] Kardar, M. *Statistical Physics of Fields*. Cambridge University Press (2007). doi:10.1017/cbo9780511815881.

[92] Kastoryano, M.J. and Eisert, J. *Rapid mixing implies exponential decay of correlations*. Journal of Mathematical Physics, **54**, 10, 102201 (2013). doi:10.1063/1.4822481.

[93] Keßler, H., Kongkhambut, P., Georges, C., Mathey, L., Cosme, J.G., and Hemmerich, A. *Observation of a dissipative time crystal*. Phys. Rev. Lett., **127**, 043602 (2021). doi:10.1103/PhysRevLett.127.043602.

[94] Kilda, D., Biella, A., Schiró, M., Fazio, R., and Keeling, J. *On the stability of the infinite projected entangled pair operator ansatz for driven-dissipative 2d lattices*. SciPost Phys. Core, **4**, 1, 005 (2021). doi:10.21468/SciPostPhysCore.4.1.005.

[95] Kliesch, M., Gogolin, C., Kastoryano, M.J., Riera, A., and Eisert, J. *Locality of temperature*. Phys. Rev. X, **4**, 031019 (2014). doi:10.1103/PhysRevX.4.031019.

[96] Kliesch, M., Gross, D., and Eisert, J. *Matrix-product operators and states: Np-hardness and undecidability.* Phys. Rev. Lett., **113**, 160503 (2014). doi:10.1103/PhysRevLett.113.160503.

[97] Kosterlitz, J.M. and Thouless, D.J. *Ordering, metastability and phase transitions in two-dimensional systems.* Journal of Physics C: Solid State Physics, **6**, 7, 1181–1203 (1973). doi:10.1088/0022-3719/6/7/010.

[98] Krämer, S., Plankensteiner, D., Ostermann, L., and Ritsch, H. *Quantumoptics.jl: A julia framework for simulating open quantum systems.* Computer Physics Communications, **227**, 109–116 (2018). doi:10.1016/j.cpc.2018.02.004.

[99] Kraus, C.V. and Osborne, T.J. *Time-dependent variational principle for dissipative dynamics.* Phys. Rev. A, **86**, 062115 (2012). doi:10.1103/PhysRevA.86.062115.

[100] Kshetrimayum, A., Rizzi, M., Eisert, J., and Orús, R. *Tensor network annealing algorithm for two-dimensional thermal states.* Physical Review Letters, **122**, 7, 070502 (2019). doi:10.1103/physrevlett.122.070502.

[101] Kshetrimayum, A., Weimer, H., and Orús, R. *A simple tensor network algorithm for two-dimensional steady states.* Nature Communications, **8**, 1 (2017). doi:10.1038/s41467-017-01511-6.

[102] Kulaitis, G., Krüger, F., Nissen, F., and Keeling, J. *Disordered driven coupled cavity arrays: Nonequilibrium stochastic mean-field theory.* Physical Review A, **87**, 1, 013840 (2013). doi:10.1103/physreva.87.013840.

[103] Landa, H., Schiró, M., and Misguich, G. *Multistability of driven-dissipative quantum spins.* Physical Review Letters, **124**, 4, 043601 (2020). doi:10.1103/physrevlett.124.043601.

[104] las Cuevas, G.D., Cubitt, T.S., Cirac, J.I., Wolf, M.M., and Pérez-García, D. *Fundamental limitations in the purifications of tensor networks*. Journal of Mathematical Physics, **57**, 7, 071902 (2016). doi:10.1063/1.4954983.

[105] las Cuevas, G.D., Schuch, N., Pérez-García, D., and Cirac, J.I. *Purifications of multipartite states: limitations and constructive methods*. New Journal of Physics, **15**, 12, 123021 (2013). doi:10.1088/1367-2630/15/12/123021.

[106] Lazarides, A., Roy, S., Piazza, F., and Moessner, R. *Time crystallinity in dissipative floquet systems*. Phys. Rev. Research, **2**, 022002 (2020). doi:10.1103/PhysRevResearch.2.022002.

[107] Le Boité, A., Orso, G., and Ciuti, C. *Steady-state phases and tunneling-induced instabilities in the driven dissipative bose-hubbard model*. Phys. Rev. Lett., **110**, 233601 (2013). doi:10.1103/PhysRevLett.110.233601.

[108] Lee, T.E., Gopalakrishnan, S., and Lukin, M.D. *Unconventional magnetism via optical pumping of interacting spin systems*. Physical Review Letters, **110**, 25, 257204 (2013). doi:10.1103/physrevlett.110.257204.

[109] Legeza, O. and Sólyom, J. *Quantum data compression, quantum information generation, and the density-matrix renormalization-group method*. Phys. Rev. B, **70**, 205118 (2004). doi:10.1103/PhysRevB.70.205118.

[110] Levin, M. and Nave, C.P. *Tensor renormalization group approach to two-dimensional classical lattice models*. Phys. Rev. Lett., **99**, 120601 (2007). doi:10.1103/PhysRevLett.99.120601.

[111] Lieb, E.H. and Robinson, D.W. *The Finite Group Velocity of Quantum Spin Systems*, pp. 425–431. Springer Berlin Heidelberg, Berlin, Heidelberg (2004). ISBN 978-3-662-10018-9. doi:10.1007/978-3-662-10018-9_25.

[112] Lubasch, M., Cirac, J.I., and Bañuls, M.C. *Unifying projected entangled pair state contractions*. New Journal of Physics, **16**, 3, 033014 (2014). doi:10.1088/1367-2630/16/3/033014.

[113] MacFarlane, A.G.J., Dowling, J.P., and Milburn, G.J. *Quantum technology: the second quantum revolution*. Philosophical Transactions of the Royal Society of London. Series A: Mathematical, Physical and Engineering Sciences, **361**, 1809, 1655–1674 (2003). doi:10.1098/rsta.2003.1227.

[114] Maghrebi, M.F. and Gorshkov, A.V. *Nonequilibrium many-body steady states via keldysh formalism*. Physical Review B, **93**, 1, 014307 (2016). doi:10.1103/physrevb.93.014307.

[115] Makhlin, Y., Schön, G., and Shnirman, A. *Quantum-state engineering with josephson-junction devices*. Rev. Mod. Phys., **73**, 357–400 (2001). doi:10.1103/RevModPhys.73.357.

[116] Marino, J. and Diehl, S. *Driven markovian quantum criticality*. Phys. Rev. Lett., **116**, 070407 (2016). doi:10.1103/PhysRevLett.116.070407.

[117] Masanes, L. *Area law for the entropy of low-energy states*. Phys. Rev. A, **80**, 052104 (2009). doi:10.1103/PhysRevA.80.052104.

[118] Mascarenhas, E., Flayac, H., and Savona, V. *Matrix-product-operator approach to the nonequilibrium steady state of driven-dissipative quantum arrays*. Physical Review A, **92**, 2, 022116 (2015). doi:10.1103/physreva.92.022116.

[119] Mendoza-Arenas, J.J., Clark, S.R., Felicetti, S., Romero, G., Solano, E., Angelakis, D.G., and Jaksch, D. *Beyond mean-field bistability in driven-dissipative lattices: Bunching-antibunching transition and quantum simulation*. Physical Review A, **93**, 2, 023821 (2016). doi:10.1103/physreva.93.023821.

[120] Mermin, N.D. and Wagner, H. *Absence of ferromagnetism or antiferromagnetism in one- or two-dimensional isotropic heisenberg models.* Phys. Rev. Lett., **17**, 1133–1136 (1966). doi:10.1103/PhysRevLett.17.1133.

[121] Minganti, F., Biella, A., Bartolo, N., and Ciuti, C. *Spectral theory of liouvillians for dissipative phase transitions.* Phys. Rev. A, **98**, 042118 (2018). doi:10.1103/PhysRevA.98.042118.

[122] Mitra, A., Takei, S., Kim, Y.B., and Millis, A.J. *Nonequilibrium quantum criticality in open electronic systems.* Phys. Rev. Lett., **97**, 236808 (2006). doi:10.1103/PhysRevLett.97.236808.

[123] Molnar, A., Schuch, N., Verstraete, F., and Cirac, J.I. *Approximating gibbs states of local hamiltonians efficiently with projected entangled pair states.* Phys. Rev. B, **91**, 045138 (2015). doi:10.1103/PhysRevB.91.045138.

[124] Monroe, C., Campbell, W.C., Duan, L.M., Gong, Z.X., Gorshkov, A.V., Hess, P.W., Islam, R., Kim, K., Linke, N.M., Pagano, G., Richerme, P., Senko, C., and Yao, N.Y. *Programmable quantum simulations of spin systems with trapped ions.* Rev. Mod. Phys., **93**, 025001 (2021). doi:10.1103/RevModPhys.93.025001.

[125] Moore, G.E. *Cramming more components onto integrated circuits, reprinted from electronics, volume 38, number 8, april 19, 1965, pp.114 ff.* IEEE Solid-State Circuits Society Newsletter, **11**, 3, 33–35 (2006). doi:10.1109/N-SSC.2006.4785860.

[126] Movassagh, R. and Shor, P.W. *Supercritical entanglement in local systems: Counterexample to the area law for quantum matter.* Proceedings of the National Academy of Sciences, **113**, 47, 13278–13282 (2016). doi:10.1073/pnas.1605716113.

[127] Myatt, C.J., King, B.E., Turchette, Q.A., Sackett, C.A., Kielpinski, D., Itano, W.M., Monroe, C., and Wineland, D.J. *Decoherence of quantum superpositions*

through coupling to engineered reservoirs. Nature, **403**, 6767, 269–273 (2000). doi:10.1038/35002001.

[128] Nagy, A. and Savona, V. *Variational quantum monte carlo method with a neural-network ansatz for open quantum systems.* Phys. Rev. Lett., **122**, 250501 (2019). doi:10.1103/PhysRevLett.122.250501.

[129] Nietner, A., Vanhecke, B., Verstraete, F., Eisert, J., and Vanderstraeten, L. *Efficient variational contraction of two-dimensional tensor networks with a non-trivial unit cell.* Quantum, **4**, 328 (2020). doi:10.22331/q-2020-09-21-328.

[130] Nishino, T. and Okunishi, K. *Corner transfer matrix renormalization group method.* Journal of the Physical Society of Japan, **65**, 4, 891–894 (1996). doi:10.1143/JPSJ.65.891.

[131] Nishino, T. and Okunishi, K. *Corner transfer matrix algorithm for classical renormalization group.* Journal of the Physical Society of Japan, **66**, 10, 3040–3047 (1997). doi:10.1143/JPSJ.66.3040.

[132] Noh, C. and Angelakis, D.G. *Quantum simulations and many-body physics with light.* Reports on Progress in Physics, **80**, 1, 016401 (2016). doi:10.1088/0034-4885/80/1/016401.

[133] Onsager, L. *Crystal statistics. i. a two-dimensional model with an order-disorder transition.* Physical Review, **65**, 3-4, 117–149 (1944). doi:10.1103/physrev.65.117.

[134] Orús, R. *A practical introduction to tensor networks: Matrix product states and projected entangled pair states.* Annals of Physics, **349**, 117–158 (2014). doi:10.1016/j.aop.2014.06.013.

[135] Orús, R. and Vidal, G. *Infinite time-evolving block decimation algorithm beyond*

unitary evolution. Phys. Rev. B, **78**, 155117 (2008). doi:10.1103/PhysRevB.78.155117.

[136] Orús, R. and Vidal, G. *Simulation of two-dimensional quantum systems on an infinite lattice revisited: Corner transfer matrix for tensor contraction.* Phys. Rev. B, **80**, 094403 (2009). doi:10.1103/PhysRevB.80.094403.

[137] Overbeck, V.R. and Weimer, H. *Time evolution of open quantum many-body systems.* Phys. Rev. A, **93**, 012106 (2016). doi:10.1103/PhysRevA.93.012106.

[138] Penrose, R. *A generalized inverse for matrices.* Mathematical Proceedings of the Cambridge Philosophical Society, **51**, 3, 406–413 (1955). doi:10.1017/S0305004100030401.

[139] Percival, I. *Quantum State Diffusion* (2005).

[140] Pirvu, B., Murg, V., Cirac, J.I., and Verstraete, F. *Matrix product operator representations.* New Journal of Physics, **12**, 2, 025012 (2010). doi:10.1088/1367-2630/12/2/025012.

[141] Plenio, M.B., Eisert, J., Dreißig, J., and Cramer, M. *Entropy, entanglement, and area: Analytical results for harmonic lattice systems.* Phys. Rev. Lett., **94**, 060503 (2005). doi:10.1103/PhysRevLett.94.060503.

[142] Plenio, M.B., Huelga, S.F., Beige, A., and Knight, P.L. *Cavity-loss-induced generation of entangled atoms.* Phys. Rev. A, **59**, 2468–2475 (1999). doi:10.1103/PhysRevA.59.2468.

[143] Plenio, M.B. and Knight, P.L. *The quantum-jump approach to dissipative dynamics in quantum optics.* Rev. Mod. Phys., **70**, 101–144 (1998). doi:10.1103/RevModPhys.70.101.

[144] Preskill, J. *Quantum computing and the entanglement frontier* (2012).

[145] Preskill, J. *Quantum Computing in the NISQ era and beyond*. Quantum, **2**, 79 (2018). doi:10.22331/q-2018-08-06-79.

[146] Ritsch, H., Domokos, P., Brennecke, F., and Esslinger, T. *Cold atoms in cavity-generated dynamical optical potentials*. Rev. Mod. Phys., **85**, 553–601 (2013). doi:10.1103/RevModPhys.85.553.

[147] Rota, R., Minganti, F., Ciuti, C., and Savona, V. *Quantum critical regime in a quadratically driven nonlinear photonic lattice*. Phys. Rev. Lett., **122**, 110405 (2019). doi:10.1103/PhysRevLett.122.110405.

[148] Rota, R., Storme, F., Bartolo, N., Fazio, R., and Ciuti, C. *Critical behavior of dissipative two-dimensional spin lattices*. Phys. Rev. B, **95**, 134431 (2017). doi:10.1103/PhysRevB.95.134431.

[149] Sacha, K. and Zakrzewski, J. *Time crystals: a review*. Reports on Progress in Physics, **81**, 1, 016401 (2017). doi:10.1088/1361-6633/aa8b38.

[150] Sakurai, J. and Napolitano, J. *Modern Quantum Mechanics*. Cambridge University Press (2020). ISBN 9781108473224.

[151] Savona, V. *Spontaneous symmetry breaking in a quadratically driven nonlinear photonic lattice*. Phys. Rev. A, **96**, 033826 (2017). doi:10.1103/PhysRevA.96.033826.

[152] Schachenmayer, J., Pikovski, A., and Rey, A.M. *Many-body quantum spin dynamics with monte carlo trajectories on a discrete phase space*. Phys. Rev. X, **5**, 011022 (2015). doi:10.1103/PhysRevX.5.011022.

[153] Schäfer, F., Fukuhara, T., Sugawa, S., Takasu, Y., and Takahashi, Y. *Tools for quantum simulation with ultracold atoms in optical lattices*. Nature Reviews Physics, **2**, 8, 411–425 (2020). doi:10.1038/s42254-020-0195-3.

[154] Schlosshauer, M. *Decoherence, the measurement problem, and interpretations of quantum mechanics*. Rev. Mod. Phys., **76**, 1267–1305 (2005). doi:10.1103/RevModPhys.76.1267.

[155] Schmidt, S., Blatter, G., and Keeling, J. *From the jaynes-cummings-hubbard to the dicke model*. J. Phys. B: At. Mol. Opt. Phys. 46 224020 (2013) (2013). doi:10.1088/0953-4075/46/22/224020.

[156] Schollwöck, U. *The density-matrix renormalization group in the age of matrix product states*. Annals of Physics, **326**, 1, 96–192 (2011). doi:https://doi.org/10.1016/j.aop.2010.09.012. January 2011 Special Issue.

[157] Schuch, N., Wolf, M.M., Verstraete, F., and Cirac, J.I. *Computational complexity of projected entangled pair states*. Phys. Rev. Lett., **98**, 140506 (2007). doi:10.1103/PhysRevLett.98.140506.

[158] Shi, Y.Y., Duan, L.M., and Vidal, G. *Classical simulation of quantum many-body systems with a tree tensor network*. Phys. Rev. A, **74**, 022320 (2006). doi:10.1103/PhysRevA.74.022320.

[159] Shore, B.W. and Knight, P.L. *The jaynes-cummings model*. Journal of Modern Optics, **40**, 7, 1195–1238 (1993). doi:10.1080/09500349314551321.

[160] Siddiqi, I. *Engineering high-coherence superconducting qubits*. Nature Reviews Materials, **6**, 10, 875–891 (2021). doi:10.1038/s41578-021-00370-4.

[161] Sieberer, L.M., Huber, S.D., Altman, E., and Diehl, S. *Dynamical critical phenomena in driven-dissipative systems.* Phys. Rev. Lett., **110**, 195301 (2013). doi: 10.1103/PhysRevLett.110.195301.

[162] Srednicki, M. *Entropy and area.* Phys. Rev. Lett., **71**, 666–669 (1993). doi: 10.1103/PhysRevLett.71.666.

[163] Steane, A. *The ion trap quantum information processor.* Applied Physics B, **64**, 6, 623–643 (1997). doi:10.1007/s003400050225.

[164] Strathearn, A., Kirton, P., Kilda, D., Keeling, J., and Lovett, B.W. *Efficient non-markovian quantum dynamics using time-evolving matrix product operators.* Nature Communications, **9**, 1, 3322 (2018). doi:10.1038/s41467-018-05617-3.

[165] Terhal, B.M., Horodecki, M., Leung, D.W., and DiVincenzo, D.P. *The entanglement of purification.* Journal of Mathematical Physics, **43**, 9, 4286–4298 (2002). doi:10.1063/1.1498001.

[166] Toner, J. and Tu, Y. *Flocks, herds, and schools: A quantitative theory of flocking.* Phys. Rev. E, **58**, 4828–4858 (1998). doi:10.1103/PhysRevE.58.4828.

[167] Tucker, K., Zhu, B., Lewis-Swan, R.J., Marino, J., Jimenez, F., Restrepo, J.G., and Rey, A.M. *Shattered time: can a dissipative time crystal survive many-body correlations?* New Journal of Physics, **20**, 12, 123003 (2018). doi: 10.1088/1367-2630/aaf18b.

[168] Vanderstraeten, L., Haegeman, J., and Verstraete, F. *Tangent-space methods for uniform matrix product states.* SciPost Phys. Lect. Notes, p. 7 (2019). doi:10.21468/SciPostPhysLectNotes.7.

[169] Vanderstraeten, L., Vanhecke, B., Läuchli, A.M., and Verstraete, F. *Approaching*

the kosterlitz-thouless transition for the classical xy model with tensor networks. Phys. Rev. E, **100**, 062136 (2019). doi:10.1103/PhysRevE.100.062136.

[170] Verstraelen, W., Rota, R., Savona, V., and Wouters, M. *Gaussian trajectory approach to dissipative phase transitions: The case of quadratically driven photonic lattices.* Phys. Rev. Research, **2**, 022037 (2020). doi:10.1103/PhysRevResearch.2.022037.

[171] Verstraete, F., García-Ripoll, J.J., and Cirac, J.I. *Matrix product density operators: Simulation of finite-temperature and dissipative systems.* Phys. Rev. Lett., **93**, 207204 (2004). doi:10.1103/PhysRevLett.93.207204.

[172] Verstraete, F., Wolf, M.M., and Ignacio Cirac, J. *Quantum computation and quantum-state engineering driven by dissipation.* Nature Physics, **5**, 9, 633–636 (2009). doi:10.1038/nphys1342.

[173] Verstraete, F., Wolf, M.M., Perez-Garcia, D., and Cirac, J.I. *Criticality, the area law, and the computational power of projected entangled pair states.* Phys. Rev. Lett., **96**, 220601 (2006). doi:10.1103/PhysRevLett.96.220601.

[174] Vicentini, F., Biella, A., Regnault, N., and Ciuti, C. *Variational neural-network ansatz for steady states in open quantum systems.* Phys. Rev. Lett., **122**, 250503 (2019). doi:10.1103/PhysRevLett.122.250503.

[175] Vidal, G. *Efficient classical simulation of slightly entangled quantum computations.* Phys. Rev. Lett., **91**, 147902 (2003). doi:10.1103/PhysRevLett.91.147902.

[176] Vidal, G. *Efficient simulation of one-dimensional quantum many-body systems.* Phys. Rev. Lett., **93**, 040502 (2004). doi:10.1103/PhysRevLett.93.040502.

[177] Vidal, G., Latorre, J.I., Rico, E., and Kitaev, A. *Entanglement in quantum critical*

phenomena. Phys. Rev. Lett., **90**, 227902 (2003). doi:10.1103/PhysRevLett.90.227902.

[178] Vidal, G. and Werner, R.F. *Computable measure of entanglement*. Physical Review A, **65**, 3, 032314 (2002). doi:10.1103/physreva.65.032314.

[179] Wallraff, A., Schuster, D.I., Blais, A., Frunzio, L., Huang, R.S., Majer, J., Kumar, S., Girvin, S.M., and Schoelkopf, R.J. *Strong coupling of a single photon to a superconducting qubit using circuit quantum electrodynamics*. Nature, **431**, 7005, 162–167 (2004). doi:10.1038/nature02851.

[180] Wang, X., Yu, C.S., and Yi, X. *An alternative quantum fidelity for mixed states of qudits*. Physics Letters A, **373**, 1, 58–60 (2008). doi:10.1016/j.physleta.2008.10.083.

[181] Watanabe, H. and Oshikawa, M. *Absence of quantum time crystals*. Phys. Rev. Lett., **114**, 251603 (2015). doi:10.1103/PhysRevLett.114.251603.

[182] Weimer, H. *Variational analysis of driven-dissipative rydberg gases*. Phys. Rev. A, **91**, 063401 (2015). doi:10.1103/PhysRevA.91.063401.

[183] Weimer, H. *Variational principle for steady states of dissipative quantum many-body systems*. Phys. Rev. Lett., **114**, 040402 (2015). doi:10.1103/PhysRevLett.114.040402.

[184] Weimer, H., Kshetrimayum, A., and Orús, R. *Simulation methods for open quantum many-body systems*. Rev. Mod. Phys., **93**, 015008 (2021). doi:10.1103/RevModPhys.93.015008.

[185] Weimer, H., Müller, M., Lesanovsky, I., Zoller, P., and Büchler, H.P. *A rydberg quantum simulator*. Nature Physics, **6**, 5, 382–388 (2010). doi:10.1038/nphys1614.

[186] Werner, A.H., Jaschke, D., Silvi, P., Kliesch, M., Calarco, T., Eisert, J., and Montangero, S. *Positive tensor network approach for simulating open quantum many-body systems.* Phys. Rev. Lett., **116**, 237201 (2016). doi:10.1103/PhysRevLett.116.237201.

[187] White, C.D., Zaletel, M., Mong, R.S.K., and Refael, G. *Quantum dynamics of thermalizing systems.* Phys. Rev. B, **97**, 035127 (2018). doi:10.1103/PhysRevB.97.035127.

[188] Wigner, E.P. *On the Quantum Correction for Thermodynamic Equilibrium*, pp. 110–120. Springer Berlin Heidelberg, Berlin, Heidelberg (1997). ISBN 978-3-642-59033-7. doi:10.1007/978-3-642-59033-7_9.

[189] Wilen, C.D., Abdullah, S., Kurinsky, N.A., Stanford, C., Cardani, L., D'Imperio, G., Tomei, C., Faoro, L., Ioffe, L.B., Liu, C.H., Opremcak, A., Christensen, B.G., DuBois, J.L., and McDermott, R. *Correlated charge noise and relaxation errors in superconducting qubits.* Nature, **594**, 7863, 369–373 (2021). doi:10.1038/s41586-021-03557-5.

[190] Wolf, M.M., Verstraete, F., Hastings, M.B., and Cirac, J.I. *Area laws in quantum systems: Mutual information and correlations.* Phys. Rev. Lett., **100**, 070502 (2008). doi:10.1103/PhysRevLett.100.070502.

[191] Xiang, T., Lou, J., and Su, Z. *Two-dimensional algorithm of the density-matrix renormalization group.* Phys. Rev. B, **64**, 104414 (2001). doi:10.1103/PhysRevB.64.104414.

[192] Yoshioka, N. and Hamazaki, R. *Constructing neural stationary states for open quantum many-body systems.* Phys. Rev. B, **99**, 214306 (2019). doi:10.1103/PhysRevB.99.214306.

[193] You, J.Q. and Nori, F. *Atomic physics and quantum optics using superconducting circuits*. Nature, **474**, 7353, 589–597 (2011). doi:10.1038/nature10122.

[194] Yu, J.F., Xie, Z.Y., Meurice, Y., Liu, Y., Denbleyker, A., Zou, H., Qin, M.P., Chen, J., and Xiang, T. *Tensor renormalization group study of classical xy model on the square lattice*. Phys. Rev. E, **89**, 013308 (2014). doi:10.1103/PhysRevE.89.013308.

[195] Zauner-Stauber, V., Vanderstraeten, L., Fishman, M.T., Verstraete, F., and Haegeman, J. *Variational optimization algorithms for uniform matrix product states*. Phys. Rev. B, **97**, 045145 (2018). doi:10.1103/PhysRevB.97.045145.

[196] Zhu, B., Marino, J., Yao, N.Y., Lukin, M.D., and Demler, E.A. *Dicke time crystals in driven-dissipative quantum many-body systems*. New Journal of Physics, **21**, 7, 073028 (2019). doi:10.1088/1367-2630/ab2afe.

[197] Zwolak, M. and Vidal, G. *Mixed-state dynamics in one-dimensional quantum lattice systems: A time-dependent superoperator renormalization algorithm*. Phys. Rev. Lett., **93**, 207205 (2004). doi:10.1103/PhysRevLett.93.207205.

Appendix A

$\mathcal{PT}-$Symmetry of the Anisotropic Dissipative XY- Model

In this section we follow [83] to show the $\mathcal{PT}$-symmetry of the anisotropic dissipative XY-model considered in chapter 5. To begin, it is useful to express the Hamiltonian of the anisotropic XY model in terms of the spin raising and lowering operators and labelling the two subspaces A and B explicitly. Doing this results in the a Liouvillian $\mathcal{L}[H_{XY}; \sqrt{\Gamma}\sigma_A^-, \sqrt{\Gamma}\sigma_B^-]$ where the Hamiltonian is $H_{XY} = \frac{J}{z}\sum_{\langle A,B\rangle} \sigma_A^+ \otimes \sigma_B^+ + \sigma_A^- \otimes \sigma_B^-$ and dissipators are the local Lindblad jump operators on each subspace $L_A = \sqrt{\Gamma}\sigma_A^-$ and $L_B = \sqrt{\Gamma}\sigma_B^-$. By choosing the unitary $\mathcal{U} = e^{i\frac{\pi}{2}(\sigma_A^x + \sigma_B^x)}$, the transformation $\mathbb{PT}(O) = \mathcal{PU}O^\dagger(\mathcal{PU})^{-1}$ leaves the components of $\mathcal{L}[H; \sqrt{\Gamma}\sigma_A^-, \sqrt{\Gamma}\sigma_B^-]$ invariant, in particular it satisfies the equation

$$\mathcal{L}[\mathbb{PT}(H_{XY}); \mathbb{PT}(\sqrt{\Gamma}\sigma_A^-), \mathbb{PT}(\sqrt{\Gamma}\sigma_B^-)] = \mathcal{L}[H; \sqrt{\Gamma}\sigma_A^-, \sqrt{\Gamma}\sigma_B^-]. \tag{A.1}$$

To verify this, the symmetry is applied to each term individually as follows. Recall that the parity operator has the effect of swapping the subspaces such that $\mathcal{P}A \otimes B\mathcal{P}^{-1} = B \otimes A$ and the unitary U acts on each subspace independently and corresponds to a π

rotation about the x-axis.

$$\begin{aligned}
\mathbb{PT}(H_{XY}) =& \frac{J}{z}\sum_{\langle A,B\rangle}\mathcal{PU}[\sigma_A^+\otimes\sigma_B^+ + \sigma_A^-\otimes\sigma_B^-]^\dagger(\mathcal{PU})^{-1} \\
=& \frac{J}{z}\sum_{\langle A,B\rangle}\mathcal{PU}[\sigma_A^-\otimes\sigma_B^- + \sigma_A^+\otimes\sigma_B^+](\mathcal{PU})^{-1} \\
=& \frac{J}{z}\sum_{\langle A,B\rangle}\mathcal{P}[\sigma_A^+\otimes\sigma_B^+ + \sigma_A^-\otimes\sigma_B^-](\mathcal{P})^{-1} \\
=& \frac{J}{z}\sum_{\langle B,A\rangle}[\sigma_B^+\otimes\sigma_A^+ + \sigma_B^-\otimes\sigma_A^-] \\
=& H_{XY}
\end{aligned} \tag{A.2}$$

$$\begin{aligned}
\mathbb{PT}(\sqrt{\Gamma}\sigma_A^-) =& \sqrt{\Gamma}\mathcal{PU}[\sigma^-\otimes\mathbb{I}]^\dagger(\mathcal{PU})^{-1} \\
=& \sqrt{\Gamma}\mathcal{PU}[\sigma^+\otimes\mathbb{I}](\mathcal{PU})^{-1} \\
=& \sqrt{\Gamma}\mathcal{P}\sigma^-\otimes\mathbb{I}\mathcal{P}^{-1} \\
=& \sqrt{\Gamma}\mathbb{I}\otimes\sigma^- \\
=& \sqrt{\Gamma}\sigma_B^-
\end{aligned} \tag{A.3}$$

$$\begin{aligned}
\mathbb{PT}(\sqrt{\Gamma}\sigma_B^-) =& \sqrt{\Gamma}\mathcal{PU}[\mathbb{I}\otimes\sigma^-]^\dagger(\mathcal{PU})^{-1} \\
=& \sqrt{\Gamma}\mathcal{P}U[\mathbb{I}\otimes\sigma^+](\mathcal{PU})^{-1} \\
=& \sqrt{\Gamma}\mathcal{P}\mathbb{I}\otimes\sigma^-\mathcal{P}^{-1} \\
=& \sqrt{\Gamma}\sigma^-\otimes\mathbb{I} \\
=& \sqrt{\Gamma}\sigma_A^-
\end{aligned} \tag{A.4}$$

We are therefore left with the Liouvillian $\mathcal{L}[H_{XY};\sqrt{\Gamma}\sigma_B^-,\sqrt{\Gamma}\sigma_A^-]$, we can then use its symmetry under swapping subsystems $A\leftrightarrow B$ to arrive at the original Liouvillian $\mathcal{L}[H_{XY};\sqrt{\Gamma}\sigma_A^-,\sqrt{\Gamma}\sigma_B^-]$. For this model, the occupations on each sublattice remain the same for any values of the dissipation and the model is $\mathcal{PT}$-symmetric.

This results associated to the model's classification as $\mathcal{PT}$-symmetric hold so long

as any additional symmetry $\mathcal{S}$ of the Hamiltonian commutes with $\mathcal{P}$. Of course the symmetry defined by the unitary $U_\phi^z = e^{i\phi\sum(\sigma_A^z - \sigma_B^z)}$ clearly does not commute with $\mathcal{P}$, however this does not play a role in this case since $\langle\sigma_A^z\rangle = \langle\sigma_B^z\rangle$ throughout.